Graphitic Carbon and Bimetallic Bismuth Oxide composites for Adsorption and Photocatalytic Removal of Toxic Pollutants

A Thesis

Submitted for the fulfillment of the requirement for the award of degree of

Doctor of Philosophy

Submitted by:

Priti Rohilla
(Regn. No. 902009014)

THAPAR INSTITUTE
OF ENGINEERING & TECHNOLOGY
(Deemed to be University)

Under the supervision of

Dr. Raj Kumar Das
Assistant Professor

Dr. Bonamali Pal
Professor

Department of Chemistry & Biochemistry
Thapar Institute of Engineering and Technology

Patiala-147004, India

2025

Certificate

This is to certify that the work embodied in this thesis entitled **"Graphitic Carbon and Bimetallic Bismuth Oxide composites for Adsorption and Photocatalytic Removal of Toxic Pollutants"** has been carried out by Ms. Priti Rohilla under my supervision and guidance in the Department of Chemistry and Biochemistry, Thapar Institute of Engineering and Technology, Patiala. The candidate completed all the conditions required for the fulfilment of the award of the Degree of Philosophy.

I also certified that the work represented in this thesis is original and has not been submitted in part or full for the award of any degree in any other University or Institute.

Dr. Raj Kumar Das

Assistant Professor

Department of Chemistry and Biochemistry

Dr. Bonamali Pal

Professor

Department of Chemistry and Biochemistry

Dr. Manmohan Chhibber

Professor and Head

Department of Chemistry and Biochemistry

Candidate's Declaration

I, hereby declare that the work presented in the thesis entitled **"Graphitic Carbon and Bimetallic Bismuth Oxide composites for Adsorption and Photocatalytic Removal of Toxic Pollutants"**, in fulfilment of the requirement for the award of the Degree of Doctor of Philosophy, Department of Chemistry and Biochemistry, Thapar Institute of Engineering and Technology, Patiala, is an authentic record of my own work carried out under the supervision of Dr. Raj Kumar Das (Assistant Professor) and Dr. Bonamali Pal (Professor), Department of Chemistry and Biochemistry, Thapar Institute of Engineering and Technology, Patiala, India. The matter embodied in this thesis has not been submitted in part or full to any other University or Institute for the award of any degree in India or Abroad.

Priti Rohilla

Dr. Raj Kumar Das

(Assistant Professor and Supervisor)

Dr. Bonamali Pal

(Professor and Supervisor)

Acknowledgement

I am deeply grateful to God, the Almighty, for his abundant blessings and guidance throughout my research journey. His grace has been a constant source of strength, enabling me to bring this work to completion.

The successful completion of this thesis would not have been possible without the invaluable support and encouragement of many individuals. I am immensely grateful to each one of them, and I find that words themselves cannot fully express my gratitude.

First, I would like to express my sincere gratitude towards my research supervisors **Dr. Raj Kumar Das** and **Prof. Bonamali Pal,** I owe deep gratitude to them for their generous guidance, insightful feedback, invaluable suggestions, and ongoing support. They have mentored me through every stage, from foundational steps to experimental design. Their unwavering support and encouragement have been a steady source of inspiration. Without their dedication and assistance, the goals of this project would not have been achieved.

I would also like to express my deep gratitude to the **Dean** (Research & Development Cell), **Head of the Department of Chemistry & Biochemistry** at Thapar University, for granting me the opportunity to pursue this doctoral research. I am truly grateful to my doctoral committee members, **Prof. Soumen Basu**, **Dr. Banibrata Maity**, and **Prof. Bhaskar Chandra Mohanty**, for their timely and invaluable guidance. I would like to express my sincere gratitude to **Prof. Satnam Singh** for graciously allowing me to utilize his lab for my work. I deeply appreciate the opportunity and the resources provided, which have been invaluable in furthering my research. My heartfelt thanks also go to **Mr. Chander Thakur** and **Mr. Hemant Kumar** and office staff member **Mr. Mayank** for their continuous cooperation, support, and assistance.

I would like to acknowledge my seniors **Dr. Pooja Kumari, Dr. Harpreet Kaur, Dr. Manjusha Passi**. My lab mates and friends **Dr. Davinder Kaur, Dr. Mehak Bansal, Riddhima, Sukhandeep Kaur, Shikha Rani, Kamya, Dr. Jemini, Shreya Sharma, Dr. Palak Soni, Samridhi Kochar, Kirti Bisht, Tania and Ishita** for their support and co-operation. I am grateful for my friends from other lab groups **Paramjeet Kaur, Abinash Mohapatra, Kirti Singh, Palak Sharma,** and **Mandeep Kaur** for their endless motivation, support and selfless help.

Special thanks to my friends **Himani Bains** and **Ajay Singh** for always inspiring, encouraging and supporting me during my challenging time. Without their mental support I might not have been able to reach the finish line.

I am deeply grateful to my parents, my father, **Mr. Kishan Chand**, who always encourage, support and push me to pursue my dreams. I would also like to acknowledge my deepest gratitude to my beloved mother, **Mrs. Kamlesh Kumari**, for the countless sacrifices she has made throughout her life. Her unwavering support and encouragement continually uplift me, filling me with positivity and guiding me toward my goals. Words cannot capture the depth of my appreciation for their persistent love, boundless support, and constant blessings. They are, and always will be, my greatest inspiration. I would also acknowledge my brother **Mr. Vikas Rohilla** and sister-in-law **Mrs. Nancy Rohilla** for their love, mental support and always motivating me to accomplish my dream. Last but not the least, my little love my nephew **Darsh Rohilla (Laddu)** who always make me feel more fulfilled and complete myself.

The help from other institutes and laboratories like **SAI Lab TIET, SPRINT testing solution** Mumbai etc. are highly acknowledged. I am highly thankful to **DST-FIST** (Grant number: SR/FST/CS-II/2018/69) for providing the HRMS facility at TIET-Patiala

Besides this, I am grateful to each person who knowingly and unknowingly supported me in the successful completion of this work.

Priti Rohilla

DEDICATED

to

My PARENTS

Table of contents

Chapter-1

Introduction and Literature Survey

Chapter-2

Fabrication of g-C_3N_4 loaded $BiVO_4$ binary nanocomposites for the photocatalytic removal of Rhodamine B.

Chapter-3

Photocatalytic degradation of Reactive orange 16 under visible light using ternary nanocomposite Bi-doped g-C_3N_4/Bi_2WO_6.

Chapter-4

Bi-doped g-C_3N_4/Bi_2MoO_6 ternary nanocomposite for the effective photodegradation of Ofloxacin under visible light irradiation.

List of Abbreviations

ms	Monoclinic schellite
ts	Tetragonal schellite
tz	Tetragonal zircon
C_3N_4	Carbon nitride
g-CN	Graphitic carbon nitride (g-C_3N_4)
C_3N_3	s-triazine
C_6N_7	tri-s-triazine
CB	Conduction band
VB	Valence band
ROS	Reactive oxygen species
rGO	Reduced graphene oxide
EG	Ethylene glycol
GO	Graphene oxide
SPR	Surface plasmon resonance
LSPR	Localised surface plasmon resonance
Bi	Bismuth
BBO	Bimetallic bismuth oxide
UV	Ultraviolet
Vis	Visible
DI	Distilled water
CTAB	Cetyltrimethylammonium bromide
XRD	X-ray diffraction
FTIR	Fourier transform infrared spectroscopy
XPS	X-ray photon spectroscopy
FESEM	Field emission scanning electron microscopy
HRTEM	High-resolution transmission electron microscopy
SAED	Selected area diffraction
EIS	Electrochemical impedance spectroscopy

DRS	Diffuse reflectance studies
DLS	Dynamic light scattering
EDS	Energy dispersive spectroscopy
BET	Brunauer Emmett-Teller
HRMS	High resolution mass spectrometer
TOC	Total organic carbon
COD	Chemical oxygen demand
BVO	Bismuth vanadate ($BiVO_4$)
BCN-1	5 wt.% loading of g-CN@BVO
BCN-2	10 wt.% loading of g-CN@BVO
BW	Bi@ Bismuth tungstate
BWO	Bismuth tungstate (Bi_2WO_6)
5GBW	5 wt.% g-CN loaded Bi@ BWO
10GBW	10 wt.% g-CN loaded Bi@ BWO
20GBW	20 wt.% g-CN loaded Bi@ BWO
BM	Bi@ Bismuth molybdate
BMO	Bismuth molybdate (Bi_2MoO_6)
5GBM	5 wt.% g-CN loaded Bi@ BMO
10GBM	10 wt.% g-CN loaded Bi@ BMO
RO-16	Reactive orange 16
OFL	Ofloxacin
RhB	Rhodamine B
NMP	N-methyl-2-pyrrolidone
FTO	Fluorinated tin oxide
PVDF	Polyvinylidene fluoride
CB	Carbon black
wt.%	Weight percentage
EDTA	Ethylenediamine tetra acetic acid
iPA	Isopropyl alcohol

List of Symbols

e^-	Electron
h^+	Hole
$^{\bullet}OH$	Hydroxyl radical
^-OH	Hydroxide ion
$^{\cdot}O_2^-$	Superoxide radical
Å	Angstrom
λ	Wavelength
α	Absorption coefficient
μ	Micro
θ	Theta
mM	Millimolar
m	Meter
mg	Milligram
h	Hour
eV	Electron volt
ppm	Parts per million
g	Gram
C	Concentration
%	Percentage
M	Molar
°C	Degree Celsius
mmol	Millimole
mL	Millilitre
min	Minute
μL	Microlitre
nm	Nanometre
W	Watt
t	Time

m^2/g	Metre square per gram
E_g	Band gap
E_0	Electrode potential
a.u.	Arbitrary unit
2D	Two dimensional
KΩ	Kiloohm

Abstracts

Chapter-1

The chapter includes the structural and chemical composition of bimetallic bismuth oxide compounds, as well as their adsorptive and photocatalytic properties. The behaviour and changes of BBOs have been addressed in relation to adsorption and photocatalysis. This chapter also covers the literature evaluation, research gaps, objectives, experimental procedures, and characterisation methodologies.

Chapter-2

Photocatalytic degradation has emerged as one of the most efficient methods to eliminate toxic dyes from wastewater. In this context, graphitic nitride (g-C_3N_4) loaded $BiVO_4$ nanocomposites (5wt.% g-CN@$BiVO_4$ and 10wt.% g-CN@$BiVO_4$) have been fabricated by the wet impregnation method, and their efficiency towards photocatalytic removal of rhodamine B have been investigated under visible light irradiation. These hybrid composites have been characterized by XRD, FESEM, HRTEM, EDS-mapping, UV-Vis DRS, DLS, XPS and BET, etc. The HRTEM images revealed that $BiVO_4$ has a decagonal shape covered by a layered nanosheet-like structure of g-C_3N_4. BET measurements suggest increasing the proportion of g-C_3N_4 results enhancement of the specific surface area. Among different photocatalysts, the 10wt.% g-C_3N_4@$BiVO_4$ hybrid possesses the best catalytic activity with 86% degradation efficiency after 60 minutes of reaction time. The LC-MS studies suggest that the degradation reactions follow the de-ethylation pathway. Even after five cycles, the heterostructure shows only a 14% decrease in photocatalytic activity, confirming its stability. As a result, the binary composite can be regarded as a promising catalyst for the degradation of pollutants due to its ease of preparation, high stability and superior catalytic activity.

Chapter-3

Because of unrestricted disposal, the concentration of reactive dyes in wastewater is gradually increasing. Owing to their eco-toxicity their removal becomes so crucial. In this regard, Bi (0)-doped g-C_3N_4/Bi_2WO_6 (g-C_3N_4/Bi@Bi_2WO_6) nanocomposites were prepared by wet impregnation followed by calcination. Remarkably, the Bi (0) doping occurs concertedly during the preparation of Bi_2WO_6 without the addition of any extra reducing agent. The efficacy of the photocatalyst for eliminating reactive orange 16 was evaluated under visible light irradiation. XRD, FESEM, HRTEM, DRS, XPS, BET, etc., were employed to characterize these hybrids. The presence of Bi (0) was confirmed by HRTEM and XPS. Increasing the g-C_3N_4 content enhances the specific surface and reduces the charge

transfer resistance. Among the various photocatalysts, the 20 wt.% g-C_3N_4/Bi@Bi_2WO_6 hybrid owned the highest degradation efficiency of 89 % after 300 min of reaction time. The controlled experiments confirm the participation of holes and superoxide anions during the reactions. The various reaction intermediates were detected by HRMS providing the necessary evidence about the mechanism. The heterostructure possesses excellent reusability and stability. Due to enhanced catalytic activity, high stability, and ease of synthesis, the reported composite can be considered as a promising catalyst for the degradation of pollutants.

Chapter-4

Water contamination is a result of the excessive use of antibiotics nowadays. Owing to this environmental toxicity, photocatalytic degradation is the primary approach to non-biological degradation for their removal. In this respect, Bi (0)-doped g-C_3N_4/Bi_2MoO_6 [g-C_3N_4/Bi@Bi_2MoO_6] ternary nanocomposite was prepared using the wet impregnation method. Surprisingly, the zerovalent Bi is generated simultaneously during the hydrothermal synthesis of Bi_2MoO_6 without any extra reducing agent. The performance of the synthesised catalyst for the removal of ofloxacin is measured using visible light radiation. Various techniques like XRD, XPS, DRS, HRTEM, FESEM etc characterise the nanocomposite. Additionally, XPS, DRS and HRTEM confirm the presence of zerovalent Bi. The degradation efficiency was recorded to be 82% after 180 min of reaction time for the optimised catalyst. The control experiments validate the role of holes and superoxide radicals in the reaction mechanism. HRMS was used to identify the intermediates and various fragments which support the suggested mechanism. The photocatalyst exhibits outstanding stability and reusability. Due to its stability, easy synthesis, excellent catalytic activity, and reusability, the reported photocatalyst is considered favourable for pollutant degradation.

CHAPTER-1

CHAPTER-1

Introduction and Literature Review

1.1 Wastewater Treatment:

The rapid growth of industry and the notable rise in population have led to significant environmental damage due to the depletion of mineral fuels. Numerous efforts have been made to develop environmentally friendly, sustainable technologies to ensure the perpetual development of society[1]. The availability of clean, fresh and harmless drinking water, free from contaminants, bacteria and carcinogens are crucial for human health. The report in 2018 of United Nations World Water Development expects that the consumption for fresh clean water will increase around one-third by 2050[2]. Water is an essential resource for all living things, and human health and wellbeing are affected directly by the quality of the water. Though water covers approximately two-third surface of earth, still the useful and fresh is only 3%, with major part is stored for glaciers and polar ice caps which makes it inaccessible[3]. Several industries such as food, medicine, textile, electrical, and electronics require clean water as a primary necessity[4]. Many of these industries utilizes a substantial amount of water, which turns into contaminated one after the manufacturing steps. Therefore, treating a major part of it becomes difficult because of the varied composition of waste such as pharmaceutical residue, colouring agent or dyes, organic substances, inhibitory compounds, hazardous material etc. Standard methods for treating wastewater often fail to meet requirements[5].

Semiconductor photocatalysis is a technique driven by renewable energy sources and has garnered significant interest in energy conversion, pollutant degradation, and hydrogen energy production[6–8]. Most materials with superior photocatalytic performance are found in wide-band gap semiconductors, such as niobate, ZnO, TiO_2, and metal titanate[9–12]. Due to their high band gap value (> 3eV) which can only absorb a small portion of UV light and affects photocatalytic activity, results in application constraints in daily practical life. Concurrently, the stability of the material does not meet the demands of industry production which restricts photocatalytic advancement[13–15].

1.1.1 Bimetallic bismuth oxide-based photocatalyst:

Numerous bismuth-based photocatalysts for environmental treatment that are driven by visible light have been reported recently. Bi_aAO_b -based semiconductor photocatalysts have shown potential in several fields and attained notable photocatalytic performance[16]. The valence band of bismuth-based material is composed of the 6s orbital of Bi and the 2p orbital of O, in contrast, the valence band of other materials like TiO_2 only comprises O 2p, therefore the hybrid orbital of Bi 6s and O 2p results

in good dispersion of charge which further reduces the bandgap values [17]. Bismuth-based materials are synthesised through various methods as represented in **Scheme – 1.1,** Among these, only hydrothermal and co-precipitation methods effectively produce materials with efficient photocatalytic activity and controlled morphology[18].

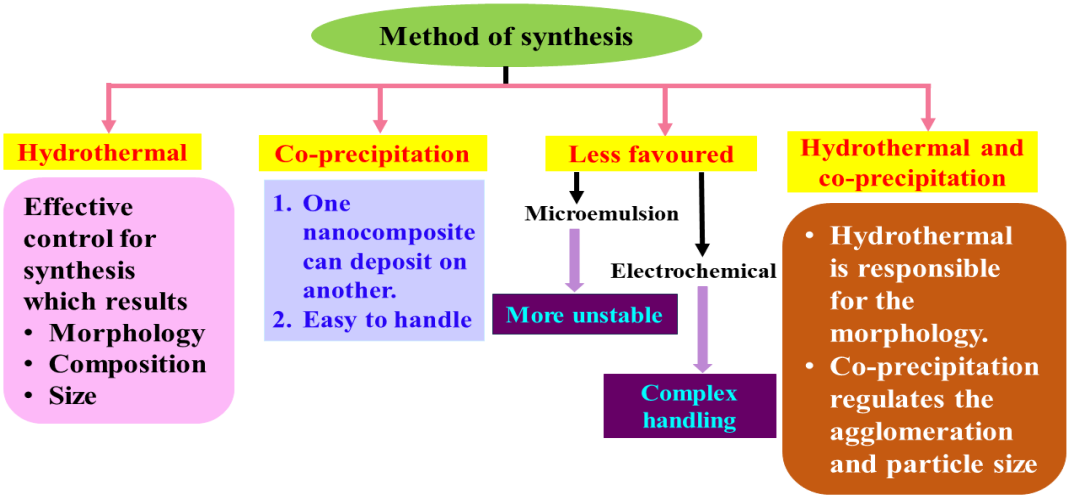

Scheme 1.1: Various methods for synthesising bismuth-based material[18].

$BiVO_4$ has attracted attention due to its remarkable visible-light-driven photocatalytic activity for destructing pollutants, low band gap value (2.4 eV), corrosion resistance, superior dispersibility, and non-toxicity. $BiVO_4$ exists mainly in three phases: monoclinic scheelite (ms), tetragonal scheelite (ts) and tetragonal zircon (tz), but the most thermodynamically stable phase is monoclinic that shows good photoelectrochemical properties. The structure of $BiVO_4$ is composed of a stacked layer of Bi_2O_3 and V_2O_5[19]. The ternary metal oxide known as bismuth tungstate (Bi_2WO_6) is made up of octahedral tungstate $[WO_4]^{2-}$ and bismuth oxide $[Bi_2O_2]^{2+}$ alternating layers. Calcite-type molybdate $[MoO_4^{2-}]$and bismuth oxide $[Bi_2O_2]^{2+}$constituents of bismuth molybdate (Bi_2MoO_6) which resembles the perovskite-like structure. Both have significant potential for applications in photocatalysis due to their sustainable nature, low cost, big specific surface area, excellent visible light sensitivity, and photothermal stability [20,21]. $BiFeO_3$ and $BiPO_4$ also show good photocatalytic activity [22–24].

A photocatalytic reaction is a redox process in which light energy is absorbed by a semiconductor photocatalyst, generating charge carrier holes (h^+) and electrons (e^-) only when the energy value reaches above the threshold energy. As a result, oxidising species, such as hydroxyl radicals ($^{\cdot}OH$) and superoxide radicals ($^{\cdot}O_2^-$), break down the organic contaminants into smaller molecules as shown in **Scheme -1.2** [25–28].

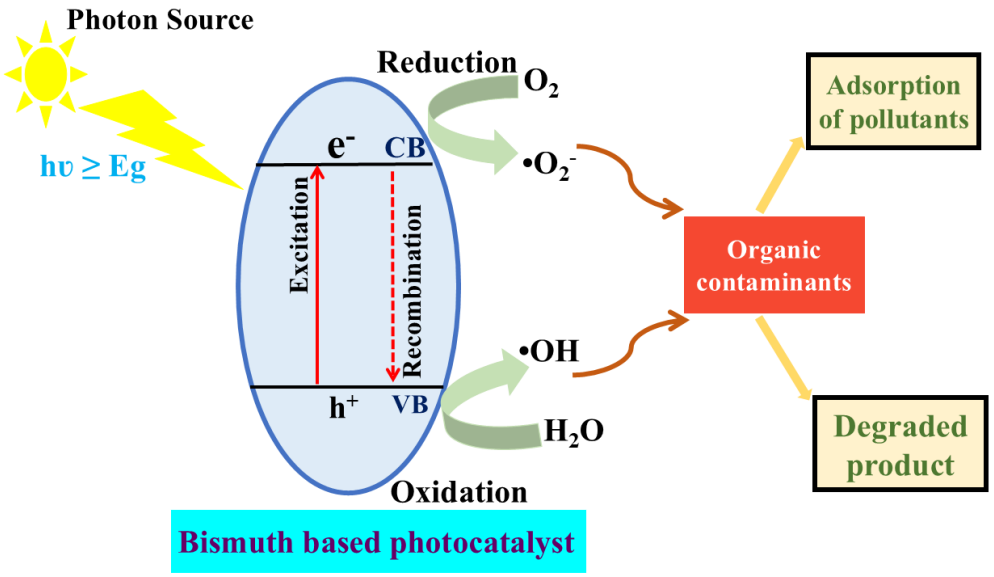

Scheme 1.2: A schematic representation showing pollutant degradation through photocatalysis.

The potential values for bismuth-based materials are represented in **Scheme -1.3**.

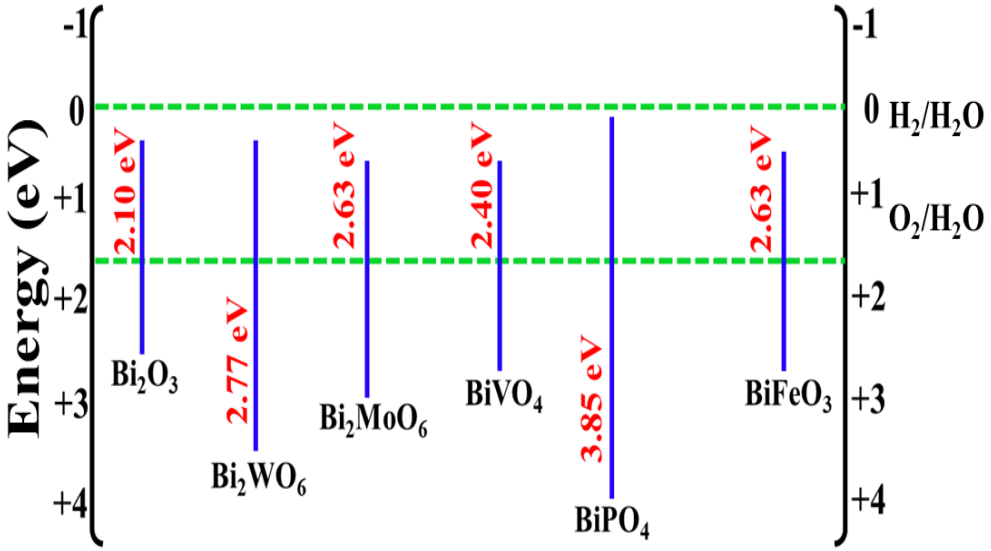

Scheme 1.3: Band position values of different Bismuth material[17].

Despite its advantages, pristine $BiVO_4$ has generally unsatisfactory photocatalytic performance because the photo-excited charge carriers tend to drop fast through recombination. Pure Bi_2MoO_6 demonstrates excellent photogenerated charge carrier separation, however, it absorbs light primarily in the ultraviolet region, which accounts for a negligible portion of the solar spectrum. Although Bi_2WO_6 possesses significant light harvesting and photoexcited electron transmission capabilities in the field of photocatalytic methods, its use has been severely limited by chemical corrosion [19,29–31]. Various approaches like incorporating heteroatom, nitrogen vacancy, morphology controlling,

combining with other semiconductor and forming a heterojunction structure by coupling with g-C_3N_4 or other graphene containing compound can enhance the photoactivity which can be follow to overcome these shortcomings, some are discussed in the following sections [32].

1.1.2 Carbon based materials:

Carbon nitride (C_3N_4) was initially developed by Berzelius in 1834 and is one of the earliest artificial polymers in scientific literature. An early form of melon, a linear polymer composed of interconnected tri-s-triazine units linked by secondary nitrogen, was synthesised by him. The material was subsequently designated by Liebig [33]. The application of g-C_3N_4 in heterogeneous catalysis was started around 20 years ago [34].

Graphitic carbon nitride (g-C_3N_4) is a metal-free photocatalyst characterised by a two-dimensional (2D) layered structure, wherein carbon and nitrogen atoms form a π-π conjugated electronic framework with sp^2 hybridisation, subsequently stacking to make a three-dimensional crystal structure. The basic structure considers two units, one is s-triazine (C_3N_3) and the other is tri-s-triazine (C_6N_7) as depicted in **Scheme 1.4**

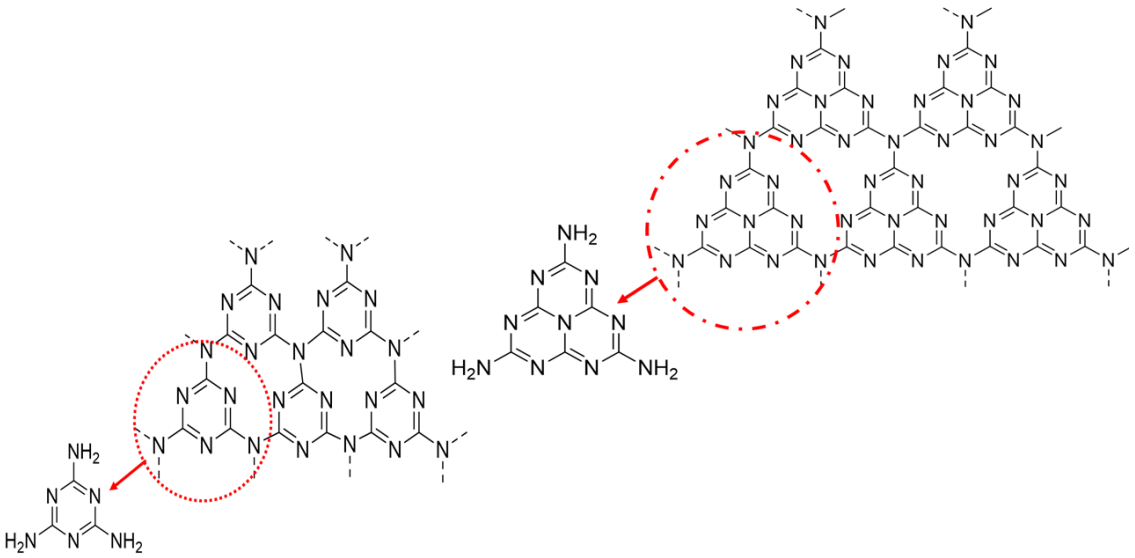

Scheme 1.4: Graphitic carbon nitride structure having s-triazine and tri-s-triazine units[35]

Bulk g-C_3N_4 can be synthesised through direct thermal condensation method using organic compound containing nitrogen group like urea, cyanamide, dicyandiamide and melamine[35]. The advantages include environmental friendliness, facile synthesis, affordability, high stability, and being one of the prime materials responsive to visible light having 2.7 eV bandgap which utilizes solar spectrum [33,36]. For photocatalytic activity, band position values are the main affecting factor, generally the CB (conduction band) and VB (valence band) values are −1.3 eV and + 1.4 eV respectively with 460 nm absorption edge make the material more efficient for visible light absorption. Hence this unique band

structure own excellent photodegradation efficiency for many organic pollutants compared to TiO_2 and other semiconductor [17,37]. The photoactivity is further depend on the microstructure, absorption ability, yield of the material, therefore different precursor used for synthesising g-C_3N_4 shows different activity. Usually, thiourea yields less negative zeta value of g-C_3N_4 and with urea the yield is very low around 1-5 % but have larger surface area with extremely superior photoactivity in pollutant degradation and hydrogen production [38,39]. The photocatalytic process carries three steps: Firstly, light is irradiated on the g-C_3N_4 surface and electron will excite to the conduction band (CB) leaving behind holes in the valence band (VB), now these charge carriers will move to the surface of the catalyst where redox reaction take place. In an aqueous solution, dissolved oxygen serves as an electron acceptor, whereas H_2O/OH^- functions as an electron donor. Reactive oxygen species (ROS), such as superoxide anions (O_2^-) and hydroxyl radicals ($^{\cdot}OH$), are produced, leading to the degradation of organic contaminants into nontoxic products [40–42].

Based on the aforementioned modification techniques, Bi_2WO_6 can be coupled with the polymeric semiconductor g-C_3N_4 to enhance its photocatalytic activity and expand the research on Bi_2WO_6 as stated by Ge *et al.* [43]. Han *et al.* reported Co_3O_4/g-C_3N_4 heterojunction photocatalyst to degrade methyl orange using visible light source [44].

In recent years, two-dimensional (2D) graphene has seeking attention because of the intriguing physical properties, like electrochemical modulation, high elasticity, extremely high mobility, quantum electronic transport [45,46], hence due to its hydrophobic nature, remarkable structure and large surface area. The increased photocatalytic activity for the elimination of different organic contaminants is confirmed by the formation of composites containing organic/inorganic semiconductor nanoparticles, metallic nanoparticles, and metal-organic frameworks[47].

When rGO is combined with another semiconductor, its electrical property facilitates the charge transfer process via the conjugated system and ultimately prevent the recombination rate of charge particles[48,49]. Liang *et al.* reported the degradation of levofloxacin by plasmonic Bi and rGO co-modified Bi_5O_7I, in which rGO plays both the role of pollutant adsorption to increase degradation efficiency as well as electron collector for boosting charge separation [50]. Kasinathan *et al*. fabricated Bi_2MoO_6/N-rGO catalyst to degrade harmful dyes, in which nitrogen present on graphene enhances the photoactivity [51]. Another report by Liu *et al*. constructed a ternary nanocomposite Ag decorated 3D flower shaped Bi_2MoO_6/rGO for the removal of organic pollutants [52].

1.1.3 Modification of bismuth-based materials:

In semiconductor photocatalysis, the charge carriers (electron and hole) produced by absorption of light could recombine and also absorption of light is very low, hence these two features result in poor degradation efficiency for organic pollutants. Therefore, to enhance the photoactivity and desired capability of photocatalyst, some modifications are required like increasing the bismuth amount, construction of heterojunction structure [53], interface modification [54], creating oxygen vacancies [55], interaction between different metal oxide of bismuth etc. [56].

Heterojunction structures are formed by mixing two or more semiconductor (**Scheme 1.5**) at nanoscale using some specific synthesis method like solvothermal, hydrothermal, coprecipitation, solid state, wet impregnation etc. In recent times, these structures are proved to be the best method for inhibiting the recombination of charge carriers and absorption of light in wider region compared to one semiconductor, both of them can effectively boost up the photo activity. The combination of the semiconductor aligns the band potential in such a way that they come in the vicinity which prevent the recombination of active species (electrons and holes). It also supports the matching of valence band (VB) and conduction band (CB) of semiconductors with desired energy potential for pollutant degradation. Different type of heterojunctions structures is there such as Type-II, Z-Scheme (traditional Z-scheme, all solid-state Z-scheme, direct Z-scheme), S-scheme [53]. Numerous bismuth-based metal oxide semiconductor heterojunction structure has been synthesised that can be categorized as n-n [57] and n-p [58] type depends upon their constituent semiconductor.

Li *et al*. has fabricated g-C_3N_4/$BiVO_4$ type-II and S-Scheme heterostructure with different faces of $BiVO_4$ to degrade methylene blue in 120 min, in which only 1% g-C_3N_4 loading increase the efficiency by 2.3 times [59]. For the degradation of nonylphenol ethoxylate, Dong *et al*. reported the synthesis of 10wt.% loading of g-C_3N_4 over $BiVO_4$ forming Z-Scheme heterojunction showed highest activity for degrading the organic pollutant [60]. Using visible light source and tetracycline antibiotic as a pollutant, Wei *et al*. degrade it up to 95.3% in 40 min and other pollutants Congo Red (anionic dye) and Crystal Violet (cationic dye) over 98.5% by utilizing rGO@Ag_2O/Bi_2WO_6 heterostructure composite. It also worked well over broad pH range [61].

Bismuth loaded Bismuth tungstate (Bi/Bi_2WO_6) has been reported to degrade tetracycline hydrochloride, an organic pollutant by Huang *et al*., they have synthesised the material using hydrothermal method and also studied the controlled molar ratio of Bi $(NO_3)_3$ to Bi_2WO_6 for formation of different amount (by moles) loaded Bi metal over Bi_2WO_6 [62]. One pot hydrothermal method was adopted by Zhou *et al*. to synthesised Bi/ Bi_2WO_6 /reduced graphene oxide nanocomposite and used ethylene glycol (EG) which play dual role, a solvent as well as to reduced GO. Rhodamine B was

utilized to degrade in visible light by the as prepared photocatalyst. The significant performance is corresponding to the SPR effect of Bi, visible light active Bi_2WO_6, effective charge transfer heterojunction and electrically conductive nature of rGO [45].

Successful fabrication of 3D/2D Bi_2MoO_6/g-C_3N_4 heterostructure by Kasinathan *et al.* using solvothermal method to degrade harmful dyes under visible light shows 94 % and 92% degradation efficiency for Rhodamine B and Methylene blue respectively, which is better than bare Bi_2MoO_6 and /g-C_3N_4 [63].

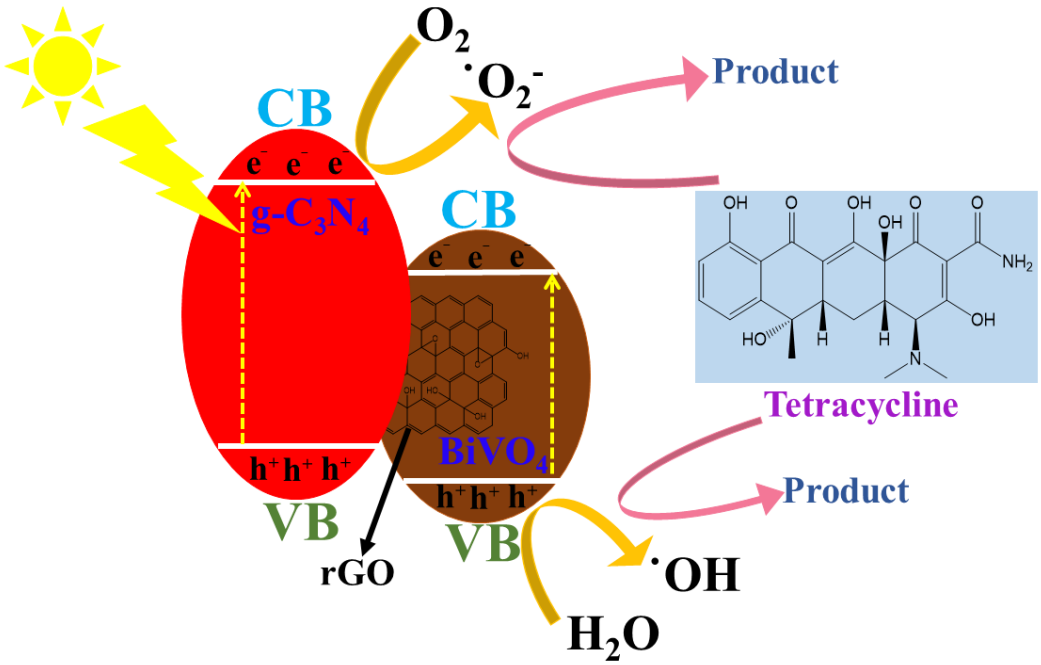

Scheme 1.5: Degradation of Tetracycline hydrochloride antibiotic by heterostructure of Bismuth based composite.

A novel ternary composite Pd loaded g-C_3N_4@Bi_2MoO_6 were synthesised by Wang *et al*. via graphitic nitride coupling using solvothermal precipitation followed by calcination and Pd-metal doped by photoreduction method. The metal here not only prevent the recombination rate of h^+/e^- but also increase optical harvesting ability through SPR effect, which significantly increase catalytic activity to degrade pollutants [64]. Also, by changing morphology of the nanomaterial, photocatalytic activity can be enhanced as reported by Zhang *et al*. that preparation of Bi_2WO_6 nanoparticles using different pH condition shows different photocatalytic activity. In acidic condition, (at pH= 1,3 and 5) obtained nanosheet like structure and in basic condition, (at pH= 9,11 and 13) microrods like morphology and at pH= 7, nanoplates with more thickness can be synthesised. The morphology in acidic range shows 12 times higher photocatalytic activity than basic range [65]. Wang *et al*. stated that using one-step solvothermal method to synthesize rose like Bi_2WO_6 loaded with TiO_2 and doped with Sb^{+3} exhibit

outstanding photoelectric conversion property, also decompose methylene blue, methyl orange and rhodamine B efficiently. Moreover, 93.8 % Cr (IV) ions were also removed under solar radiation by using this nanocomposite [66]. Various other heterojunction structure and metal loaded photocatalysts of bismuth-based material are successfully fabricated [67–69].

1.2 Research gap:

On the basis of literature studies, following research gaps have been realized which will be addressed in the present research proposal.

There are reports on graphitic nitride (g-C_3N_4), reduced graphene oxide (rGO) which behaved as catalyst and composites with bismuth but not vast studies have done on their heterojunction structure or nanocomposites.

For the degradation of organic pollutants, treatment of water sources, degradation of pharmaceutical waste, pesticides, dyes etc., there is a requirement of superior, efficient, reliable and easy synthesis methods. The synthesised material should have strong thermal and chemical stability, adjustable band gap, good photoelectric properties. These nanocomposites including graphitic carbon like material (g-C_3N_4, rGO, GO etc.) with bismuth-based compounds such as g-C_3N_4/$BiVO_4$, g-C_3N_4/Bi_2O_3, g-C_3N_4/Bi_2WO_6 etc. or rGO/ bismuth-based compounds. So along with these features of the nanocomposite, some modification in the morphology, structure of nanomaterial, like hollow tubular structure, nanorods, nanotubes, nano mesh, flower shape etc. is required.

Also, as per our knowledge or literature study, there are no reports on the synthesis of self-reduction of metal without addition of any reducing agent. In addition to the precious metals (Ag, Cu and Au), non-noble elements reveal significant LSPR effects. Non-noble metal like bismuth (Bi) shows a surface plasmon resonance (SPR) behaviour characterised by significant resonant absorption of visible light. Moreover, bismuth is cost-effective, non-toxic and electric conductive compared to other precious metals. Furthermore, the superior photocatalytic activity of nanocomposites compared to the bare analogues has been primarily attributed to the lower band gap and prevention of electron/hole pair recombination, but improvement of other properties like changes in charge transfer resistance has not been explored much.

Hence, based on the above-mentioned research gaps, my research will focus on these research limitations, which include the photocatalytic activity in visible or natural sunlight and UV light. Hence, by the use of nanocomposites, heterojunction structure is constructed from the self-reduction of bismuth present in the bismuth-based semiconductor. Therefore, by studying the photodegradation

process and kinetics, harmful organic and inorganic water pollutants produced by pharmaceutical and dyeing industries can be removed by using the above-mentioned photocatalyst.

1.3 Objectives:

1. Preparation and characterization of the graphitic carbons (g-C_3N_4, rGO etc.), bimetallic bismuth oxides ($BiVO_4$, Bi_2WO_6 etc.) and their composites.
2. Tuning the composition of the heterostructures to afford desired surface morphology and physicochemical properties.
3. Evaluation of adsorption and photocatalytic activities of these composites towards organic pollutants.

1.4 Methodology:

1.4.1 Synthesis of Bimetallic bismuth oxide (BBO)

(a) Homogeneous precipitation method:

In this method, the bismuth containing salt [Bi $(NO_3)_3 \cdot 5H_2O$] was dissolved in acid [HNO_3] which undergo ultrasonication treatment and the other precursor was then added into the solution and then kept the mixture on stirring so that the entire solution formed a homogeneous mixture. After that, slow addition of urea into the reaction mixture was taken place, which control the particle size and minimize the agglomeration. Now placed the mixture at heating in oil bath for one day. Then filtered the mixture, washed with distilled water and ethanol multiple times and dried at 60 ℃ overnight. Detail is given in the Chapter-2 under the heading "Preparation of $BiVO_4$" section **2.2.2**

(b) Hydrothermal method:

In this method, the salt precursor of bismuth [Bi $(NO_3)_3 \cdot 5H_2O$] is dissolved in distilled water along with some compound or surfactant. The second precursor was then added to the above mixture and then placed the reaction in an autoclave at high temperature for some specific time. After that, centrifuged and dried at 60 ℃. The procedure is in brief in Chapter-3 under heading "Preparation of Bi_2WO_6" section **3.2.2**

(c) Solvothermal method:

This procedure involved a chemical reaction occurring in an organic solvent at a temperature above the boiling point of solvent. The metal precursors were dissolved in an organic solvent in this process.

The whole mixture was thereafter transferred to an autoclave for hydrothermal treatment at a certain temperature for a defined duration. Detailed procedure is in Chapter-4 under section **4.2.2** with the heading as "Preparation of Bi_2MoO_6".

1.4.2 Synthesis of g-C_3N_4 (g-CN)

(a) Tandem Method

50 mL of DI water and 12 g of urea were mixed in a mortar pestle and then heated for 12 h at 60 °C to facilitate recrystallization. After recrystallizing, it was covered in aluminium foil and heated for 2 h at 550 °C at a rate of 10 °C per min. The obtained brownish-coloured g-C_3N_4 was ground into a powdered form. Detail is given in the respective Chapter-2 and 3

(b) One pot

30 g urea in a crucible was heated at 5 ℃/min at 500 ℃ for 2 h then again to 550 ℃ at 10 ℃/min for another 2 h. After cooling down naturally, the obtained pale yellow-coloured powder was ground into bulk g-C_3N_4. The bulk g-C_3N_4 was dispersed in ethanol for 1 h using ultrasonication to attain g-C_3N_4 sheets, then the solution was filtered and dried at 50 ℃. Detail is given in the respective Chapter-4

1.4.3 Synthesis of g-CN loaded bimetallic bismuth oxide-based composites

(a) Wet impregnation method

In this method, the desired amount of one material (bimetallic bismuth oxide) is dispersed in a solvent (distilled water, methanol, ethanol etc.) then add required weight percentage loading amount of another material (g-CN) into the above solution and kept under sonication for half or one hour. Then stirred the reaction mixture for 24 h. Afterwards, centrifuged and dried at required temperature. Details are present in the respective Chapters-2 and 4 under the section **2.2.4** and **4.2.4** respectively.

(b) Wet impregnation followed by calcination

This method consists the necessary amount of bimetallic bismuth oxide mixed with water and followed by sonication for 1 h. After that, solution kept on stirring for 24 h. Now, separate the mixture by centrifugation and dried at 70 ℃. After drying, the product is now calcined at a specific temperature in a furnace. Details are present in Chapter-3 under the section **3.2.4**

1.5 Characterization technique

Various modified methods have employed to synthesis the pristine bimetallic bismuth oxide (BBO), graphitic nitride (g-CN) and g-CN/BBO with different weight percentage loading nanocomposites

(experimental details are given in the related chapters). The synthesized catalysts were subsequently examined through several characterisation to evaluate their structural, physicochemical and surface properties.

1.5.1 X-ray diffraction (XRD):

The phase purity and crystallographic properties were recorded using Xpert pro-Cu-Kα (1.54 Å), diffractometer at 45 kV with an angle (2θ) range 10°-75°.

1.5.2 Fourier transform infrared spectroscopy (FTIR):

To study the structural information of the photocatalysts, Shimadzu, IRTracer-100 was used to record the Fourier transform infrared spectra.

1.5.3 Dynamic light scattering (DLS):

The hydrodynamic size was recorded using dynamic light scattering technique, (ZEN 3600, Malvern, U.K.) to study the electrokinetic characteristic of the as prepared catalyst. The size was measured by using disposable cuvette containing 2 mg catalyst dispersed in 10 mL distilled water.

1.5.4 Morphology study:

The structural morphology was determined by using field emission scanning electron microscopy (FESEM, Carl-Zeiss Sigma 500 FEG-SEM), along with energy dispersive spectroscopy (EDS, BRUKER) for finding elemental composition. HRTEM (High-resolution transmission electron microscopy, JEOL JEM 2100 plus) for confirming the detailed morphology of the synthesised material.

1.5.5 Surface area determination:

The surface area of the as prepared samples was analysed by BET (Brunauer Emmett-Teller): (i) Quanta chrome Nova 2200e) and (ii) Microtrac Belsorp Mini-II (Bel, Japan, Inc.).

1.5.6 Optical studies:

The optical absorbance bandgap (DRS, diffuse reflectance studies) was obtained by using (i) UV-visible spectrophotometer (Shimadzu UV-2600) and (ii) JASCO V-750 Spectrophotometer with utilizing $BaSO_4$ as a reference standard and halogen lamp as a light source.

1.5.7 X-ray photon spectroscopy (XPS):

The oxidation state and elemental composition was determined by using (i) X-ray photon spectroscopy, (XPS, Thermo Fischer Scientific ESCALAB Xi) and (ii) XPS, Omicron ESCA make Oxford Instrument Germany.

1.5.8 Electrochemical study:

Electrochemical impedance spectroscopy (EIS) tests were conducted using a Biologic VSP300 potentiostat by adjusting parameters: a frequency range of 1 Hz to 1000 Hz operating in the dark mode, and a standard Ag/AgCl reference electrode in 0.5 M Na_2SO_4 solution and varying voltage in chapters 2-4

1.5.9 Mass spectrometry:

The intermediate detection was studied by HRMS (High resolution mass spectrometer, Waters [QTOF] with UPLC (XEVO G2 XS) and Ion source Combined APCI having both positive and negative ESI mode at different time intervals).

1.5.10 Demineralisation study:

To detect the demineralisation efficiency of the pollutant during degradation reaction, Total organic carbon measurement was carried out by using the Analytikjena TOC/TNb analyser, series 300 and also used Hach COD digestor DRB200, open reflux method followed by APHA 4200 (21edition) for chemical oxygen demand.

1.6 Adsorption and photocatalytic studies:

In the adsorption and photodegradation experiments, an optimised amount of catalyst was introduced into a test tube containing an aqueous solution of a particular pollutant, which was subsequently placed in both dark and light irradiation for a period of time duration. At specific time intervals, the catalyst was removed from the pollutant solution using centrifugation, and the remaining pollutant concentration was evaluated using a UV-visible spectrophotometer (Shimadzu UV-2600).

To predict the reaction kinetics of photodegradation, pseudo zero and first-order kinetic models were examined. The explained procedures and respective equations are thoroughly elaborated in their corresponding chapters for better understanding.

1.7 Scavenger's study:

The role of reactive species in degradation process is confirmed by performing the Scavenger's experiment. For that, various scavengers such as EDTA (5 mg), NH_4SCN (5 mg), iPA (5 mL), Ar gas purging (15-20 minutes) has been used to monitor their effects on photocatalytic degradation activity. To perform the experiment, different batches having different scavengers were used and given same optimized condition. Batch I has the reaction mixture (RM) along with EDTA, batch II has RM + iPA, batch III has RM + NH_4SCN and batch IV has RM + Ar gas purging covered with a septum and after that followed the same photocatalytic degradation experiment.

References:

1 X. Liu, S. Gu, Y. Zhao, G. Zhou and W. Li, $BiVO_4$, Bi_2WO_6 and Bi_2MoO_6 photocatalysis: A brief review, *J. Mater. Sci. Technol*., 2020, **56**, 45.

2 S. N. Ahmed and W. Haider, Heterogeneous photocatalysis and its potential applications in water and wastewater treatment: a review, *Nanotechnol.*, 2018, **29**, 342001.

3 P. Rajasulochana and V. Preethy, Comparison on efficiency of various techniques in treatment of waste and sewage water – A comprehensive review, *Res. Eff. Technol*., 2016, **2**, 175.

4 G. Veréb, L. Manczinger, A. Oszkó, A. Sienkiewicz, L. Forró, K. Mogyorósi, A. Dombi and K. Hernádi, Highly efficient bacteria inactivation and phenol degradation by visible light irradiated iodine doped TiO_2, *Appl. Catal. B.*, 2013, **129**, 194.

5 S. Mishra and B. Sundaram, A review of the photocatalysis process used for wastewater treatment, *Mater.Today Proc.*, 2024, **102**, 393.

6 Q. Xiang, F. Cheng and D. Lang, Hierarchical Layered WS_2/Graphene-Modified CdS Nanorods for Efficient Photocatalytic Hydrogen Evolution, *Chem. Sus.Chem.*, 2016, **9**, 996.

7 A. Bellucci, P. Calvani, M. Girolami, S. Orlando, R. Polini and D. M. Trucchi, Optimization of black diamond films for solar energy conversion, *Appl. Surf. Sci.*, 2016, **380**, 8.

8 X. She, J. Wu, H. Xu, J. Zhong, Y. Wang, Y. Song, K. Nie, Y. Liu, Y. Yang, M. T. F. Rodrigues, R. Vajtai, J. Lou, D. Du, H. Li and P. M. Ajayan, High Efficiency Photocatalytic Water Splitting Using 2D α-Fe_2O_3/g-C_3N_4 Z-Scheme Catalysts, *Adv. Energy Mater.*, 2017, **17**, 1700025.

9 M. Baradaran, F. E. Ghodsi, C. Bittencourt and E. Llobet, The role of Al concentration on improving the photocatalytic performance of nanostructured ZnO/ZnO:Al /ZnO multilayer thin films, *J. Alloys Compd.*, 2019, **788**, 289.

10 X. Kong, C. Zeng, X. Wang, J. Huang, C. Li, J. Fei, J. Li and Q. Feng, Ti-O-O coordination bond caused visible light photocatalytic property of layered titanium oxide, *Sci. Rep.*, 2016, **6**, 29049.

11 A. Meng, L. Zhang, B. Cheng and J. Yu, Dual Cocatalysts in TiO_2 Photocatalysis, Adv. Mater., 2019, **31,** 1807660.

12 X. Kong, Q. Lu, J. Huang, L. Li, J. Zhang, X. Wang, J. Li, Y. Wang and Q. Feng, Visible light photocatalytic property and mechanism of peroxy bond incorporated layered $H_4Nb_6O_{17}$ niobate, *J. Alloys Compd.*, 2018, **746**, 68.

13 T. Di, B. Cheng, W. Ho, J. Yu and H. Tang, Hierarchically CdS–Ag_2S nanocomposites for efficient photocatalytic H_2 production, *Appl. Surf. Sci.*, 2019, **470**, 196.

14 Q. Xiang, D. Lang, T. Shen and F. Liu, Graphene-modified nanosized Ag_3PO_4 photocatalysts for enhanced visible-light photocatalytic activity and stability, *Appl. Catal. B.*, 2015, **162**, 196.

15 Y. Zhou, G. Chen, Y. Yu, Y. Feng, Y. Zheng, F. He and Z. Han, An efficient method to enhance the stability of sulphide semiconductor photocatalysts: a case study of N-doped ZnS, *Phys. Chem. Chem. Phys.*, 2015, **17**, 1870.

16 R. He, D. Xu, B. Cheng, J. Yu and W. Ho, Review on nanoscale Bi-based photocatalysts, *Nanoscale Horiz.*, 2018, **3**, 464.

17 S. S. M. Bhat and H. W. Jang, Recent Advances in Bismuth-Based Nanomaterials for Photoelectrochemical Water Splitting, *Chem.Sus.Chem.*, 2017, **10**, 3001.

18 M. Batool, M. F. Nazar, A. Awan, M. B. Tahir, A. Rahdar, Bismuth-based heterojunction nanocomposites for photocatalysis and heavy metal detection applications, A. E. Shalan, S. Lanceros-Méndez and M. N. Zafar, *Nano-Struct. Nano-Objects.*, 2021, **27**, 100762.

19 Q. Y. Tang, R. Huo, L. Y. Ou, X. L. Luo, Y. R. Lv and Y. H. Xu, One-pot synthesis of peony-like $Bi_2S_3/BiVO_4$ (040) with high photocatalytic activity for glyphosate degradation under visible light irradiation, *Chinese J. Catal.*, 2019, **40**, 580.

20 H. Sun, C. Zou and W. Tang, Designing double Z-scheme heterojunction of g-$C_3N_4/Bi_2MoO_6/Bi_2WO_6$ for efficient visible-light photocatalysis of organic pollutants, *Colloids Surf. A. Physicochem. Eng. Asp.*, 2022, **654**, 130105.

21 F. Opoku, K. K. Govender, C. G. C. E. van Sittert and P. P. Govender, Insights into the photocatalytic mechanism of mediator-free direct Z-scheme g-C_3N_4/Bi_2MoO_6 (010) and g-C_3N_4/Bi_2WO_6 (010) heterostructures: A hybrid density functional theory study, *Appl. Surf. Sci.*, 2018, **427**, 487.

22 A. Murthy, A Review on Eco-Friendly Synthesis of $BiVO_4$ Nanoparticle and its Eclectic Application, *Adv. J. Sci. Eng.*, 2020, **1,** 106.

23 Y. Zhou, Y. Zhang, M. Lin, J. Long, Z. Zhang, H. Lin, J. C. S. Wu and X. Wang, Monolayered Bi_2WO_6 nanosheets mimicking heterojunction interface with open surfaces for photocatalysis, *Nat. Commun.*, 2015, **6**, 8340.

24 X. Ding, W. Ho, J. Shang and L. Zhang, Self-doping promoted photocatalytic removal of no under visible light with bi2moo6: Indispensable role of superoxide ions, *Appl. Catal. B.*, 2016, **182**, 316.

25 J. Wang, Y. X. Feng, M. Zhang, C. Zhang, M. Li, S. J. Li, W. Zhang and T. B. Lu, β-Cyclodextrin Decorated CdS Nanocrystals Boosting the Photocatalytic Conversion of Alcohols, *CCS Chem.*, 2020, **2**, 81.

26 M. Moradi, F. Hasanvandian, A. A. Isari, F. Hayati, B. Kakavandi and S. R. Setayesh, CuO and ZnO co-anchored on g-C_3N_4 nanosheets as an affordable double Z-scheme nanocomposite for photocatalytic decontamination of amoxicillin, *Appl. Catal. B.*, 2021, **285**, 119838.

27 J. Mei, Y. Tao, C. Gao, Q. Zhu, H. Zhang, J. Yu, Z. Fang, H. Xu, Y. Wang and G. Li, Photo-induced dye-sensitized $BiPO_4$/BiOCl system for stably treating persistent organic pollutants, *Appl. Catal. B.*, 2021, **285**, 119841.

28 W. Zou, X. H. Liu, C. Xue, X. T. Zhou, H. Y. Yu, P. Fan and H. B. Ji, Enhancement of the visible-light absorption and charge mobility in a zinc porphyrin polymer/g-C_3N_4 heterojunction for promoting the oxidative coupling of amines, *Appl. Catal. B.*, 2021, **285**, 119863.

29 Y. Ma, Y. Jia, Z. Jiao, M. Yang, Y. Qi and Y. Bi, Hierarchical Bi_2MoO_6 nanosheet-built frameworks with excellent photocatalytic properties, *Chem. Commun*., 2015, **51**, 6655.

30 K. Jing, J. Xiong, N. Qin, Y. Song, L. Li, Y. Yu, S. Liang and L. Wu, Development and photocatalytic mechanism of monolayer Bi_2MoO_6 nanosheets for the selective oxidation of benzylic alcohols, *Chem. Commun*., 2017, **53**, 8604.

31 Y. Hao, X. Dong, S. Zhai, X. Wang, H. Ma and X. Zhang, Controllable self-assembly of a novel Bi_2MoO_6-based hybrid photocatalyst: excellent photocatalytic activity under UV, visible and near-infrared irradiation, *Chem.Comm.*, 2016, **52**, 6525.

32 P. Niu, L. Zhang, G. Liu and H. M. Cheng, Graphene-Like Carbon Nitride Nanosheets for Improved Photocatalytic Activities, *Adv. Funct. Mater*., 2012, **22**, 4763.

33 Y. Zhao and J. Zhang, Qu. L, Graphitic Carbon Nitride/Graphene Hybrids as New Active Materials for Energy Conversion and Storage, *Chem. Nano. Mat.*, 2015, **1**, 298.

34 F. Goettmann, A. Fischer, M. Antonietti and A. Thomas, Metal-free catalysis of sustainable Friedel–Crafts reactions: direct activation of benzene by carbon nitrides to avoid the use of metal chlorides and halogenated compounds, *Chem. Commun.*, 2006, 4530.

35 M. Zhang, Y. Yang, X. An and L. an Hou, A critical review of g-C_3N_4-based photocatalytic membrane for water purification, *Chem. Eng. J.*, 2021, **412**,128663.

36 J. Wen, J. Xie, X. Chen and X. Li, A review on g-C_3N_4-based photocatalysts, *Appl. Surf. Sci.*, 2017, **391**, 72.

37 B. Xu, M. B. Ahmed, J. L. Zhou, A. Altaee, G. Xu and M. Wu, Graphitic carbon nitride-based nanocomposites for the photocatalysis of organic contaminants under visible irradiation: Progress, limitations and future directions, *Sci. Total Environ*., 2018, **633**, 546.

38 B. Zhu, P. Xia, W. Ho and J. Yu, Isoelectric point and adsorption activity of porous g-C_3N_4, *Appl. Surf. Sci.*, 2015, **344**, 188.

39 H. Lan, L. Li, X. An, F. Liu, C. Chen, H. Liu and J. Qu, Microstructure of carbon nitride affecting synergetic photocatalytic activity: Hydrogen bonds vs. structural defects, *Appl. Catal. B.*, 2017, **204**, 49.

40 B. Xu, M. B. Ahmed, J. L. Zhou, A. Altaee, G. Xu and M. Wu, Graphitic carbon nitride-based nanocomposites for the photocatalysis of organic contaminants under visible irradiation: Progress, limitations and future directions, *Sci. Total Environ*., 2018, **633**, 546.

41 A. Sudhaik, P. Raizada, P. Shandilya, D. Y. Jeong, J. H. Lim and P. Singh, Review on fabrication of graphitic carbon nitride based efficient nanocomposites for photodegradation of aqueous phase organic pollutants, *J. Ind. Eng. Chem., 2018, **67**,* 28.

42 S. Yu, Y. Wang, F. Sun, R. Wang and Y. Zhou, Novel mpg-C_3N_4/TiO_2 nanocomposite photocatalytic membrane reactor for sulfamethoxazole photodegradation, *Chem. Eng. J.*, 2018, **337**, 183.

43 L. Ge, C. Han and J. Liu, Novel visible light-induced g-C_3N_4/Bi_2WO_6 composite photocatalysts for efficient degradation of methyl orange, *Appl. Catal. B.*, 2011, **108**, 100.

44 C. Han, L. Ge, C. Chen, Y. Li, X. Xiao, Y. Zhang and L. Guo, Novel visible light induced Co_3O_4-g-C_3N_4 heterojunction photocatalysts for efficient degradation of methyl orange, *Appl. Catal. B: Environ*., 2014, **147**, 546.

45 Y. Zhou, S. Ren, Q. Dong, Y. Li and H. Ding, One-pot preparation of Bi/Bi_2WO_6/reduced graphene oxide as a plasmonic photocatalyst with improved activity under visible light, *RSC Adv.*, 2016, **6**, 102875.

46 D. Fang, X. Li, H. Liu, W. Xu, M. Jiang, W. Li and X. Fan, $BiVO_4$-rGO with a novel structure on steel fabric used as high-performance photocatalysts, *Sci. Rep.*, 2017, **7**, 7979.

47 R. Suresh, R. V. Mangalaraja, H. D. Mansilla, P. Santander and J. Yanez, Reduced Graphene Oxide-Based Photocatalysis, *Environ. Chem. Sustain. World*, 2019, **34**,145.

48 Y. Zhang, D. Li, Y. Zhang, X. Zhou, S. Guo and L. Yang, Graphene-wrapped $Bi_2O_2CO_3$ core–shell structures with enhanced quantum efficiency profit from an ultrafast electron transfer process, *J. Mater. Chem. A. Mater.*, 2014, **2**, 8273.

49 X. Pan, Y. Zhao, S. Liu, C. L. Korzeniewski, S. Wang and Z. Fan, Comparing Graphene-TiO_2 Nanowire and Graphene-TiO_2 Nanoparticle Composite Photocatalysts, *ACS Appl. Mater. Interfaces*, 2012, **4**, 3944.

50 C. Liang, C. G. Niu, L. Zhang, X. J. Wen, S. F. Yang, H. Guo and G. M. Zeng, Construction of 2D heterojunction system with enhanced photocatalytic performance: Plasmonic Bi and reduced graphene oxide co-modified Bi_5O_7I with high-speed charge transfer channels, *J. Hazard Mater.*, 2019, **361**, 245.

51 M. Kasinathan, S. Thiripuranthagan, A. Sivakumar, S. Ranganathan, T. Vembuli, S. Kumaravel and E. Erusappan, Fabrication of novel Bi_2MoO_6/N-rGO catalyst for the efficient photocatalytic degradation of harmful dyes, *Mater. Res. Bull*, 2020, **125**, 110782.

52 X. Liu, W. Y. Huang, Q. Zhou, X. R. Chen, K. Yang, D. Li and D. D. Dionysiou, Ag-decorated 3D flower-like Bi_2MoO_6/rGO with boosted photocatalytic performance for removal of organic pollutants, *Rare Met.*, 2021, **40**, 1086.

53 H. Chawla, A. Chandra, P. P. Ingole and S. Garg, Recent advancements in enhancement of photocatalytic activity using bismuth-based metal oxides Bi_2MO_6 (M = W, Mo, Cr) for environmental remediation and clean energy production, *J. Ind. Eng. Chem.*,2021, **95**, 1.

54 M. Iwasaki, M. Hara, H. Kawada, H. Tada and S. Ito, Cobalt Ion-Doped TiO_2 Photocatalyst Response to Visible Light, *J. Colloid Interface Sci.*, 2000, **224**, 202–204.

55 Z. Lv, H. Zhou, H. Liu, B. Liu, M. Liang and H. Guo, Controlled assemble of oxygen vacant CeO_2@Bi_2WO_6 hollow magnetic microcapsule heterostructures for visible-light photocatalytic activity, *Chem. Eng. J.*, 2017, **330**, 1297.

56 Z. Zhang, T. Zheng, J. Xu, H. Zeng and N. Zhang, Carbon Quantum Dots/Bi_2WO_6 Composites for Efficient Photocatalytic Pollutant Degradation and Hydrogen Evolution, *Nano.*, 2017, **12**, 7

57 M. S. Gui, W. De Zhang, Y. Q. Chang and Y. X. Yu, One-step hydrothermal preparation strategy for nanostructured WO_3/Bi_2WO_6 heterojunction with high visible light photocatalytic activity, *Chem. Eng. J.*, 2012, **197**, 283.

58 Z. Zhang, C. Shao, X. Li, C. Wang, M. Zhang and Y. Liu, Electrospun Nanofibers of p-Type NiO/n-Type ZnO Heterojunctions with Enhanced Photocatalytic Activity, *ACS Appl. Mater. Interfaces*, 2010, **2**, 2915.

59 X. Li, G. Fang, Q. Tian and T. Wu, Crystal regulation of $BiVO_4$ for efficient photocatalytic degradation in g-C_3N_4/$BiVO_4$ heterojunction, *Appl. Surf. Sci.*, 2022, **584**, 152642.

60 S. Dong, G. J. Lee, R. Zhou and J. J. Wu, Synthesis of g-C_3N_4/$BiVO_4$ heterojunction composites for photocatalytic degradation of nonylphenol ethoxylate, *Sep. Purif. Technol.*, 2020, **250**, 117202.

61 J. Wei, Z. Chen and Z. Tong, Synthesis of g-C_3N_4/$BiVO_4$ heterojunction composites for photocatalytic degradation of nonylphenol ethoxylate, *J. Colloid Interface Sci.*, 2021, **596**, 22.

62 X. Huang, M. Li, Y. Guo, L. Li and Y. Wu, Hollow nest-like Bi/Bi2WO6 photocatalyst with coupled active effects of SPR and defective oxygen, *Mater. Sci.: Mater. Electron.*, 2022, **33**, 19447.

63 M. Kasinathan, S. Thiripuranthagan and A. Sivakumar, Fabrication of 3D/2D Bi_2MoO_6/g-C_3N_4 heterostructure with enhanced photocatalytic behaviour in the degradation of harmful organics, *Emerg. Mater.*, 2021, **4**, 1363.

64 M. Wang, Y. Zhang, C. Jin, Z. Li, T. Chai and T. Zhu, Fabrication of novel ternary heterojunctions of Pd/g-C_3N_4/Bi_2MoO_6 hollow microspheres for enhanced visible-light photocatalytic performance toward organic pollutant degradation, *Sep. Purif. Technol.*, 2019, **211**, 1.

65 L. Zhang, T. Xu, X. Zhao and Y. Zhu, Controllable synthesis of Bi_2MoO_6 and effect of morphology and variation in local structure on photocatalytic activities, *Appl. Catal. B.*, 2010, **98**, 138.

66 Q. Wang, H. Li, X. Yu, Y. Jia, Y. Chang and S. Gao, Morphology regulated Bi_2WO_6 nanoparticles on TiO_2 nanotubes by solvothermal Sb^{3+} doping as effective photocatalysts for wastewater treatment, *Electrochim. Acta*., 2020, **330**, 135167.

67 C. Pan, J. Xu, Y. Wang, D. Li and Y. Zhu, Dramatic Activity of $C_3N_4/BiPO_4$ Photocatalyst with Core/Shell Structure Formed by Self-Assembly, *Adv. Funct. Mater.*, 2012, **22**, 1518.

68 Y. Wang, D. Yu, W. Wang, P. Gao, L. Zhang, S. Zhong and B. Liu, *Colloids Surf. A. Physicochem. Eng. Asp.*, The controllable synthesis of novel heterojunction $CoO/BiVO_4$ composite catalysts for enhancing visible-light photocatalytic property, *Colloids Surf. A: Physicochem. Eng. Asp.*, 2019, **578**, 123608.

69 Z. Wang, X. Cai, X. Xie, S. Li, X. Zhang and Z. Wang, Visible-LED-light-driven photocatalytic degradation of ofloxacin and ciprofloxacin by magnetic biochar modified flower-like Bi_2WO_6: The synergistic effects, mechanism insights and degradation pathways, *Sci. Total Environ*., 2021, **764**, 142879.

CHAPTER-2

CHAPTER-2

Fabrication of g-C_3N_4 loaded $BiVO_4$ binary nanocomposites for the photocatalytic removal of Rhodamine B.

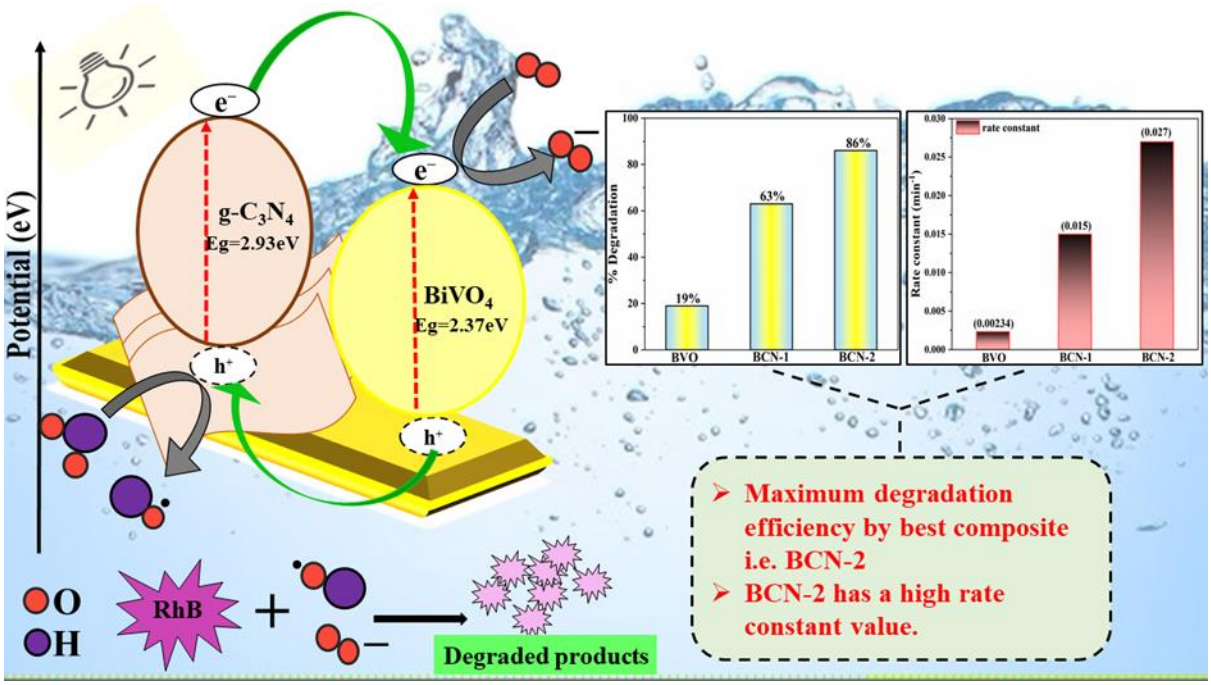

Schematic outline:

In this chapter, g-C_3N_4 loaded $BiVO_4$ type-II heterojunction structure have been synthesized using wet impregnation method exhibit high photocatalytic activity in 60 minutes in visible light towards rhodamine B dye.

2.1 Introduction:

Water contamination has played a significant role in the recent increase in worldwide environmental pollution, which is primarily due to the textile industry. According to studies, between 10-12% of the dyes are classified as hazardous waste, with Rhodamine B being one of the contaminants[1,2]. Rhodamine B, a member of the xanthene family, is frequently employed in the textile industry due to its stability, solubility in water, and brightness[3]. Even at smaller concentrations (1 ppm), the dye has a detrimental impact on the aquatic environment[4]. The dye has a dangerous and mutagenic effect in that it harms people by affecting their brain, central nervous system, liver, and kidneys[5]. As a result, many techniques for their removal have been developed [6].

The reliable method for removing toxins from water is thought to be semiconductor-based photocatalysts. $BiVO_4$ has emerged as an excellent photocatalyst due to its narrow band gap (2.4 eV), low toxicity, corrosion resistance, chemical stability, etc.[7,8]. The photoactivity of bare $BiVO_4$ is not very significant due to the rapid electron-hole pair recombination rate and smaller specific surface area [9]. Therefore, combining it with other materials, such as metals and non-metals, to create composites with heterojunction structures has now emerged as a great option[10]. Such methodologies result in an improvement of the sensitivity towards visible light and a reduction in electron-hole pair recombination. Numerous investigations have shown that composites have higher photocatalytic activity than bare $BiVO_4$[11]. Due to the potential and fundamental physical characteristics, graphitic nitride (g-C_3N_4), a 2D layered and metal-free structured material, is currently attracting a lot of interest[12–16]. Fabrication heterojunction interface allows the effective separation of photogenerated electrons and holes. Additionally, the direction of charge transfer changes in accordance with the semiconductor's band position[17]. The development of the heterojunction structure of both semiconductors has proven to be an appropriate solution; as a result of the band positions of g-C_3N_4 and $BiVO_4$ matching, the separation of charge and recombination rate is effectively controlled and also enhances the photocatalytic activity[18]. There have not been many reports on the wet chemical methods used to create a composite of $BiVO_4$/g-C_3N_4 with varying weight ratios, whose photocatalytic performance was examined.

2.2 Experimental:

2.2.1 Chemicals:

All the chemicals Bismuth nitrate pentahydrate 98% [Bi $(NO_3)_3.5H_2O$], Ammonium metavanadate 99% [NH_4VO_3], Urea 99% extra pure, Rhodamine B. [RhB], N-Methyl-2-pyrrolidone (NMP) were procured from Loba Chemie, India. The carbon black (CB) powder, polyvinylidene fluoride (PVDF), and fluorinated tin oxide (FTO) glasses (resistance < 10 ohm) were purchased from Nanoshell, Sigma Aldrich, and Vitra Technologies, respectively. Ethanol (absolute) 99.9% was obtained from Changshu Hongsheng Fine Chemicals Co. Ltd. Deionized water was prepared using Milli-Q, Millipore ultrafiltration system.

2.2.2 Preparation of $BiVO_4$:

$BiVO_4$ (denoted as BVO) was prepared by homogeneous precipitation method, in which Bi $(NO_3)_3.5H_2O$ [6 mmol] was dispersed in a 32 mL aqueous solution of 1M HNO_3 using ultrasonication. After that, NH_4VO_3 [6 mmol] was added to the above solution and strenuously stirred for 1 h. Subsequently, 3 g urea was added and heated the mixture at 80 ℃ using an oil bath for 24 h. then yellow-color precipitate was filtered and washed with DI water & ethanol and dried at 60 ℃ overnight[9].

2.2.3 Preparation of g-C_3N_4:

In a crucible, 12 g of urea was added to 50 mL of DI water and placed in an oven at 60 ℃ (12 h) for recrystallization. After recrystallization, covered it properly with aluminium foil and placed it in a muffle furnace for 2 h at 550 ℃ with a 10℃/min rise in temperature. A light brownish-colored solid product of g-C_3N_4 was grounded as a fine powder and denoted as g-CN[19].

2.2.4 Preparation of g-CN loaded BVO composite:

The composite was prepared by wet impregnation chemical followed by solvent evaporation method[20,21]. For the synthesis of g-C_3N_4@$BiVO_4$ composite, firstly dispersed 50 mg $BiVO_4$ in 20 mL ethanol and the mixture was sonicated for 1 h. After 1 h, the required amount of g-C_3N_4 was added to the mixture and sonicated for another 1 h then the mixture was kept for stirring for 24 h. Now, the obtained composite was kept in an oven at 50 ℃ for drying. The composite is abbreviated as BCN-1 for 5 wt.% loading of g-CN@BVO and BCN-2 for 10 wt.% loading of g-CN@BVO.

2.2.5 Preparation of Thin Films:

The films for the EIS Nyquist plot were prepared on FTO glass by drop cast method. Initially, 1 mg of PVDF and 40-60 µL NMP were mixed thoroughly to result in a uniform paste then 1 mg CB was added to this mixture and blended further for 20 minutes. Subsequently, 8 mg of the active material (BVO or

BCN-2) was also added and combined further to obtain a homogeneous mixture, which was drop-casted into a clean FTO. The coated FTO substrate was dried at 80 ℃ overnight.

2.2.6 Photocatalytic activity evaluation:

The toxic pollutant RhB (Rhodamine B) was chosen to scrutinize the photocatalytic properties of as prepared $BiVO_4$ and its composite prepared by 5 wt.% loading of g-CN@BVO (named as BCN-1) and 10 wt.% loading of g-CN@BVO (named as BCN-2). In a typical experiment, 7.5 mg of the photocatalyst was added to a test tube containing 5 ml of RhB solution (0.0183 mM) at room temperature. Before the photocatalytic degradation experiment, the suspension was stirred in the dark for 30 minutes to attain the adsorption-desorption equilibrium. After that, the test tube was illuminated with visible light irradiation (Wipro Garnet B22-50watt LED bulb, λ>360 nm) for monitoring degradation at fixed time intervals. By centrifugation, catalysts were separated out and the concentration of RhB pollutant was examined in the corresponding solution using a UV-Vis spectrophotometer (Shimadzu UV-2600). The following equation was used to calculate the degradation efficiency:

$$\text{Degradation efficiency (\%)} = \frac{\boldsymbol{C_0 - C_t}}{\boldsymbol{C_0}} \times \mathbf{100}$$

Where $\mathbf{C_0}$ is the initial concentration of pollutant

$\mathbf{C_t}$ is concentration after 't' time

2.2.7 Characterization technique:

The crystallographic properties were recorded by X-ray diffraction (XRD) using Xpert pro-Cu-Kα (1.54 Å) at 45 kV with a diffraction angle 2θ (15°-65°). The structural morphology was investigated with field emission scanning electron microscopy (FESEM, Carl-Zeiss Sigma 500 FEG-SEM) and EDS (energy dispersive spectroscopy) for elemental composition by BRUKER and high-resolution transmission electron microscopy (HRTEM, JEOL JEM 2100 plus). The optical absorption spectra of bare BVO and its composites (BCN-1 and BCN-2) were studied with a diffuse reflectance spectrophotometer (solid state, Shimadzu UV-2600). The hydrodynamic size was recorded with a zeta potential analyzer (ZEN 3600, Malvern, U.K.). The oxidation state was confirmed by X-ray Photoelectron spectroscopy (XPS, Thermo Fischer Scientific ESCALAB Xi). The N_2 adsorption-desorption was carried out by (Quanta chrome Nova 2200e). The band gaps were determined by monitoring its diffused reflectance spectra (DRS) using UV-visible spectrophotometer (Shimadzu UV-2600). The intermediates were detected by HRMS (Waters, QTOF mass spectrometer with UPLC (XEVO G2 XS) and Ion source - Combined ESI and APCI source

with positive and negative mode scans, at different time intervals, retention time 8 minutes). The electrochemical impedance spectroscopy (EIS) experiments were performed at a voltage of 0.7 V vs RHE in the frequency range from 1 Hz to 1000 Hz using a Biologic VSP300 potentiostat under dark. The BVO and BCN-2 loaded FTO were used as the working electrode, Pt as the counter electrode, and the standard calomel electrode as the reference electrode in 0.5 M Na_2SO_4 (pH=6.5). FTIR was recorded by IRTracer-100 (Fourier Transform Infrared Spectrophotometer, Shimadzu)

2.3 Result and discussion:

2.3.1 XRD studies

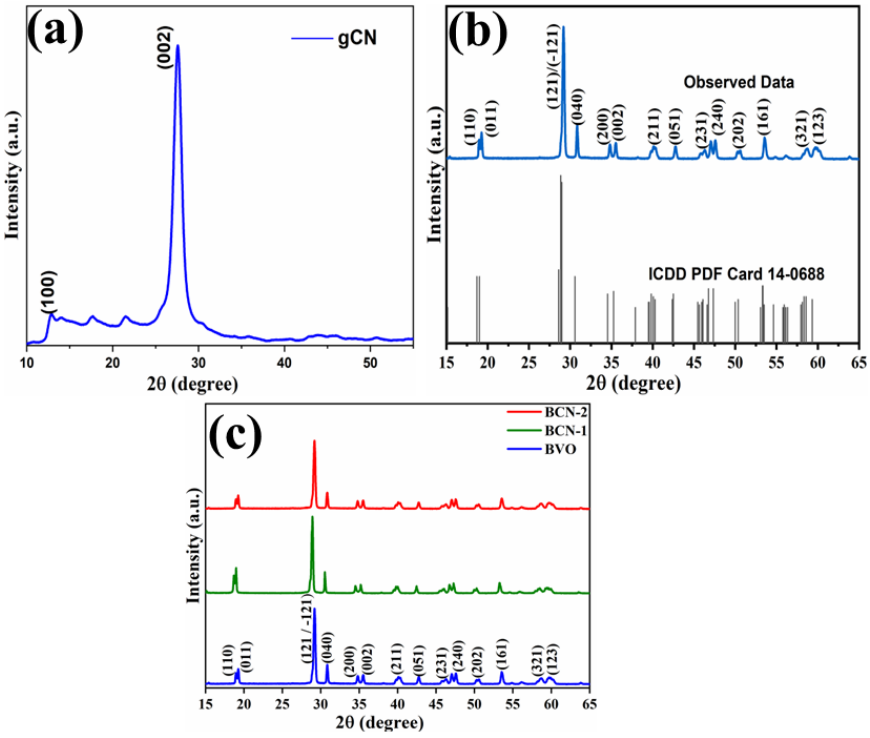

Fig. 2.1: XRD patterns of (a) g-CN, (b) BVO and (c) BVO, BCN-1 and BCN-2 composites.

XRD analyzed the phase structure of samples, **Fig. 2.1a** contains the XRD pattern of g-CN in which the strong intensity peak lies at the (002) plane at 27.9° and another peak at 12.7° for the (100) plane[19] and there are two extra peaks in the diffraction field of 15°-25° which could be due to the crystallographic planes in the graphitic nitride layered structure[22]. It could be seen that the bare $BiVO_4$ **(Fig. 2.1 b)** was in good agreement with the monoclinic scheelite phase (ICDD PDF card number 14-0688) [9]. In **Fig. 2.1b**, the peaks indicate the presence of no phase impurity, as evidenced by the absence of any extra diffraction

peak. The XRD pattern for the composites, BCN-1 and BCN-2 **(Fig. 2.1 c)** is exactly similar to the bare BVO and has no corresponding peak of g-CN. Such observation is quite reasonable as g-CN has a much smaller x-ray scattering coefficient than BVO. It also confirms that upon loading of g-CN in the BVO surface, there is no significant effect on its structural integrity[23,24].

2.3.2 XPS analysis

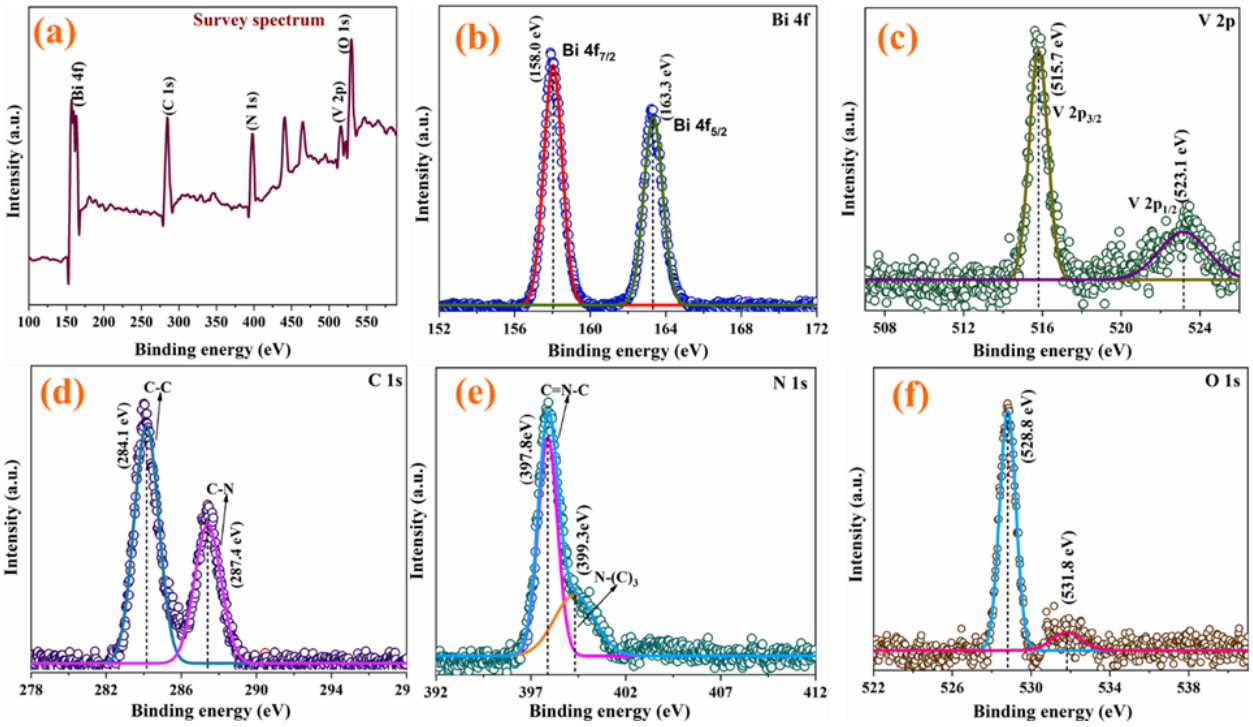

Fig. 2.2. XPS spectra of BCN-2 composite showing (a) survey spectrum. The elemental peaks of (b) Bi 4f (c) V 2p (d) C 1s (e) N 1s (f) O 1s respectively of the synthesized catalyst.

The XPS plot of g-CN doped $BiVO_4$ composite (BCN-2) is shown in **Fig. 2.2**. The survey diagram in **Fig. 2.2a**, indicates the presence of elements Bi, C, N, V and O in the composite. The peaks at 158.0 eV and 163.3 eV binding energy correspond to Bi ($4f_{7/2}$) and Bi ($4f_{5/2}$), respectively, validating Bi's trivalent oxidation state **Fig. 2.2b**[25,26]. In **Fig. 2.2c,** The V $2p_{3/2}$ (515.7 eV) and $2p_{1/2}$ (523.1 eV) signals can be ascribed to the V^{5+} species[27,28]. As observed in **Fig. 2.2d,** the XPS spectrum of C 1s has peaks at 284.1 eV and 287.4 eV, which are characteristic of the C-C bond and C-N bond, respectively, in which C attached to the $-NH_2$ group and is in sp^2 state in aromatic ring[29]. Meanwhile, the allocation of the peak at 397.8 eV in **Fig. 2.2e** was assigned to N-atom in triazine rings (C=N-C) having sp^2 hybridization and a less intense

peak at high binding energy of 399.3 eV consisting of centered/bridged sp^2 N-atom which is further attached to C- atom like N-$(C)_3$ [30,31]. **Fig. 2.2f** represents the XPS spectrum of O 1s in which the peaks were deconvoluted into two peaks with binding energy at 528.8 eV and 531.8 eV, which are characteristic of the lattice oxygen and surface-absorbed water, respectively [30,32]. The absence of any other elements confirms the chemical purity of the g-CN/$BiVO_4$ composite.

2.3.3 Optical property

To determine the optical bandgap, the UV-Vis diffuse reflectance spectrum of the as-prepared photocatalysts was recorded. As shown in **Fig. 2.3a**, the bare $BiVO_4$ shows the absorption edge at 516 nm, which is in good agreement with the reported result[9]. The bandgap energy of the bare $BiVO_4$ photocatalyst is determined with the help of a Tauc's plot, as shown in **Fig. 2.3b**. With the increase in the loading of g-CN[22], the bandgap gradually decreases from 2.37 eV ($BiVO_4$) to 2.30 eV (BCN-2).

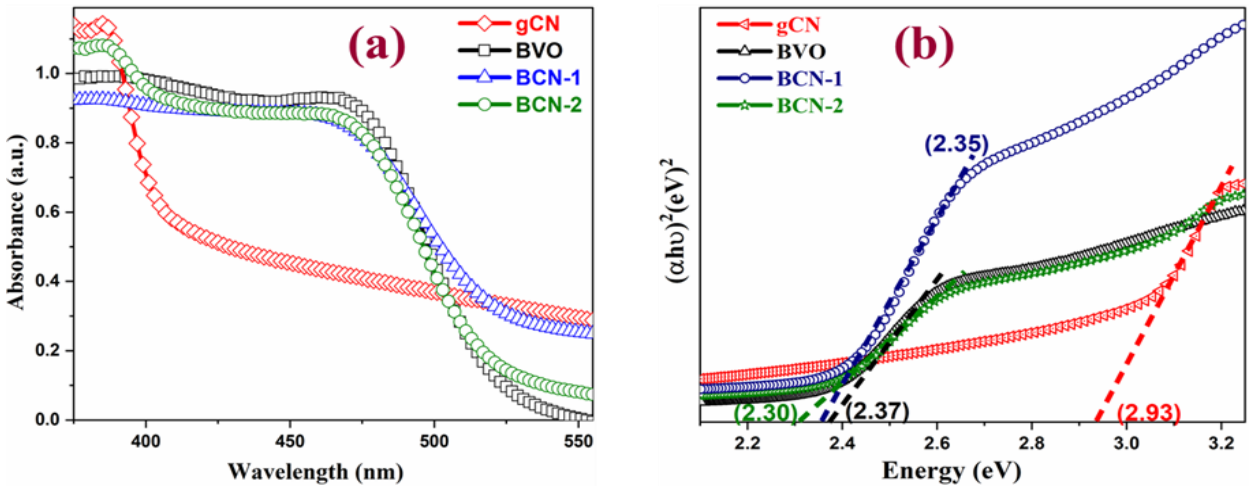

Fig. 2.3: (a) UV-Vis diffuse reflectance spectra of the prepared photocatalyst, (b) Tauc's Plot of the as-synthesized catalysts.

2.3.4 EIS measurements

In order to investigate the change transfer characteristics, the electrochemical impedance spectroscopic (EIS) measurements were carried out for BVO and the BCN-2 composites in the dark. It has been noticed that the Nyquist plot of the BCN-2 composite has smaller radii than the pristine BVO **(Fig. 2.4)**. Such observation suggests that the BCN-2 composite has a lower charge transfer resistance than the original BVO.

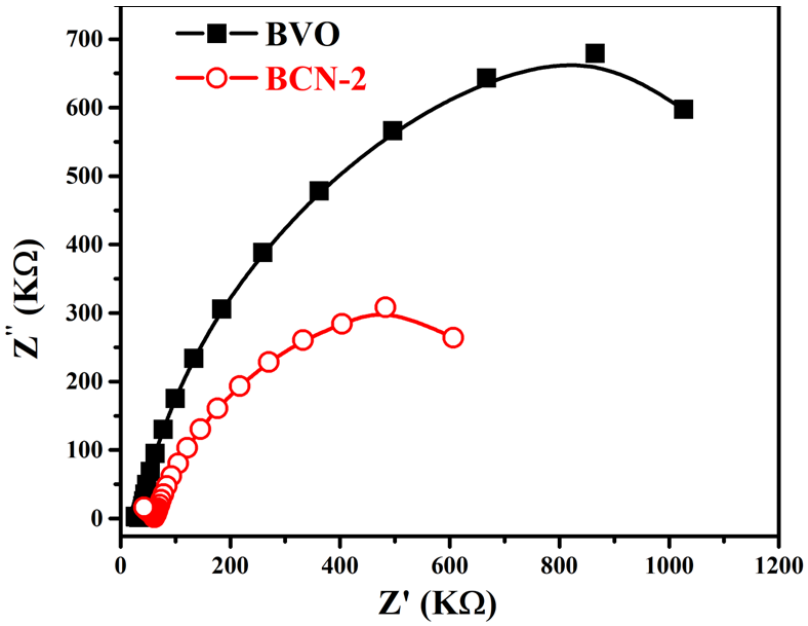

Fig. 2.4: EIS Nyquist plots of BVO and BCN-2 composite

2.3.5 Morphology and Multielemental analysis

SEM images were recorded to investigate the morphology of the pure $BiVO_4$ and its composite with g-C_3N_4 by the loading amount (10 wt.%) of g-CN@$BiVO_4$, named BCN-2 shown in **Fig. 2.5**. It was noticed that the morphology of bare $BiVO_4$ sample exhibit decagonal shape in **Fig. 2.5 (a-b)** where the well-formed crystal displayed sharp edges and smooth surface[9]. The average particle size of BVO was found to be 225 nm, shown in **Fig. 2.6**. The FE-SEM image of the BCN-2 composite demonstrates the presence of both deposition of $BiVO_4$ crystals and CN layers **[Fig. 2.5 (c-e)]**[19], thereby confirming the formation of the composite. In HRTEM, the dark grey-colored portions represent the BVO, whereas the light grey areas correspond to the g-CN sheets. The HRTEM images clearly show the deposition of g-CN sheets over the $BiVO_4$, particles. Moreover, the lattice fringes of 0.49 nm in **Fig.2.7c** were assigned to the (110) plane of $BiVO_4$[18] which showed that its crystallinity is retained in the composite. The EDS mapping of the prepared samples was analyzed to determine the elemental composition present in the samples. The EDS mapping shows the particular region over which the distribution of the different elements was present, as shown in **Fig. 2.8** and **Fig. 2.9** for $BiVO_4$ and BCN-2 composite (which contains C, N, Bi, V, O) respectively.

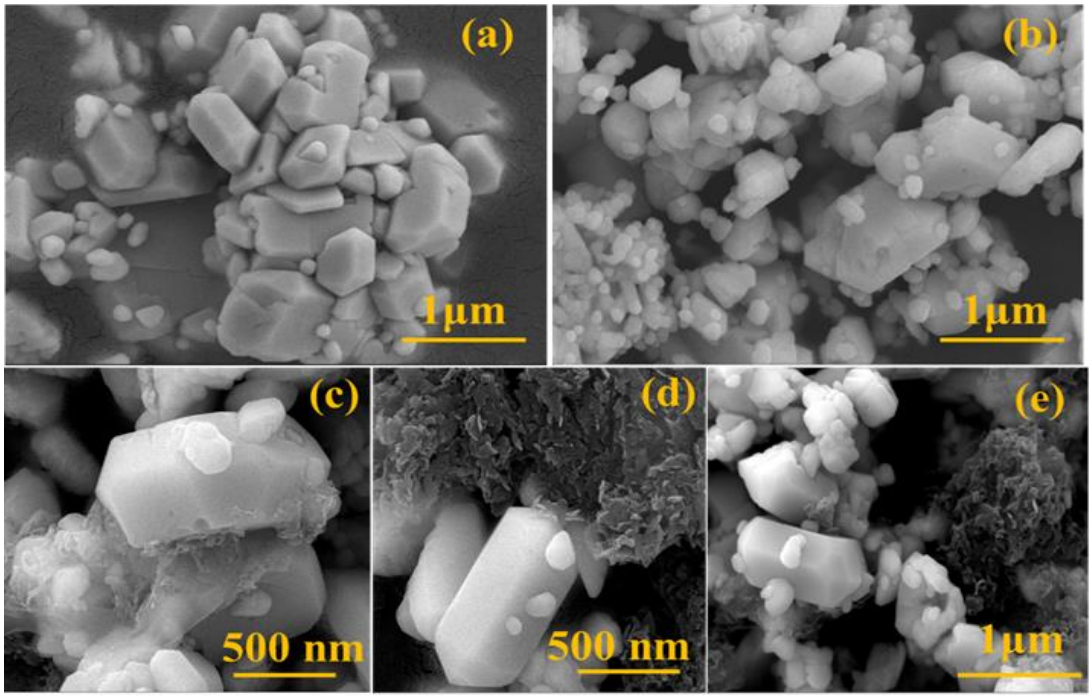

Fig. 2.5: FE-SEM images of BVO (a and b) and BCN-2 composite (c, d and e).

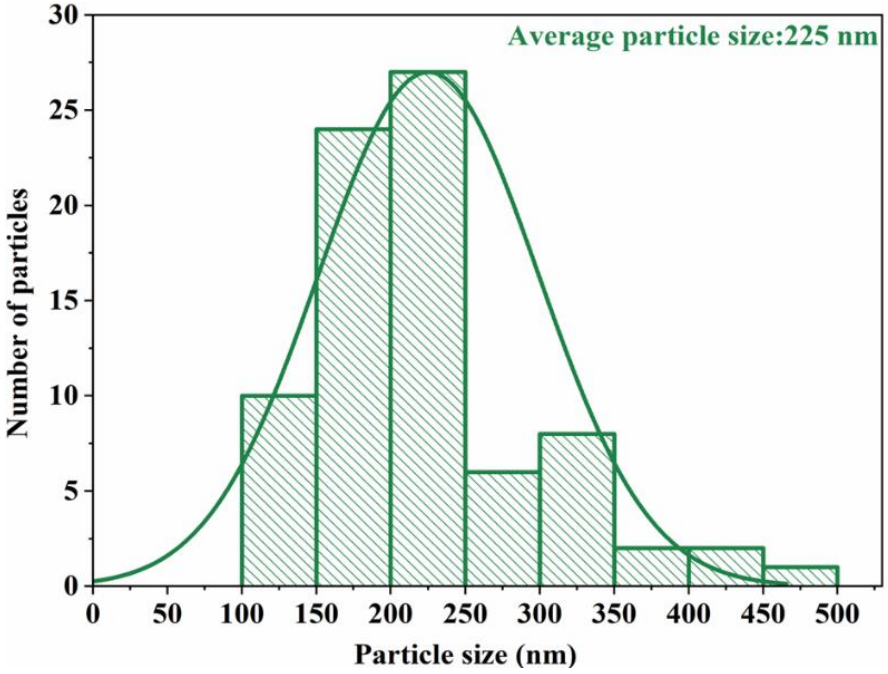

Fig. 2.6: Average particle size of $BiVO_4$.

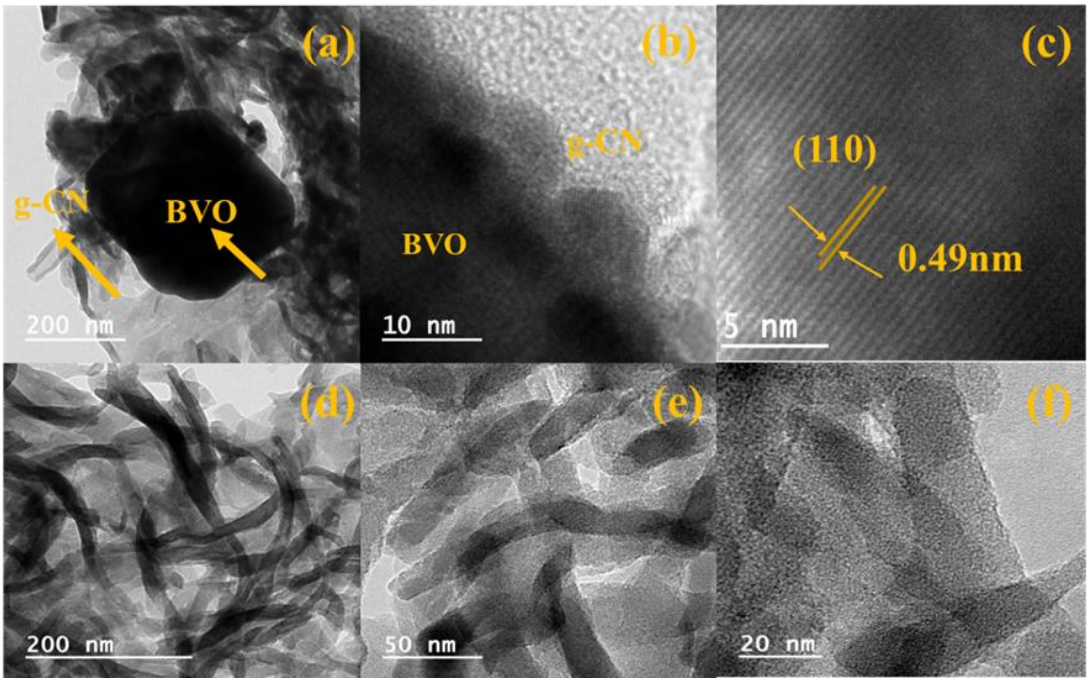

Fig. 2.7: HRTEM images of BCN-2 (a and b), lattice fringes (c) and g-CN (d, e, f).

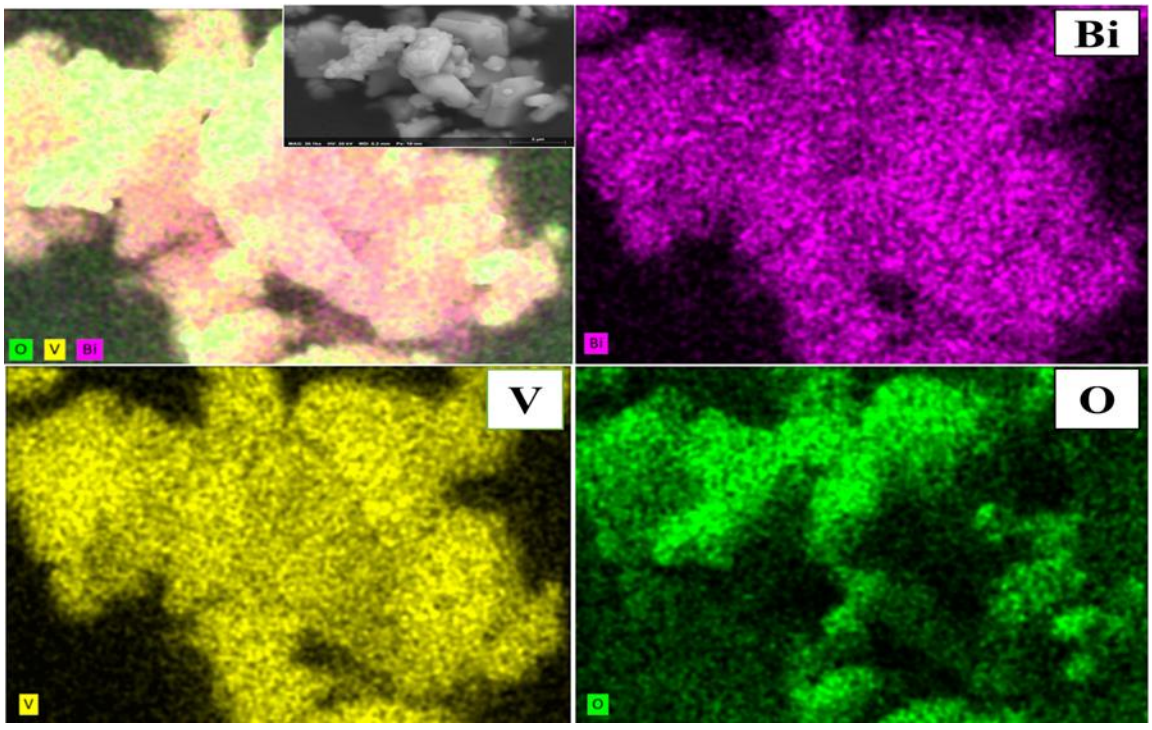

Fig. 2.8: EDS mapping of bare $BiVO_4$ showing the presence of elements Bi, V and O.

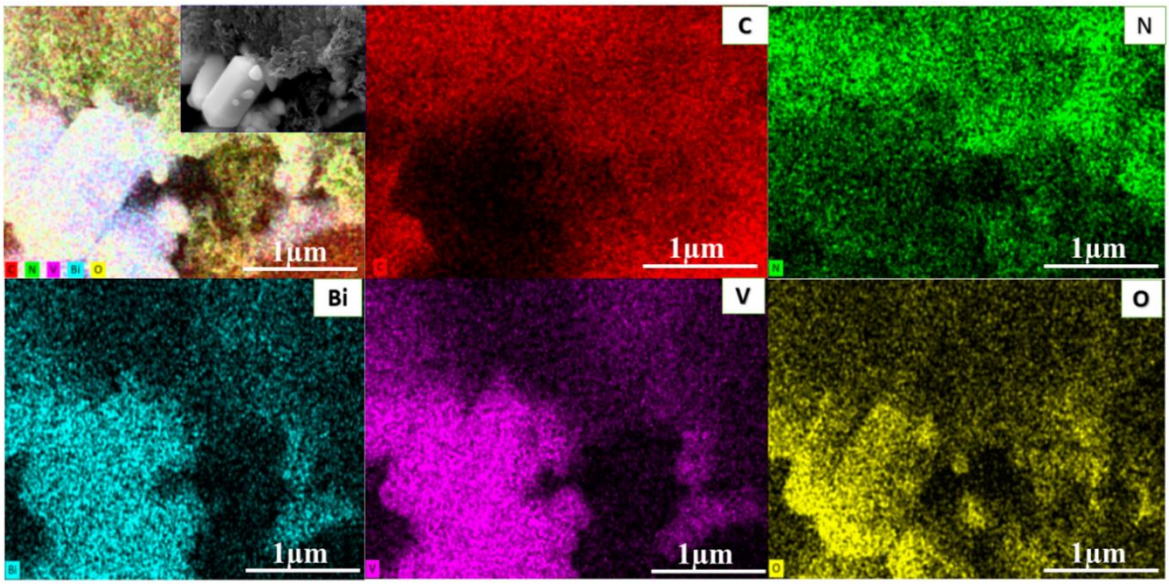

Fig. 2.9: Elemental dot mapping of BCN-2 composite, showing the presence of elements Bi, V, O, C and N.

The hydrodynamic particle size of the photocatalyst can be recorded with the Dynamic light scattering technique. It was found that the hydrodynamic sizes of the particles are 612 nm, 639 nm, and 684 nm, for $BiVO_4$, BCN-1, and BCN-2, respectively **(Fig. 2.10)**. The increase in the size is due to the loading of layered g-CN sheets on $BiVO_4$.

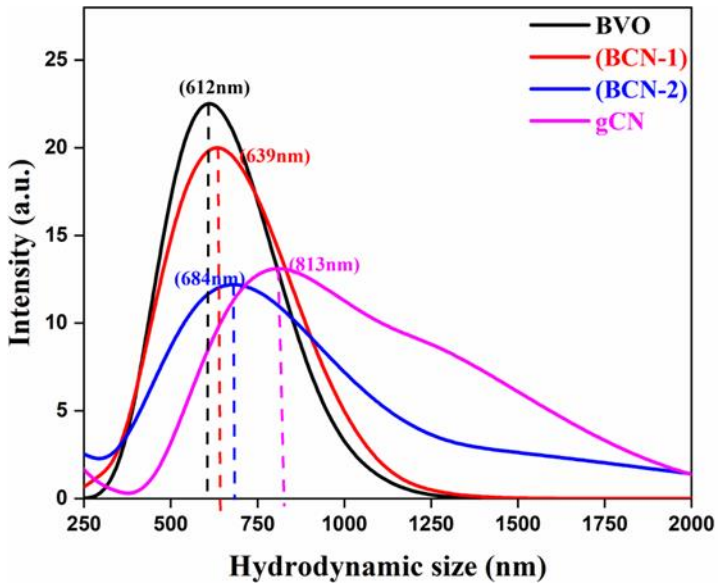

Fig. 2.10: Hydrodynamic size of photocatalyst and their composites.

2.3.6 N_2 adsorption-desorption Analysis

Using BET analysis, the surface properties of the as-prepared material were analyzed (**Fig. 2.11**). The prepared samples consisted of type-III adsorption-desorption isotherm having an H3 hysteresis loop[33]. The surface area of $BiVO_4$ is 6.7 m^2/g and the BCN-2 composite is 13.4 m^2/g in **Fig. 2.11b,** respectively. The loading of graphitic nitride on $BiVO_4$ enhances the number of active sites, thereby increasing the specific surface area. So, the composite can act as a superior photocatalyst due to its higher surface area[34].

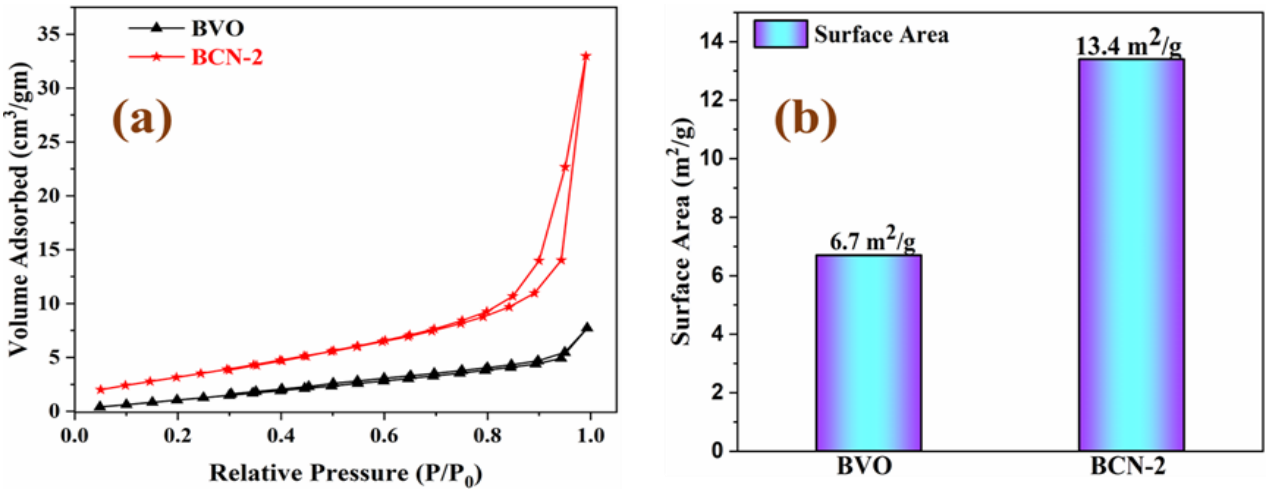

Fig. 2.11: N_2 adsorption-desorption isotherm of (a) $BiVO_4$ and BCN-2 composite respectively, (b) Surface area of $BiVO_4$ and BCN-2 respectively.

2.3.7 Photocatalytic degradation

RhB was adopted as the model pollutant for the photodegradation experiment to evaluate the photocatalytic activity of synthesized composite in the presence of visible light[35] (**Fig. 2.12**). The initial concentration of RhB was 0.0183 mM. Before illuminating the light, the reaction mixture was stirred for 30 minutes in the dark to attain adsorption-desorption equilibrium. After 60 min the $BiVO_4$ was given only ~19% degradation efficiency. The BCN-1 and ~63% and BCN-2 composite is ~86% in 60min.

To evaluate the rate constant, the following equation[35]

$$\ln\left(\frac{C}{C_0}\right) = -kt$$

was followed and **Table 1** shows the rate constant values, **Fig. 2.12d** shows the bar plot of rate constant values of different synthesized samples

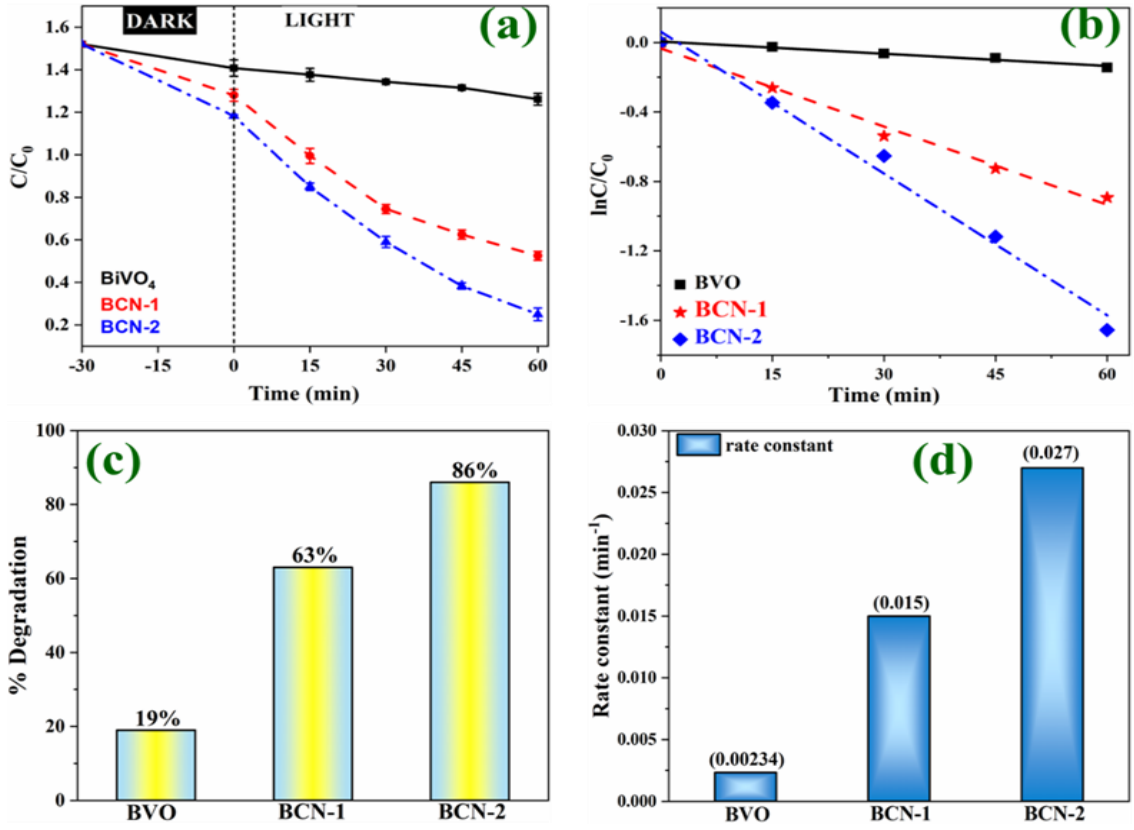

Fig. 2.12: Photocatalytic degradation of RhB with time (a) and showing trends with ln C/C_0 and at different time intervals of bare BVO, BCN-1 and BCN-2 composites respectively (b), (c) represents the bar graph of RhB degradation efficiency and (d) showing the bar graph of rate constant values of BVO, BCN-1 and BCN-2 respectively.

Table 1:

Samples	Rate Constant ,k (min^{-1})	Degradation Efficiency	R-square
BVO	0.00234	~19%	0.973
BCN-1	0.015	~63%	0.984
BCN-2	0.027	~86%	0.981

The kinetic study of bare BVO, g-CN and BCN-1 and BCN-2 composite is shown in **[Fig. 2.13 (a-d)].** It has been concluded that the BCN-2 composite displayed the maximum degradation efficiency in visible light.

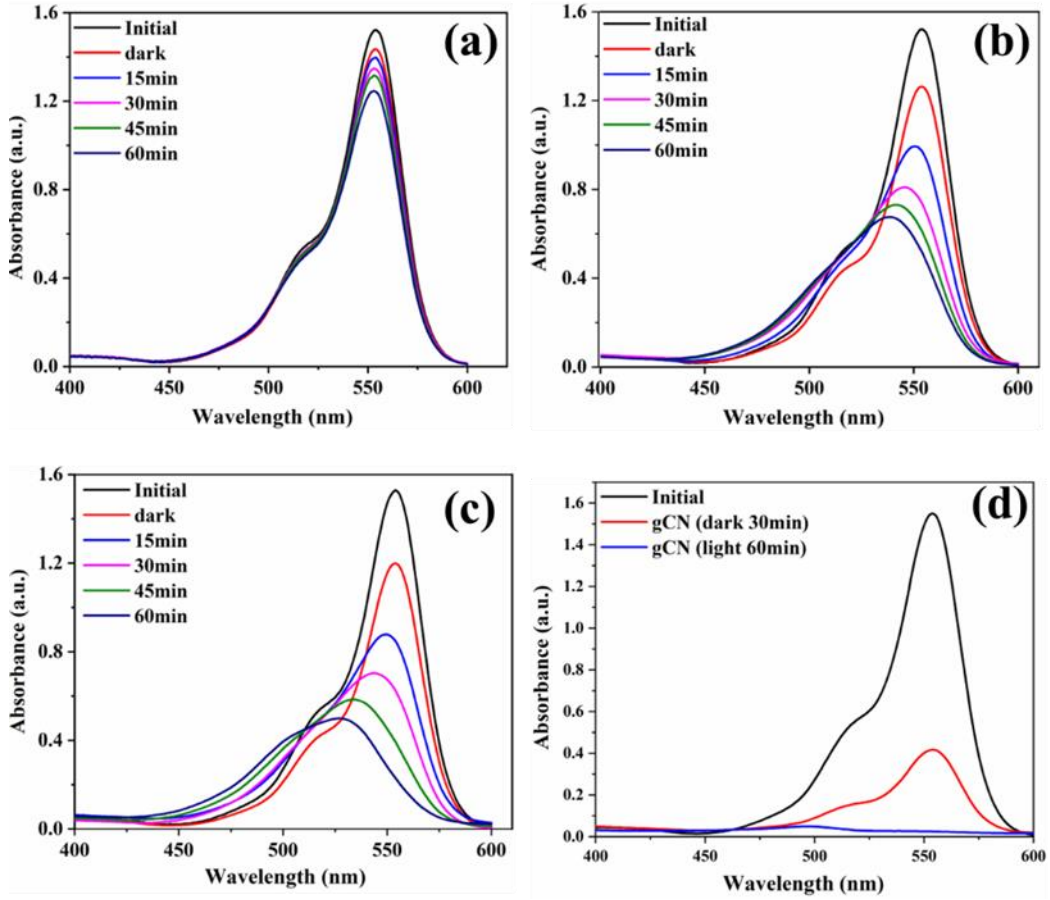

Fig. 2.13: Kinetics studies of BVO(a), BCN-1(b) and BCN-2(c) respectively and (d) showing only adsorption for g-C_3N_4.

2.3.8 Mechanistic Studies:

2.3.8.1 Mechanism

The proposed photocatalytic mechanism is based on the generation of electron-hole pairs by excitation through a band gap (**Fig. 2.14)**, a type-II heterojunction structure[36–39] in which the electrons (e^-) that are excited in CB of g-CN will transfer to the CB of BVO and corresponding holes (h^+) in VB of BVO will migrate to the VB of g-CN which reduces the electron-hole pair recombination. The hydroxyl radicals ($^{\cdot}OH$) and superoxide anions ($O_2^{\cdot-}$) are produced by redox interactions between the electrons and holes

and the water molecules and molecular oxygen, respectively. These reactive species photodegrade the RhB pollutant.

The band edge potential energies of BVO and g-C_3N_4 were calculated by the following equation to support the proposed mechanism [40]

$E_{VB} = X - E_e + 0.5E_g$

$E_{CB} = E_{VB} - E_g$

where, E_{VB}= Valence band potential

E_{CB}= Conduction band potential

X= Electronegativity of semiconductor (geometric mean of electronegativities of its constituent elements)

E_e= Energy of free electron

E_g= Band gap energy

The E_{VB} value for $BiVO_4$ and g-C_3N_4 is +2.85 eV and +1.64 eV respectively and E_{CB} is +0.48 eV for $BiVO_4$ and -1.29 eV for g-C_3N_4. There is a positive electrode potential of both the VB as well as CB for $BiVO_4$ as compared with the VB and CB of g-C_3N_4 [41].

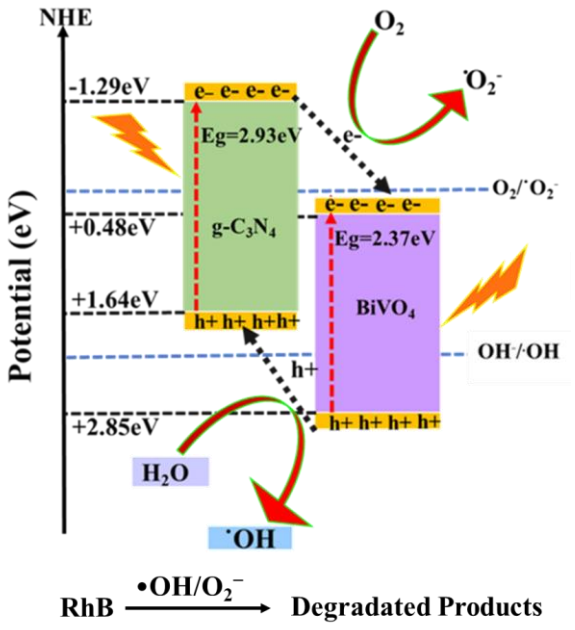

Fig. 2.14: A plausible mechanism for the photocatalytic degradation of RhB by using BCN-2 composite (10wt.% g-C_3N_4 @$BiVO_4$).

2.3.8.2 Scavengers Effect

To evaluate the role of reactive species, a number of control studies were conducted with EDTA, Argon gas purging, iPA, and NH_4SCN (**Fig. 2.15)**. It was observed that the degradation efficiency of the reaction mixture is decreased by the addition of EDTA, iPA, and NH_4SCN from 86% to 37%, 76%, and 62.2%, respectively. They function as hole scavengers which effectively prevent the production of hydroxyl radicals during the oxidation of water molecules by holes.

Additionally, the photocatalytic degradation efficiency drops to 71.5% after the purging of Ar gas. This is due to the elimination of oxygen from the reaction mixture caused by the argon purging, which lowers the feasibility of superoxide radical production. According to this result, photocatalytic oxidation activities are likely promoted by both superoxide anions and hydroxide radicals[42].

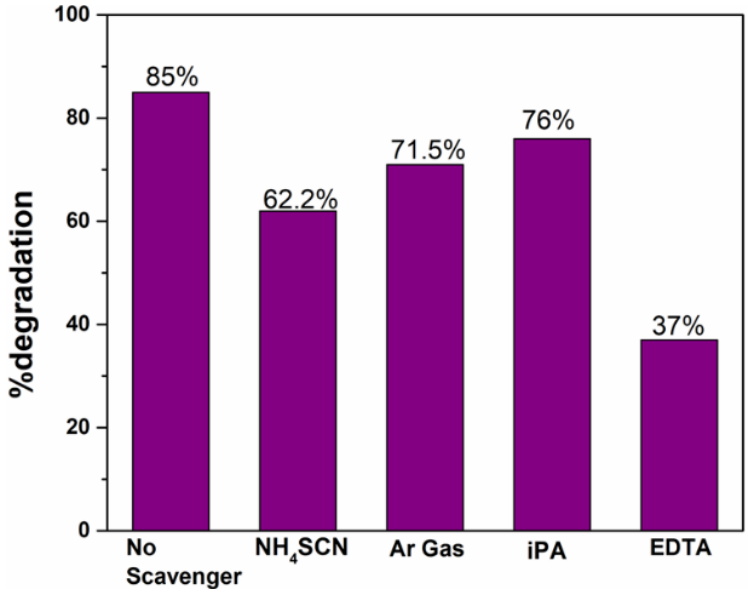

Fig. 2.15: Plot showing the variation of photocatalytic degradation of 10 wt.% g-CN@BVO (BCN-2 composite) after the purging of Ar and upon the addition of NH_4SCN, iPA and EDTA.

2.3.8.3 HRMS studies

In order to identify the intermediates, HPLC-MS studies were carried out **(Scheme 1)** and in **(Fig. 2.16)**. The signal at m/z 443 is characteristic of the parent RhB molecule. Apart from this the MS spectra also give prominent signals at m/z 415, 387, 359 and 331 corresponding to different de-ethylated intermediates[43,44]. Such observation suggests that the degradation process proceeds through de-ethylation pathway[44–46].

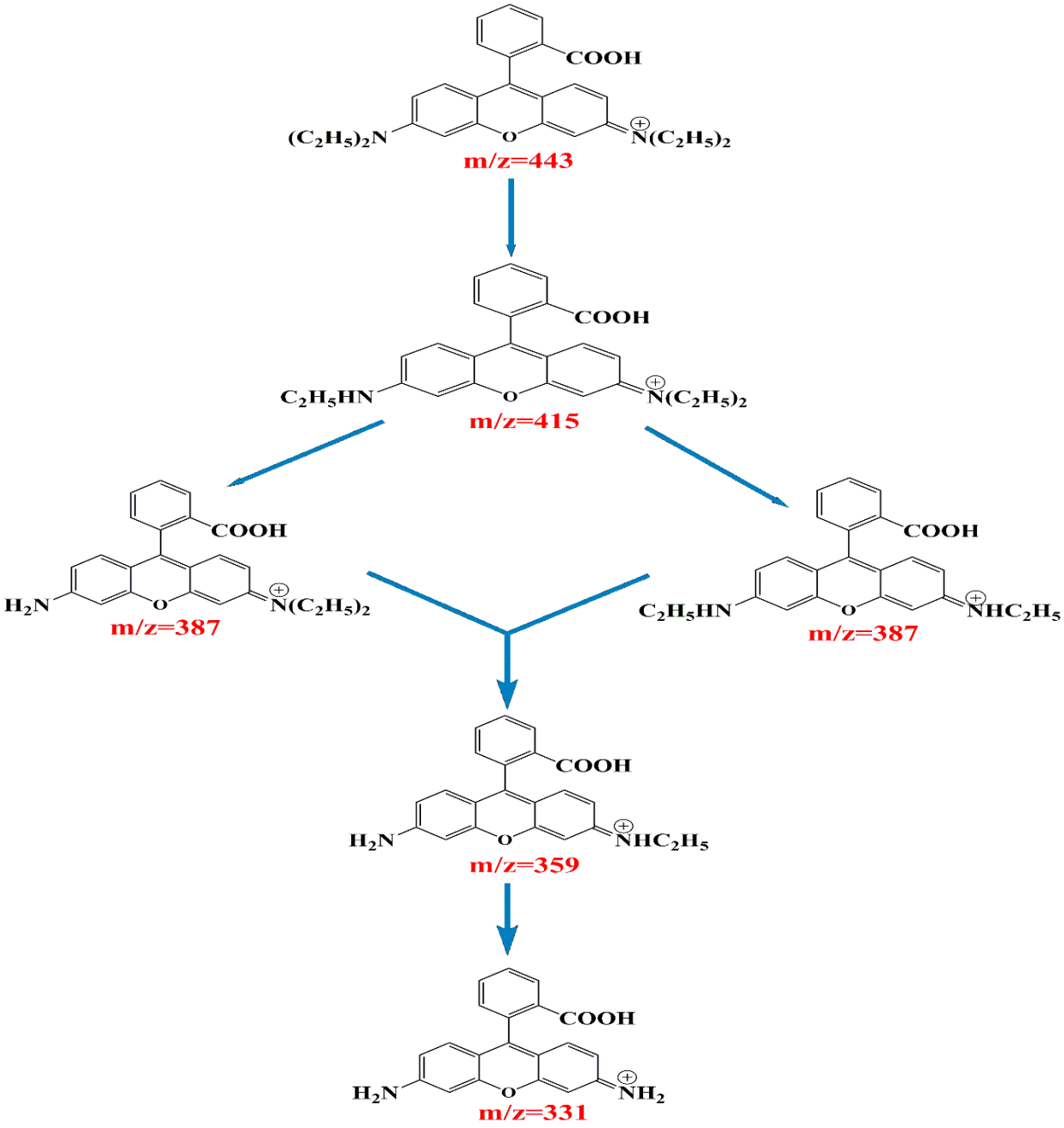

Scheme 1. A probable mechanism for the photodegradation of Rhodamine B dye using BCN-2 catalyst.

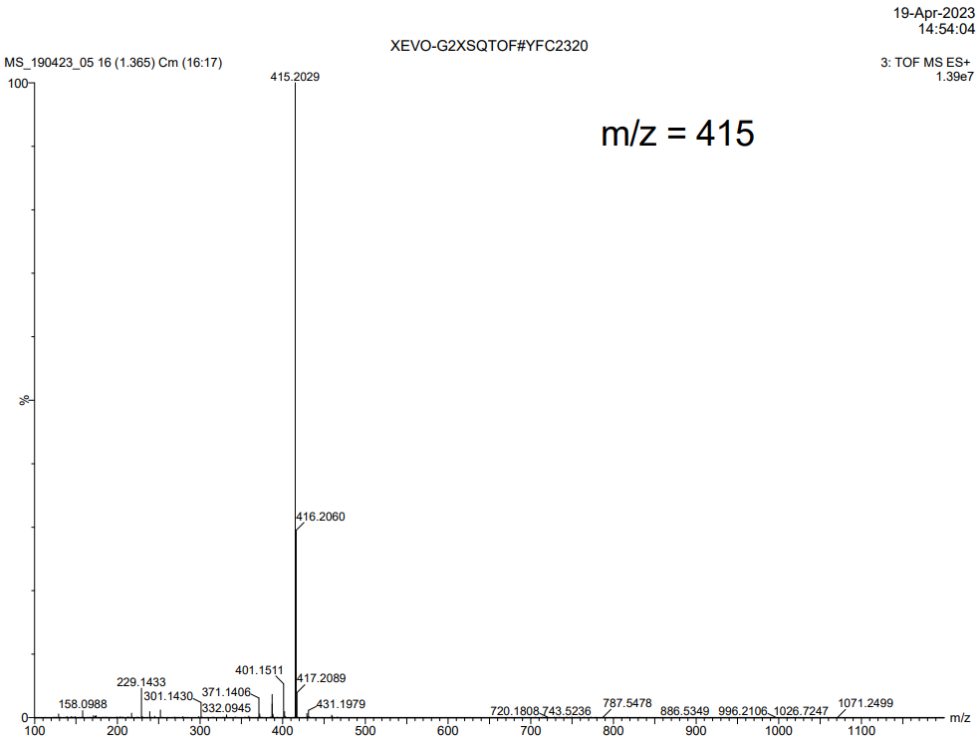
19-Apr-2023
14:54:04
XEVO-G2XSQTOF#YFC2320
MS_190423_05 16 (1.365) Cm (16:17)
3: TOF MS ES+
1.39e7
m/z = 415
415.2029
416.2060
401.1511
417.2089
229.1433
301.1430
371.1406
332.0945
158.0988
431.1979
720.1808,743.5236
787.5478
886.5349
996.2106,1026.7247
1071.2499
%
m/z

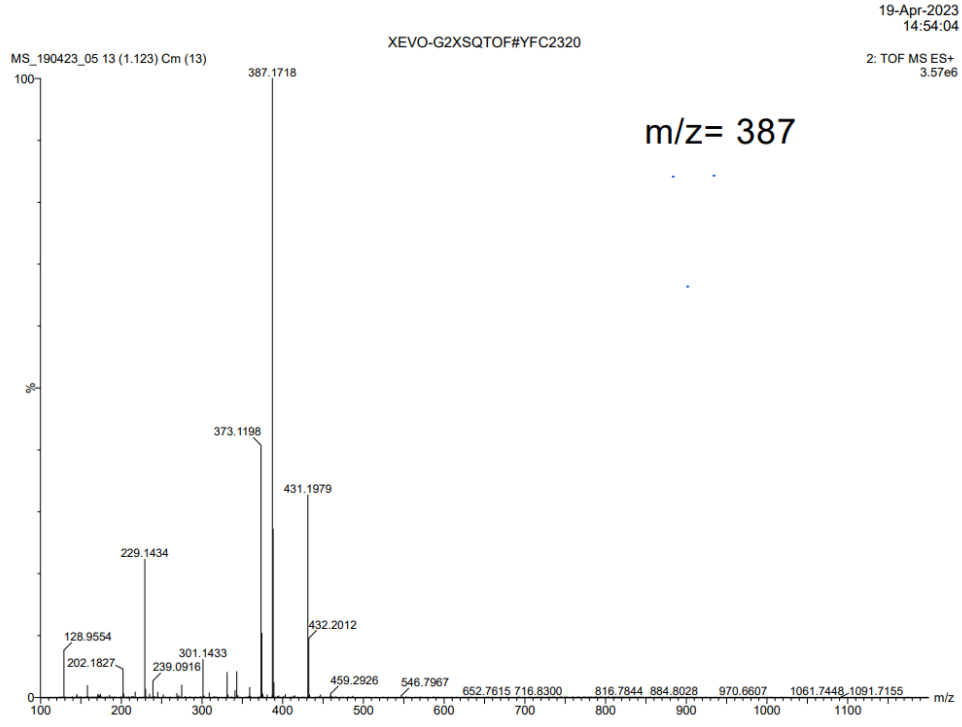
19-Apr-2023
14:54:04
XEVO-G2XSQTOF#YFC2320
MS_190423_05 13 (1.123) Cm (13)
2: TOF MS ES+
3.57e6
m/z= 387
387.1718
373.1198
431.1979
229.1434
432.2012
128.9554
202.1827
301.1433
239.0916
459.2926
546.7967
652.7615,716.8300
816.7844
884.8028
970.6607
1061.7448,1091.7155
%
m/z

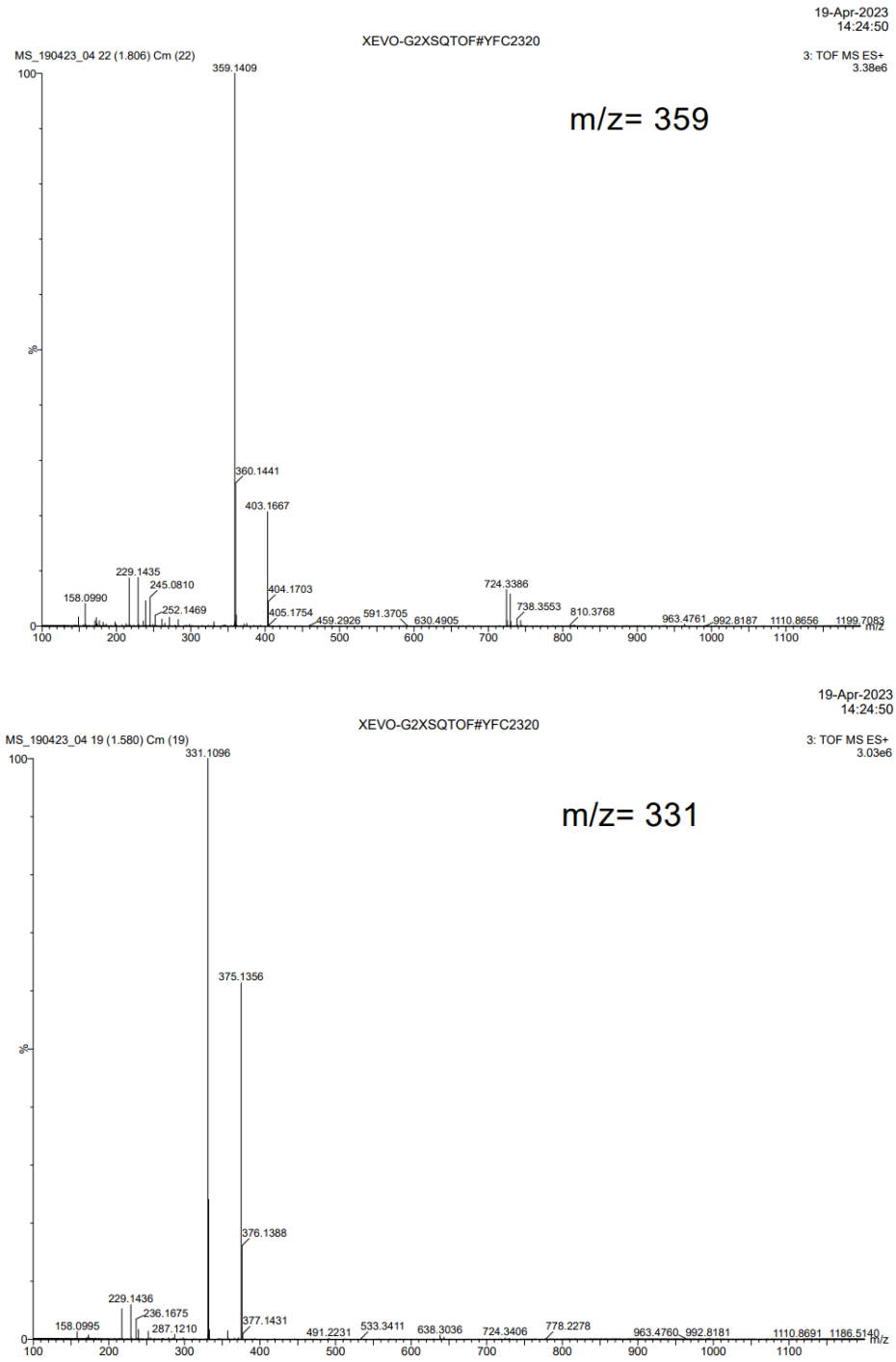

Fig. 2.16: HRMS pattern of the reaction mixture at different time intervals.

2.3.9 Recyclability of photocatalyst

In order to investigate the stability of the BCN-2 photocatalyst, recyclability studies were performed **(Fig. 2.17)**. The photocatalyst was recovered from the reaction mixture after the photodegradation process and reused in the following reaction under identical conditions. The recyclability of the photocatalyst is inspected with the help of 5 runs in the degradation of RhB. The degradation efficiencies were found to be 87%, 86%, 81%, 78% and 74% from the first to fifth cycle. Interestingly, there is only a 13% decrease in photocatalytic efficiency than the initial cycle, which can be due to the loss of amount during washing/ centrifugation and drying[47].

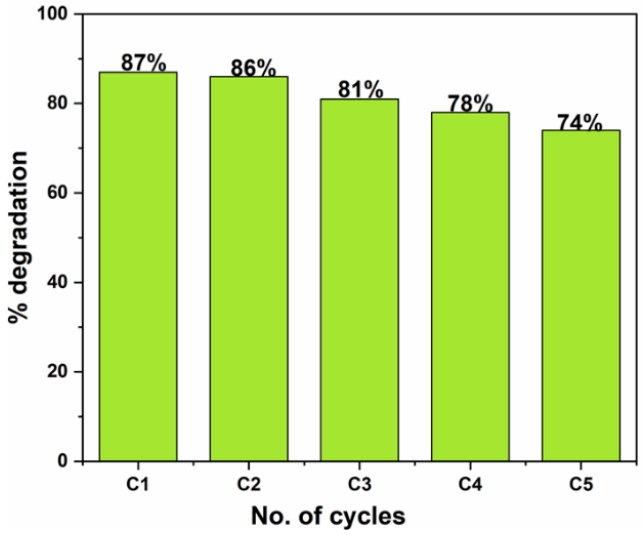

Fig. 2.17: Recyclability of the BCN-2 composite for the degradation of RhB using a visible light source for five successive runs.

2.3.10 Stability of Photocatalyst

In order to confirm the stability of the photocatalyst further, FTIR, XRD, and SEM of the BCN-2 composite before and after the reaction have been performed **(Fig. 2.18-2.19)**. It has been observed that the FTIR spectra **(Fig. 2.18)** and XRD patterns **(Fig. 2.19a)** remain practically similar before and after the photocatalytic reactions. The SEM images **(Fig. 2.19b)** reveal that the morphology of BCN-2 remains similar before and after the reactions. All these observations confirm the stability of the photocatalyst and rules out any possibility of dissociation or leaching during catalytic reactions.

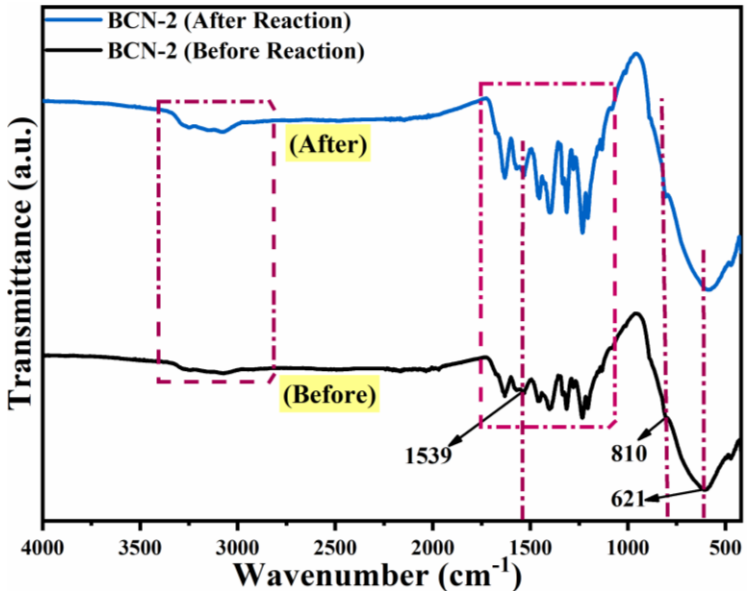

Fig. 2.18: FTIR spectra of BCN-2 composite before and after the photocatalytic reaction.

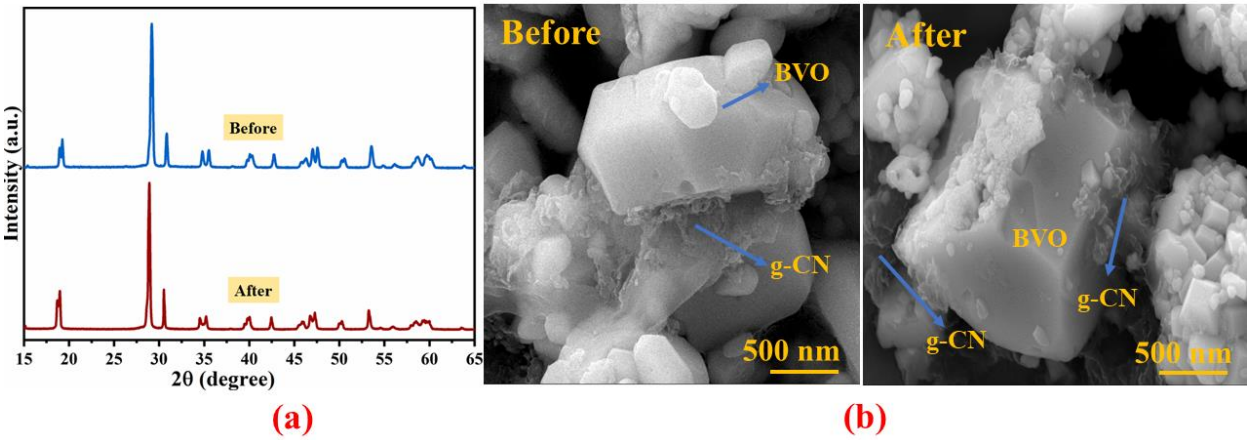

Fig. 2.19: (a) XRD patterns and (b) FESEM images of BCN-2 heterostructure before and after the photocatalytic reaction.

2.4 Conclusion:

In conclusion, this report involves the design of g-C_3N_4/$BiVO_4$ nanocomposites and the evaluation of their photocatalytic degradation activity towards the removal of RhB from wastewater under visible light radiation. The controlled experiments revealed that both hydroxide radicals and superoxide ions are the main reactive species in the photodegradation process. The HPLC-MS studies reveal that the photocatalytic reaction proceeds via de-ethylation mechanism. Moreover, the recyclability experiments confirmed the stability of the photocatalysts. Hence, the current report will be quite helpful in designing new-generation photocatalysts for wastewater treatment.

References:

1 A. Rafiq, M. Ikram, S. Ali, F. Niaz, M. Khan, Q. Khan and M. Maqbool, Photocatalytic degradation of dyes using semiconductor photocatalysts to clean industrial water pollution, *J. Ind. Eng. Chem.*, 2021, **97**, 111.

2 S. Chen, J. Zhang, C. Zhang, Q. Yue, Y. Li and C. Li, Equilibrium and kinetic studies of methyl orange and methyl violet adsorption on activated carbon derived from Phragmites australis, *Desalination*, 2010, **252**, 149.

3 C. Hu, A. T. Le, S. Y. Pung, L. Stevens, N. Neate, X. Hou, D. Grant and F. Xu, Efficient dye-removal via Ni-decorated graphene oxide-carbon nanotube nanocomposites, *Mater. Chem. Phys.*, 2021, **260**, 124117.

4 N. Daneshvar, D. Salari and A. R. Khataee, Photocatalytic degradation of azo dye acid red 14 in water: investigation of the effect of operational parameters, *J. Photochem. Photobiol. A. Chem.*, 2003, **157**, 111.

5 Z. Ajji and A. M. Ali, Adsorption of methyl violet and brilliant blue onto poly (vinyl alcohol) membranes grafted with N-vinyl imidazole/acrylic acid, *Nucl. Instrum. Methods Phys. Res. B.*, 2007, **265**, 362.

6 T. O. Ajiboye, O. A. Oyewo and D. C. Onwudiwe, Adsorption and photocatalytic removal of Rhodamine B from wastewater using carbon-based materials, *FlatChem*, 2021, **29**, 100277.

7 X. Lin, H. Li, L. Yu, H. Zhao, Y. Yan, C. Liu and H. Zhai, Efficient removal rhodamine B over hydrothermally synthesized fishbone like $BiVO_4$, *Mater. Res. Bull.*, 2013, **48**, 4424.

8 N. G. Deshpande, C. H. Ahn, R. R. Koli, A. S. Jamadar, D. S. Kim, Y. B. Kim and S. H. Jung, Controlled nanostructured morphology of $BiVO_4$ photoanodes for efficient on-demand catalysis in solar water-splitting and sustainable water-treatment, *Appl. Surf. Sci.*, 2020, **514**, 146075.

9 F. Chen, Q. Yang, X. Li, G. Zeng, D. Wang, C. Niu, J. Zhao, H. An, T. Xie and Y. Deng, Hierarchical assembly of graphene-bridged Ag_3PO_4/Ag/$BiVO_4$ (040) Z-scheme photocatalyst: An efficient, sustainable and heterogeneous catalyst with enhanced visible-light photoactivity towards tetracycline degradation under visible light irradiation, *Appl. Catal. B.*, 2017, **200**, 330.

10 Y. Wang, K. Ding, R. Xu, D. Yu, W. Wang, P. Gao and B. Liu, Fabrication of $BiVO_4$/$BiPO_4$/GO composite photocatalytic material for the visible light-driven degradation, *J. Clean Prod.*, 2020, **247**, 119108.

11 Y. Wang, D. Yu, W. Wang, P. Gao, L. Zhang, S. Zhong and B. Liu, The controllable synthesis of novel heterojunction CoO/$BiVO_4$ composite catalysts for enhancing visible-light photocatalytic property, *Colloids Surf. A. Physicochem. Eng. Asp.*, 2019, **578**, 123608.

12 H. Tian, M. Liu and W. Zheng, Constructing 2D graphitic carbon nitride nanosheets/layered MoS_2/graphene ternary nanojunction with enhanced photocatalytic activity, *Appl. Catal. B.*, 2018, **225**, 468.

13 W. Zhang, Y. Ma, X. Zhu, S. Liu, T. An, J. Bao, X. Hu and H. Tian, Fabrication of Ag decorated g-C_3N_4/$LaFeO_3$ Z-scheme heterojunction as highly efficient visible-light photocatalyst for degradation of methylene blue and tetracycline hydrochloride, *J. Alloys Compd.*, 2021, **864**, 158914.

14 J. Bao, X. Jiang, L. Huang, W. Quan, C. Zhang, Y. Wang, H. Wang, Y. Zeng, W. Zhang, Y. Ma, S. Yu, X. Hu and H. Tian, Molybdenum disulfide loading on a Z-scheme graphitic carbon nitride and lanthanum nickelate heterojunction for enhanced photocatalysis: Interfacial charge transfer and mechanistic insights, *J. Colloid Interface Sci.*, 2022, **611**, 684.

15 N. Fajrina and M. Tahir, Monolithic Ag-Mt dispersed Z-scheme pCN-TiO_2 heterojunction for dynamic photocatalytic H_2 evolution using liquid and gas phase photoreactors, *Int. J. Hydrogen Energy*, 2020, **45**, 4355.

16 S. S. Lam, V. H. Nguyen, M. T. Nguyen Dinh, D. Q. Khieu, D. D. La, H. T. Nguyen, D. V. N. Vo, C. Xia, R. S. Varma, M. Shokouhimehr, C. C. Nguyen, Q. Van Le and W. Peng, Mainstream avenues for boosting graphitic carbon nitride efficiency: towards enhanced solar light-driven photocatalytic hydrogen production and environmental remediation, *J. Mater. Chem. A*, 2020, **8**, 10571.

17 X. Guo, J. Duan, W. Wang and Z. Zhang, Modified graphitic carbon nitride as the photocatalyst for wastewater treatment under visible light irradiation, *Fuel*, 2020, **280**, 118544.

18 J. Zhao, J. Yan, H. Jia, S. Zhong, X. Zhang and L. Xu, $BiVO_4$/g-C_3N_4 composite visible-light photocatalyst for effective elimination of aqueous organic pollutants, *J. Mol. Catal. A Chem.*, 2016, **424**, 162.

19 D. Monga, D. Ilager, N. P. Shetti, S. Basu and T. M. Aminabhavi, 2D/2d heterojunction of MoS_2/g-C_3N_4 nanoflowers for enhanced visible-light-driven photocatalytic and electrochemical degradation of organic pollutants, *J. Environ. Manage.*, 2020, **274**, 111208.

20 J. Singh, P. Kumari and S. Basu, Degradation of toxic industrial dyes using SnO_2/g-C_3N_4 nanocomposites: Role of mass ratio on photocatalytic activity, *J. Photochem. Photobiol. A Chem.*, 2019, **371**, 136.

21 P. Kumari, B. Pal and R. K. Das, Superior adsorptive removal of eco-toxic drug diclofenac sodium by Zn–Al LDH·xBi_2O_3 layer double hydroxide composites, *Appl. Clay Sci.*, 2021, **208**, 106119.

22 M. I. Chebanenko, N. V Zakharova, A. A. Lobinsky and V. I. Popkov, Ultrasonic-Assisted Exfoliation of Graphitic Carbon Nitride and its Electrocatalytic Performance in Process of Ethanol Reforming, *Semicond.*, 2019, **53**, 2072.

23 S. Dong, G. J. Lee, R. Zhou and J. J. Wu, Synthesis of g-C_3N_4/$BiVO_4$ heterojunction composites for photocatalytic degradation of nonylphenol ethoxylate, *Sep. Purif. Technol.*, 2020, **250**, 117202.

24 M. Zhang, Facile fabrication of $BiVO_4$/g-C_3N_4 photocatalysts and its photocatalytic activity under visible light irradiation, *J. Mater. Sci.: Mater. Electron.*, 2020, **31**, 1335.

25 M. Han and J. Jia, The interlace of Bi_2S_3 nanowires with TiO2 nanorods: An effective strategy for high photoelectrochemical performance, *J. Colloid Interface Sci.*, 2016, **481**, 91.

26 M. Han, H. Guo, B. Li, J. Jia and W. Wang, Controllable coverage of Bi_2S_3 quantum dots on one-dimensional TiO_2 nanorod arrays by pulsed laser deposition technique for high photoelectrochemical properties, *New J. Chem.*, 2017, **41**, 4820.

27 X. Lin, C. Liu, J. Wang, S. Yang, J. Shi and Y. Hong, Graphitic carbon nitride quantum dots and nitrogen-doped carbon quantum dots co-decorated with $BiVO_4$ microspheres: A ternary heterostructure photocatalyst for water purification, *Sep. Purif. Technol.*, 2019, **226**, 117.

28 S. S. Kekade, P. V. Gaikwad, S. A. Raut, R. J. Choudhary, V. L. Mathe, D. Phase, A. Kshirsagar and S. I. Patil, Electronic Structure of Visible Light-Driven Photocatalyst δ-$Bi_{11}VO_{19}$ Nanoparticles Synthesized by Thermal Plasma, *ACS Omega*, 2018, **3**, 5853.

29 X. Zhang, Q. Wu, Z. Du, Y. Zheng and Q. Li, Green synthesis of g-C_3N_4-Pt catalyst and application to photocatalytic hydrogen evolution from water splitting, *Fuller. Nanotub. Car. N.*, 2018, **26**, 688.

30 N. A. Mohamed, J. Safaei, A. F. Ismail, M. F. Mohamad Noh, N. A. Arzaee, N. N. Mansor, M. A. Ibrahim, N. A. Ludin, J. S. Sagu and M. A. Mat Teridi, Fabrication of exfoliated graphitic carbon nitride, (g-C_3N_4) thin film by methanolic dispersion, *J. Alloys Compd.*, 2020, **818**, 152916.

31 Y. P. Zhu, T. Z. Ren and Z. Y. Yuan, Mesoporous Phosphorus-Doped g-C_3N_4 Nanostructured Flowers with Superior Photocatalytic Hydrogen Evolution Performance, *ACS Appl. Mater. Interfaces*, 2015, **7**, 16850.

32 W. Ali, H. Ullah, A. Zada, W. Muhammad, S. Ali, S. Shaheen, M. K. Alamgir, M. Z. Ansar, Z. U. Khan, H. Bilal and P. S. Yap, Synthesis of TiO_2 modified self-assembled honeycomb ZnO/SnO_2 nanocomposites for exceptional photocatalytic degradation of 2,4-dichlorophenol and bisphenol A, *Sci. Total Environ.*, 2020, **746**, 141291.

33 A. Kundu, S. Sharma and S. Basu, Modulated BiOCl nanoplates with porous g-C_3N_4 nanosheets for photocatalytic degradation of color/colorless pollutants in natural sunlight, *J. Phys. Chem. Solids*, 2021, **154**, 110064.

34 L. Li, M. Mao, X. She, J. Yi, M. He, L. Pan, Z. Chen, H. Xu and H. Li, Direct Z-scheme photocatalyst for efficient water pollutant degradation: A case study of 2D g-C_3N_4/$BiVO_4$, *Mater. Chem. Phys.*, 2020, **241**, 122308.

35 A. Nagar and S. Basu, Ternary g-C_3N_4/Ag/$BiVO_4$ nanocomposite: Fabrication and implementation to remove organic pollutants, 2021, **23**, 101646.

36 T. Jiang, F. Nan, J. Zhou, F. Zheng, Y. Weng, T. Y. Cai, S. Ju, B. Xu and L. Fang, Enhanced photocatalytic and photoelectrochemical performance of g-C_3N_4/$BiVO_4$ heterojunction: A combined experimental and theoretical study, *AIP Adv.*, 2019, **9**, 055225.

37 N. Tian, H. Huang, Y. He, Y. Guo, T. Zhang and Y. Zhang, Mediator-free direct Z-scheme photocatalytic system: $BiVO_4$/g-C_3N_4 organic–inorganic hybrid photocatalyst with highly efficient visible-light-induced photocatalytic activity, *Dalton Trans.*, 2015, **44**, 4297.

38 Y. Ji, J. Cao, L. Jiang, Y. Zhang and Z. Yi, G–C_3N_4/$BiVO_4$ composites with enhanced and stable visible light photocatalytic activity, *J. Alloys Compd.*, 2014, **590**, 9.

39 K. Zhong, J. Feng, H. Gao, Y. Zhang and K. Lai, Fabrication of $BiVO_4$@g-C_3N_4(100) heterojunction with enhanced photocatalytic visible-light-driven activity, *J. Solid State Chem.*, 2019, **274**, 142.

40 N. Tian, H. Huang, Y. He, Y. Guo, T. Zhang and Y. Zhang, Mediator-free direct Z-scheme photocatalytic system: $BiVO_4$/g-C_3N_4 organic–inorganic hybrid photocatalyst with highly efficient visible-light-induced photocatalytic activity, *Dalton Trans.*, 2015, **44**, 4297.

41 Y. Ji, J. Cao, L. Jiang, Y. Zhang and Z. Yi, G–C_3N_4/$BiVO_4$ composites with enhanced and stable visible light photocatalytic activity, *J. Alloys Compd.*, 2014, **590**, 9.

42 M. Chahkandi and M. Zargazi, New water based EPD thin BiVO4 film: Effective photocatalytic degradation of Amoxicillin antibiotic, *J. Hazard. Mater.*, 2020, **389**, 121850.

43 K. Yu, S. Yang, H. He, C. Sun, C. Gu and Y. Ju, Visible Light-Driven Photocatalytic Degradation of Rhodamine B over $NaBiO_3$: Pathways and Mechanism, *J. Phys. Chem. A.*, 2009, **113**, 10024.

44 G. Sharma, D. D. Dionysiou, S. Sharma, A. Kumar, A. H. Al-Muhtaseb, M. Naushad and F. J. Stadler, Highly efficient Sr/Ce/activated carbon bimetallic nanocomposite for photoinduced degradation of rhodamine B, *Catal. Today*, 2019, **335**, 437.

45 T. S. Natarajan, M. Thomas, K. Natarajan, H. C. Bajaj and R. J. Tayade, Study on UV-LED/TiO_2 process for degradation of Rhodamine B dye, *Chem. Eng. J.*, 2011, **169**, 126.

46 Z. HE, S. YANG, Y. JU and C. SUN, Microwave photocatalytic degradation of Rhodamine B using TiO_2 supported on activated carbon: Mechanism implication, *J. Environ. Sci.*, 2009, **21**, 268.

47 H. Kaur, S. Singh and B. Pal, Effect of plasmonic metal (Cu, Ag, and Au) loading over the physicochemical and photocatalytic properties of Mg-Al LDH towards degradation of tetracycline under LED light, *Appl. Surf. Sci.*, 2023, **609**, 155455.

CHAPTER-3

CHAPTER-3

Photocatalytic degradation of Reactive orange 16 under visible light using ternary nanocomposite Bi-doped g-C_3N_4/Bi_2WO_6.

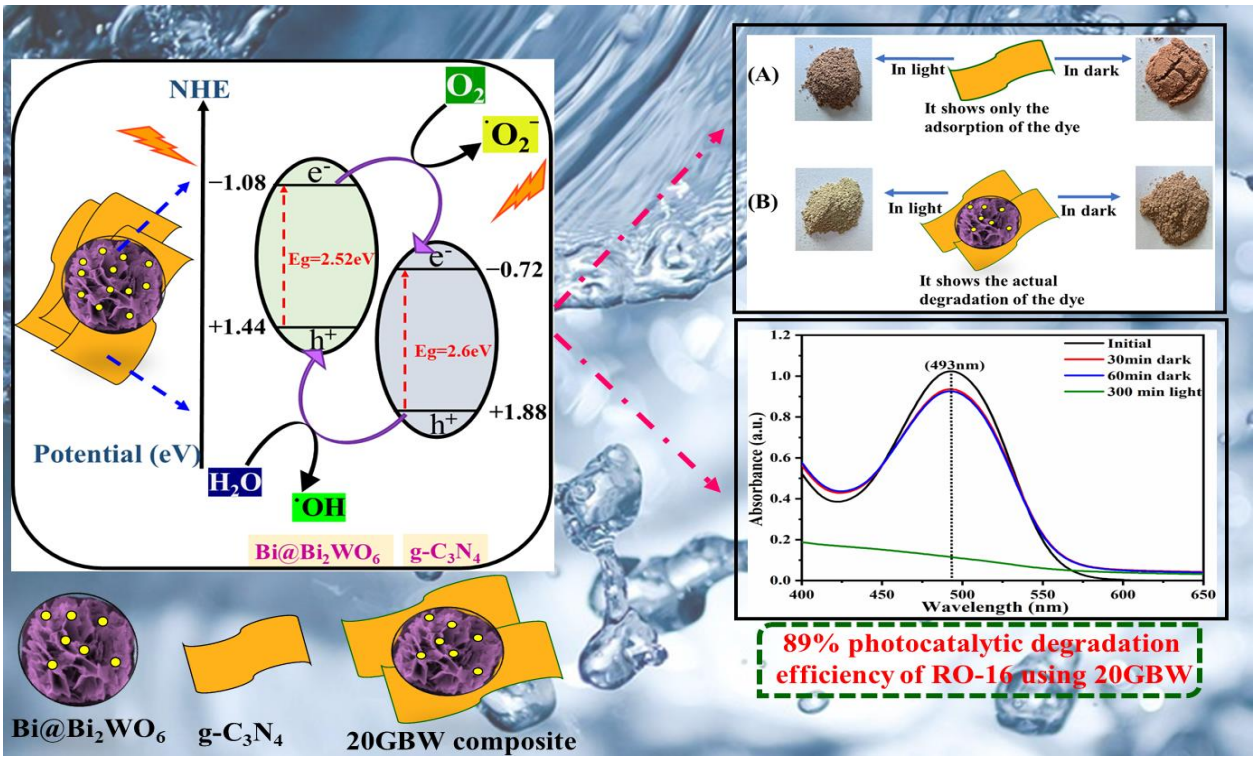

Schematic outline:

The Bi-doped g-C_3N_4@Bi_2WO_6 were prepared by wet impregnation followed by calcination method. The photocatalyst is highly stable and having suitable band gap of 2.22 eV lying in visible region. Bi (0) doping occurs concertedly without addition of any extra reducing agent during in-situ hydrothermal synthesis of Bi_2WO_6, which was confirmed by XPS and HRTEM along with the presence of SPR band in DRS. The effect of non-noble metal present here is that it increases the visible light response through LSPR effect. Loading of g-C_3N_4 enhances the surface area which decreases the charge transfer resistance, which further helped in degradation of pollutant.

3.1 Introduction:

In recent years, excessive use of organic dyes by the textile industries has emerged as one of the most important threats to the ecosystem [1]. Reactive dyes are one of the foremost widely used colorants in the textile industry. These dyes react with cotton fabric to form covalent bonds, thereby resulting in quite a strong affinity towards the fabric. As a result, they possess exceptionally high wet fastness [2]. Unfortunately, textile effluents contain a significant concentration of unfixed dyes that are disposed of directly into the environment. These dyes have a harsh impact on the environment as they are carcinogenic, mutagenic, and highly toxic [3–6]. Moreover, they also significantly affect the aquatic ecosystem, human beings, and crop productivity [7–9]. The elimination of these dye effluents is tricky due to their structural complexity, high stability, and poor biodegradability. Consequently, their efficient elimination from wastewater becomes extremely important. To date, several techniques, such as ion exchange, coagulation, nano-filtration, adsorption, photocatalysis, etc., have been developed[10] one of the most promising methodologies in wastewater treatment as it results in the total decomposition of the pollutants instead of transmitting them from one medium to another[11,12].

Nowadays, semiconductor-based photocatalysts have attracted a significant amount of interest in the area of wastewater treatment [13–15]. Bi_2WO_6 is a member of the Aurivillius class of perovskite oxide. Its structure consists of alternate layers of anionic $(WO_4)_2^-$ and cationic $(Bi_2O_2)^{2+}$ sheets. It has drawn much attention because of its exceptional electronic properties, stability, reactivity, low toxicity, etc [16–18]. However, the principal drawback of pure Bi_2WO_6 is interrelated with its low absorbance in the visible region, high charge transfer resistance, fast electron-hole pair recombination, photo-corrosion, low surface area, etc. These shortcomings can be resolved using a variety of strategies. Common techniques for modifying this semiconductor photocatalyst's band structure include element doping [19–21] and heterojunction construction[22–24]. One of the most capable materials for producing a semiconductor heterojunction is g-C_3N_4 because of its low cost and high stability. In addition, g-C_3N_4 has additional benefits like a unique energy band of about 2.7 eV, a large surface area, strong physicochemical stability, and non-toxicity [25–27].

Moreover, the loading of various plasmonic elements can also increase photocatalytic activities [28–30]. These elements boost the light absorption characteristics through the localized surface plasmon resonance (LSPR) phenomenon to afford high-energy charge carriers that disperse through vibrational modes to yield large lattice temperatures. Hence these materials act as superior photocatalysts. Apart from the precious metal, non-novel elements like Bi exhibit substantial LSPR effects [19,31–34]. Also, the lower cost of bismuth compared to the novel metals offers an additional advantage. The present study involves the preparation of a Bi-doped g-C_3N_4/Bi_2WO_6 ternary composite and evaluating its visible-

light-driven photodegradation efficiency for the removal of reactive orange 16 (RO-16) dye. The Bi-doped Bi_2WO_6 (Bi@Bi_2WO_6) was prepared by the solvothermal technique in the presence of cetyltrimethylammonium bromide (CTAB). Interestingly, the reduction of Bi (III) does not need any extra step or the addition of any additional reducing agent. Herein, the CTAB plays a dual role. It acts as a surfactant to prevent the agglomeration of Bi_2WO_6 nanoparticles and as a mild reducing agent[35] to afford the formation of Bi metal through the in-situ reduction of Bi (III). The g-C_3N_4 loading was successfully achieved via the wet impregnation method followed by calcination. This composite can possess high photocatalytic efficiency due to complementary characteristics of metallic Bi, Bi_2WO_6, and g-C_3N_4.

3.2 Experimental:

3.2.1 Chemicals:

All the substances: Bismuth (III) nitrate pentahydrate 98% [Bi $(NO_3)_3$. $5H_2O$], Urea 99% extra pure, Sodium tungstate dihydrate 98% extra pure [Na_2WO_4. $2H_2O$], Cetyltrimethyl ammonium bromide (CTAB) 99% AR [$C_{19}H_{42}BrN$] was obtained from Loba Chemie, India. Absolute ethanol (99%) was bought from Changshu Hongsheng Fine Chemicals Co. Ltd. Reactive orange 16 (Remazol bright orange 3R) was obtained from SRL India, and deionized water (DI) was manufactured using the Milli-Q, Millipore ultrafiltration system. N-methyl-2-pyrrolidone (NMP) was bought from India's Loba Chemie. The fluorinated tin oxide (FTO) coated glasses (resistance<10Ω), polyvinylidene fluoride (PVDF), and carbon black (CB) powder were purchased from Vritra Technologies, Sigma Aldrich, and Nanoshell.

3.2.2 Preparation of Bi@Bi_2WO_6:

The hydrothermal method was used to synthesize Bi@Bi_2WO_6, 0.1 g of CTAB, and 1.2125 g of [Bi $(NO_3)_3$. $5H_2O$] were mixed with 50 mL of DI water and stirred the mixture until a clear solution formed. Then 0.4125 g of $Na_2WO_4 \cdot 2H_2O$ was added to this reaction mixture followed by vigorous stirring for 30 minutes. The reaction mixture was then placed in an autoclave for 12 h at 170 ℃. After being washed with DI water, and ethanol the milky white precipitate was dried at 60 ℃ [25]. This will be represented as BW throughout this manuscript.

3.2.3 Preparation of g-C_3N_4:

50 mL of DI water and 12 g of urea were mixed in a mortar pestle and then heated for 12 h at 60 °C to facilitate recrystallization. After recrystallizing, it was covered in aluminium foil and heated for 2 h at 550 °C at a rate of 10 °C per min. The obtained brownish-coloured g-C_3N_4 was ground into a powdered form [36] and will be designated as g-CN throughout the manuscript.

3.2.4 Preparation of g-CN loaded BW composite:

The wet impregnation followed by the calcination method was used to prepare the composite [37,38]. To prepare the g-C_3N_4/Bi@Bi_2WO_6 composite, 100 mg of Bi_2WO_6 and the requisite quantity of g-CN were first mixed in DI water (50 mL), and then the mixture was sonicated for 1h. Afterwards, the solution was left for 24 h on stirring. Then, the solid products were separated from the reaction mixture using centrifugation, which was dehydrated at 70 °C. The product was then calcined for 1 h at 300 °C at a rate of 5 °C per min in a muffle furnace. The 5, 10, and 20wt% g-C_3N_4 loaded Bi@Bi_2WO_6 binary composites will be abbreviated 5GBW, 10GBW, and 20GBW respectively, throughout this manuscript.

3.2.5 Preparation of thin films:

The working electrodes for the Electrochemical impedance spectroscopy (EIS) Nyquist plot were fabricated by using the drop-casting method. NMP (40-60 µL) and PVDF (1mg) were mixed to achieve a smooth paste. CB (1 mg) was added and blended for another 20 min. Then the 8 mg of the material of interest (BW or 20GBW) was added and melded to obtain a uniform paste. It was then drop-casted onto a fresh FTO-coated glass film and then desolvated for 12 h at 80 °C.

3.2.6 Photocatalytic activity evaluation:

Reactive orange 16 is selected as a model contaminant to examine the photocatalytic characteristics of as-prepared BW and the composites (5GBW, 10 GBW, and 20 GBW). In an exemplary experiment, 7.5mg of the composite was added to a test tube along with 5 mL of Reactive Orange 16 solution (40 ppm). The suspension was stirred for 30 minutes in the dark to attain the adsorption-desorption equilibrium. Thereafter, visible light exposure (Wipro Garnet B22-50 W LED bulb with $\lambda > 360$ nm) was directed onto the reaction mixture for different predetermined intervals. After the photocatalysts were extracted by centrifugation, the concentration of the dye-reactive orange 16 in the corresponding solution was monitored using UV-Vis spectroscopy. The degradation efficiency(%D) was obtained by the equation 1:

$$Degradation\ efficiency\ (\%\boldsymbol{D}) = \frac{\boldsymbol{C_0 - C_t}}{\boldsymbol{C_0}} \times 100 \qquad (1)$$

The initial and final concentrations of the pollutants are denoted by $\mathbf{C_0}$ and $\mathbf{C_t}$

All photodegradation reactions were done in three batches and the mean and standard deviation of the degradation efficiencies were calculated.

The demineralization efficiency was calculated using the equation 2.

$$Demineralization\ efficiency\ = \frac{T_0 - T_t}{T_0} \times 100 \qquad (2)$$

Where T_0 and T_t are the initial and final total organic carbon (TOC) content of the reaction mixture.

3.2.7 Characterization technique:

X-ray diffraction (XRD) was done by utilizing an Xpert pro-Cu-Kα (1.54 Å) diffractometer at 45 kV with a diffraction angle (2θ) o10-65° to record the crystallographic properties. Field-emission scanning electron microscopy (FESEM, Carl-Zeiss Sigma 500 FEG-SEM) and high-resolution transmission electron microscopy (HRTEM, JEOL JEM 2100 plus) were used to examine the structural morphology. The diffused reflectance spectroscopic (DRS) measurements of the as-prepared catalyst were studied using JASCO V-750 Spectrophotometer. X-ray photoelectron spectroscopy (XPS) was employed to validate the oxidation state, and XPS valence band spectra were studied using (XPS, Thermo Fischer Scientific ESCALAB Xi). A Microtrac Belsorp Mini-II (Bel, Japan, Inc.) surface area analyzer was used to determine the external surface area. IRTracer-100 (Shimadzu) was used to record the Fourier Transform Infrared (FTIR) Spectra. High-resolution mass spectrometry (HRMS) studies were performed by using Waters mass spectrometer (QTOF) with UPLC (XEVO G2 XS) and Ion source Combined APCI and ESI source (including positive as well negative mode scans) to identify the intermediates. Experiments of Electrochemical impedance spectroscopy (EIS) was conducted using a Biologic VSP300 potentiostat, at 0.4 V versus RHE, in the frequency range 1-1000 Hz under dark conditions in a three-electrode system comprised of Pt, BW/20GBW loaded FTO, and standard Calomel electrode as the counter, working, and reference electrodes respectively in Na_2SO_4 solution (0.1 M). Total organic carbon (TOC) measurements were conducted using the Analytikjena TOC/TNb analyzer (series 300).

3.3 Result and discussion:

3.3.1 XRD Studies

The phase purity and crystallinity of the synthesized materials were studied using XRD **(Fig. 3.1)**. XRD pattern of g-CN (Fig. 1a) shows that the (002) plane has a strong intensity peak at 27.5°, while the (100) plane has another peak at 12.7°. Furthermore, there are two extra peaks between 15° and 25°, which can result from the layered structure of g-CN, which matches quite well with the ICDD No. 87-1526. The slight shift (002) peak position can be attributed to the charge in the inter-planar distance between the g-CN layers [36,39,40]. The peaks at 28.3°, 32.8°, 47.1°, 55.8°, and 58.5° belong to (133), (020), (220), (313), and (262) planes, which match quite well with the ICDD No. 39-0256 of Bi_2WO_6 (orthorhombic crystallographic phase) [25,37] **(Fig. 3.1b-c)**. Furthermore, the XRD patterns of the 5GBW,

10GBW, and 20GBW hetero-composites are practically identical with the original BW, suggesting that the loading of g-CN does not considerably affect the structural integrity of the BW [36,38,41]. The absence of any g-CN signal in the composite is because of the low loading and relatively smaller X-ray scattering coefficient of g-CN compared to BW.

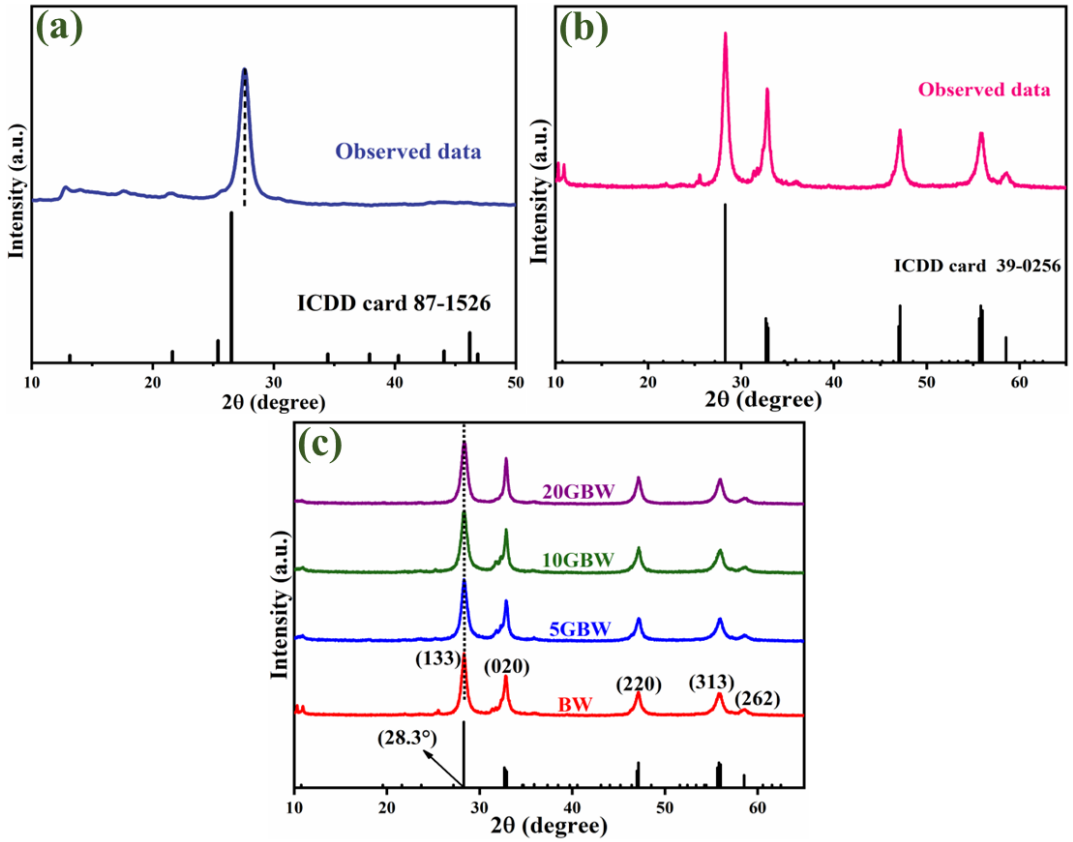

Fig. 3.1: XRD patterns of (a) g-CN, (b) BW, (c) bare BW, and all the g-CN loaded composites (5GBW, 10GBW and 20GBW).

3.3.2 XPS Studies

XPS studies have been used to find out the surface chemical composition of the 20GBW composite **(Fig. 3.2)**. The Bi 4f signals at 159.2 eV (Bi $4f_{7/2}$) and 164.5 eV (Bi $4f_{5/2}$) are characteristic of trivalent bismuth in Bi_2WO_6 **(Fig. 3.2b)**. Remarkably, the additional signals at 157.2 eV (Bi $4f_{7/2}$) and 162.5 eV (Bi $4f_{5/2}$) **(Fig. 3.2b)** confirm the reduction of Bi^{+3} to zerovalent Bi by CTAB [41–43]. The W $4f_{5/2}$ and $4f_{7/2}$ signals at 37.5 eV and 35.3 eV **(Fig. 3.2c)** affirm its hexavalent oxidation state (W^{+6}) [44]. The Bi–O linkages correspond to O1s peaks at 530.3 eV and 530.6 eV **(Fig. 3.2d)** [41,43]. Four peaks could be identified in the XPS spectra of C1s as binding energies at 284.6 eV, 287.2 eV, 293.6 eV, and 280.7 eV **(Fig. 3.2e)** are because of extraneous carbon in the surface, sp^2 hybridized carbon of (N)2–C=N heterocyclic ring, the residual C=O in the surface and indefinable hydrocarbon respectively [45–48]. The

peaks detected at 398.6 eV and 400.4 eV correspond to the imino and amino groups, respectively **(Fig. 3.2f)** [49,50].

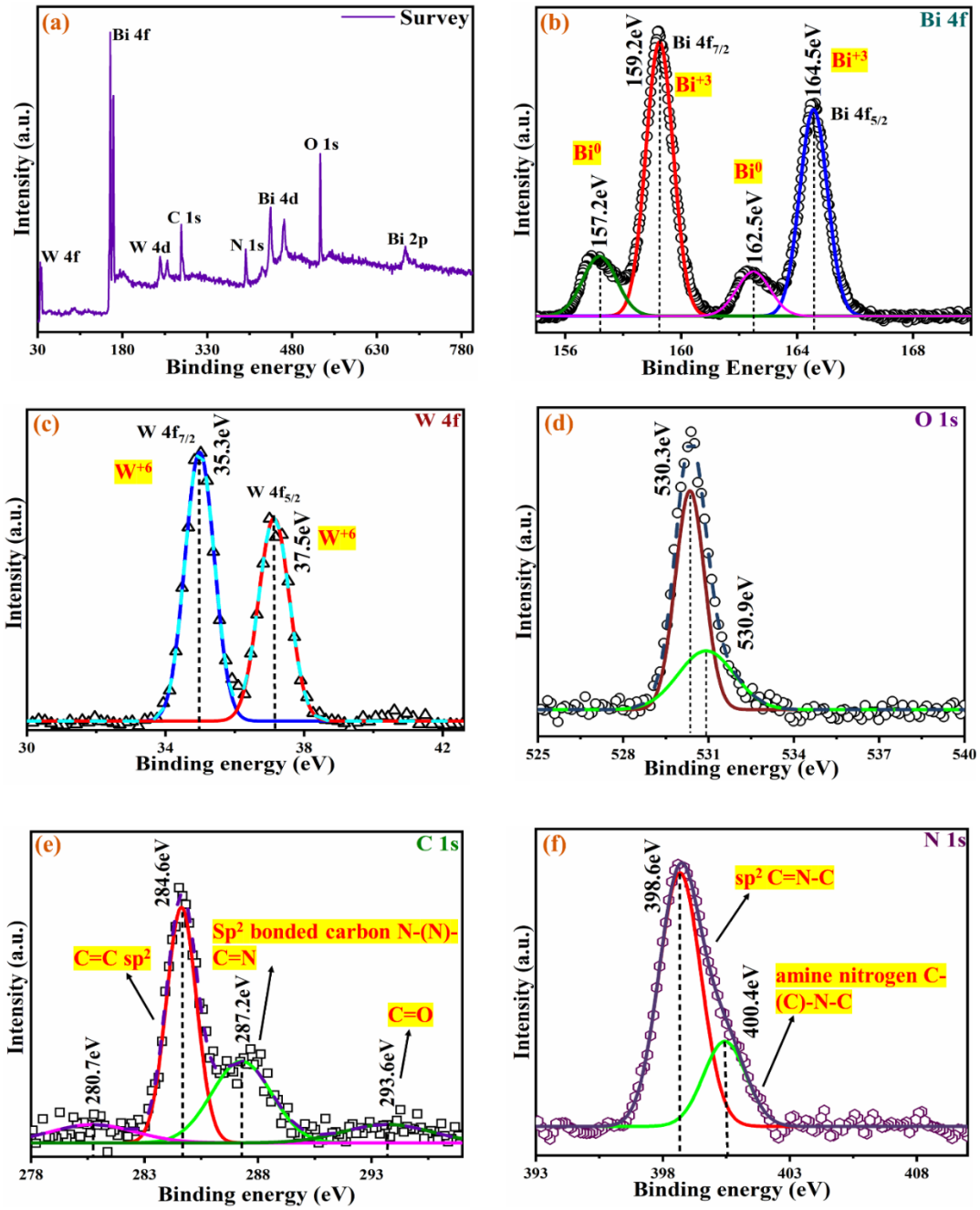

Fig. 3.2: XPS spectra shows (a) Survey spectrum (b) Bi 4f (c) W 4f (d) O 1s (e) C 1s (f) N 1s of the 20GBW composite.

3.3.3 Optical Properties

The optical properties were investigated to calculate the optical bandgap of the BW and the composites. The absorption edges at 447 nm and 438 nm are characteristic of the Bi_2WO_6 and g-CN, respectively

(Fig. 3.3a) [19,36]. Moreover, in the UV-visible spectra of BW, there is a broad absorption band in the region of 500-800 nm that can be ascribed to the LSPR of the effect of the zerovalent Bi [51,52]. Tauc's plot **(Fig. 3.3b)** was used to obtain the band gap of synthesized material. The band gap of BW is 2.52 eV, which is somewhat less than the reported value [25]. Such observation can be ascribed to the presence of plasmonic Bi in the Bi_2WO_6 and lattice. The bandgap of the composites gradually decreases from 2.52 eV to 2.22 eV upon increasing the g-CN loading suggesting their enhanced sensitivity towards visible light. The photoluminescence studies were inconclusive due to the non-fluorescent nature of the parent BW.

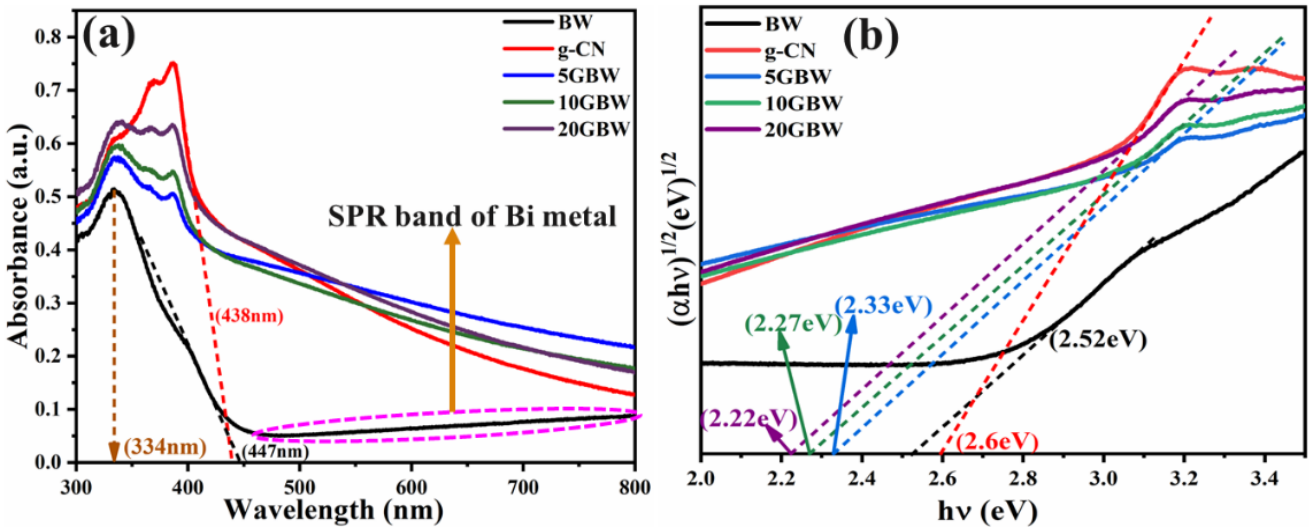

Fig. 3.3: (a) Diffuse reflectance spectra of bare BW, g-CN, and other composites (b) Tauc's Plot of the as-synthesized materials.

3.3.4 FTIR analysis

The structure of composites was further confirmed by FTIR. The 5GBW, 10GBW and 20GBW hybrid nanocomposites exhibit characteristic peaks of both g-CN and BW **(Fig. 3.4)**. The intensities of g-CN characteristics peaks were progressively enhanced with the increment in the extent of loading. The out-of-plane bending mode of the C−N heterocycle was observed at 808 cm^{-1} [38]. The peaks observed at 572 cm^{-1} and 706 cm^{-1} are assigned to the W−O and Bi−O stretching vibrations, respectively [53]. The stretching vibrational modes of the C−N are observed in the 1000–1800 cm^{-1} region, and the broad band between 3000–3500 cm^{-1} are attributable to the of C–H and N–H stretching modes [54].

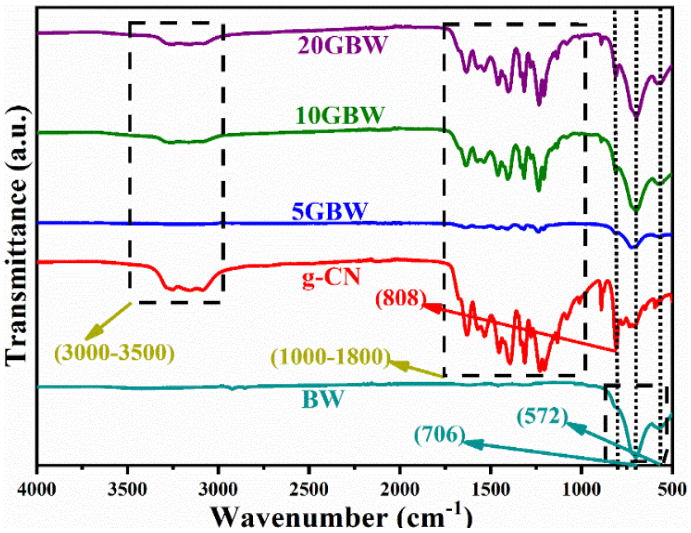

Fig. 3.4: FTIR patterns of bare BW, g-CN and different wt.% loading composites.

3.3.5 EIS studies

The transfer effectiveness of photogenerated carriers affects radical species production, measurable by EIS analysis [55]. To examine this characteristic, studies were conducted in the dark for both BW and the 20GBW composites. The radius of each arc was determined to understand the charge transfer process at the respective electrode/electrolyte interface [56]. Here, smaller arc radii reflect lower impedance and more efficient charge transfer. Nyquist plot of the 20GBW composite exhibits lesser radii compared to bare BW **(Fig. 3.5)**. This observation indicates that the 20GBW composite possesses a decreased charge transfer resistance relative to the unmodified BW [57]. Such observation suggests that the loading of g-CN promotes the charge transfer from BW to its surface, thereby reducing the charge transfer resistance. Therefore, the g-CN loaded composites can act as more efficient photocatalysts compared to the bare BW.

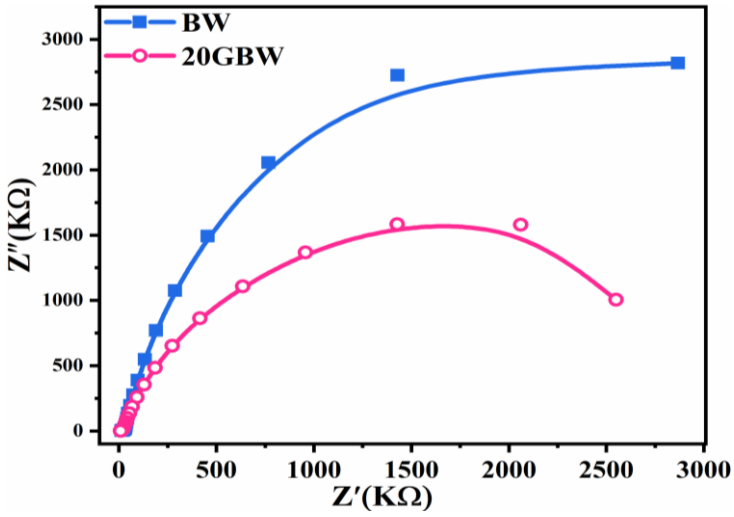

Fig. 3.5: EIS Nyquist plots of BW and 20GBW demonstrating their charge transfer characteristics

3.3.6 Morphology and Multielemental analysis

The morphological characteristics of pure Bi_2WO_6 and its 20GBW hybrid were examined using FE-SEM, as shown in **Fig. 3.6.** Notably, the bare Bi_2WO_6 displays a petal-like floral structure **[Fig. 3.6 (a-c)]** [25]. The existence of both CN layers and Bi_2WO_6 floral petals deposition is shown in the FE-SEM images of the 20GBW hybrid in **Fig. 3.6 (d-f)**, affirming the formation of the composite. EDS elemental mapping of the 20GBW hybrid reveals that all the constituent (Bi, W, O, N, and C) elements were homogeneously disseminated over its surface **(Fig. 3.7)**.

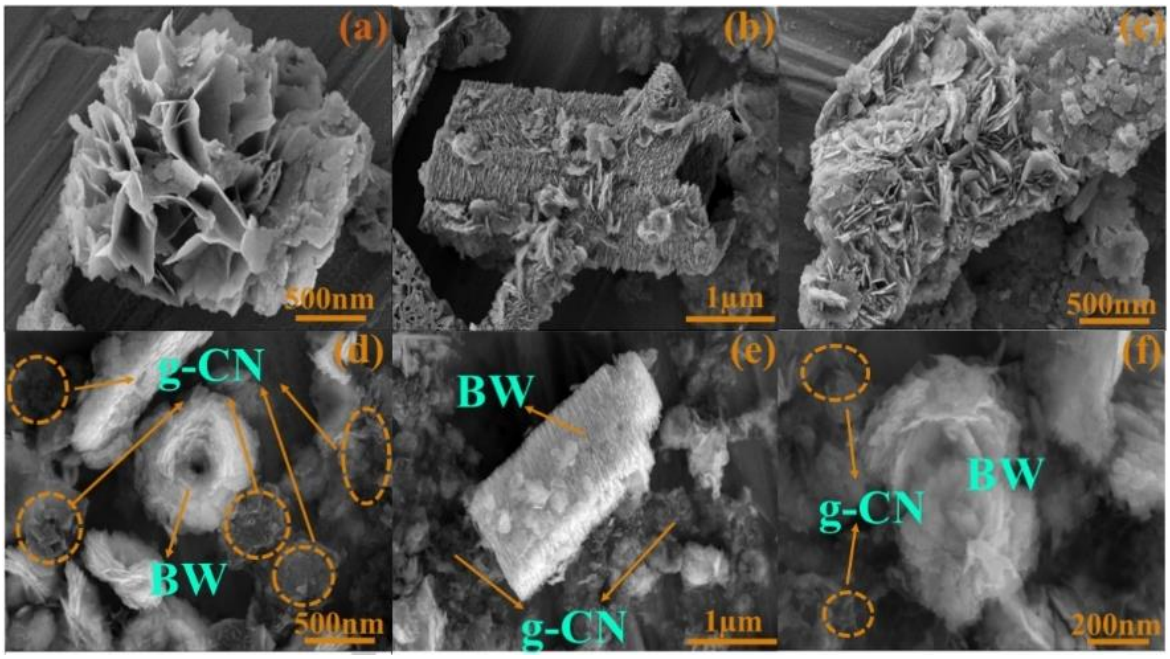

Fig. 3.6: FE-SEM images of (a-c) BW and (d-f) 20GBW hybrid composite.

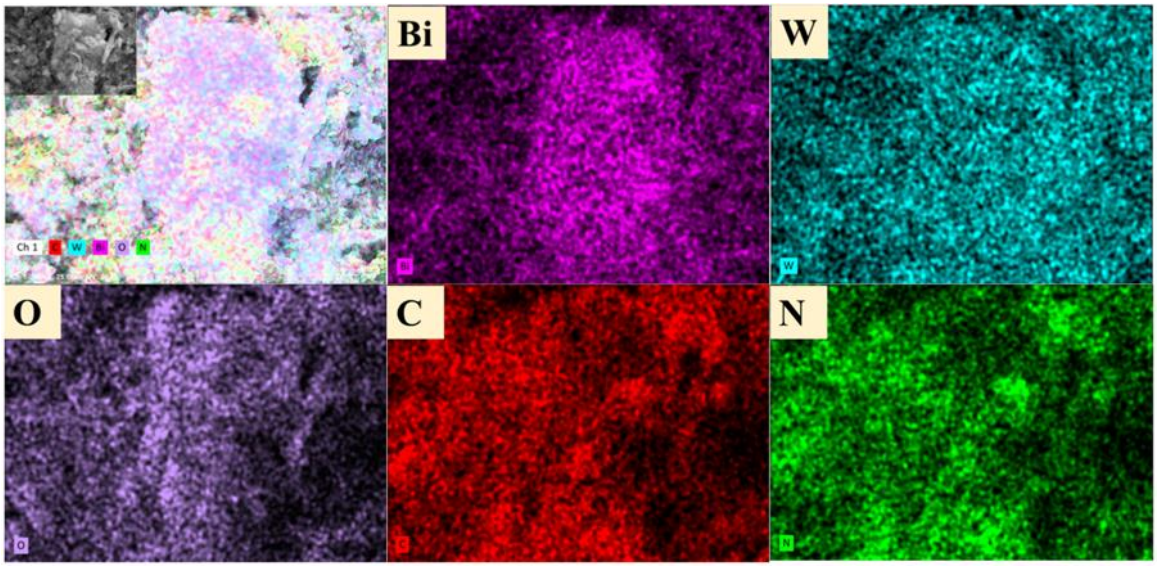

Fig. 3.7: EDS mapping of 20GBW composite showing the presence of uniformly distributed metal Bi, W, O, C and N in the composite.

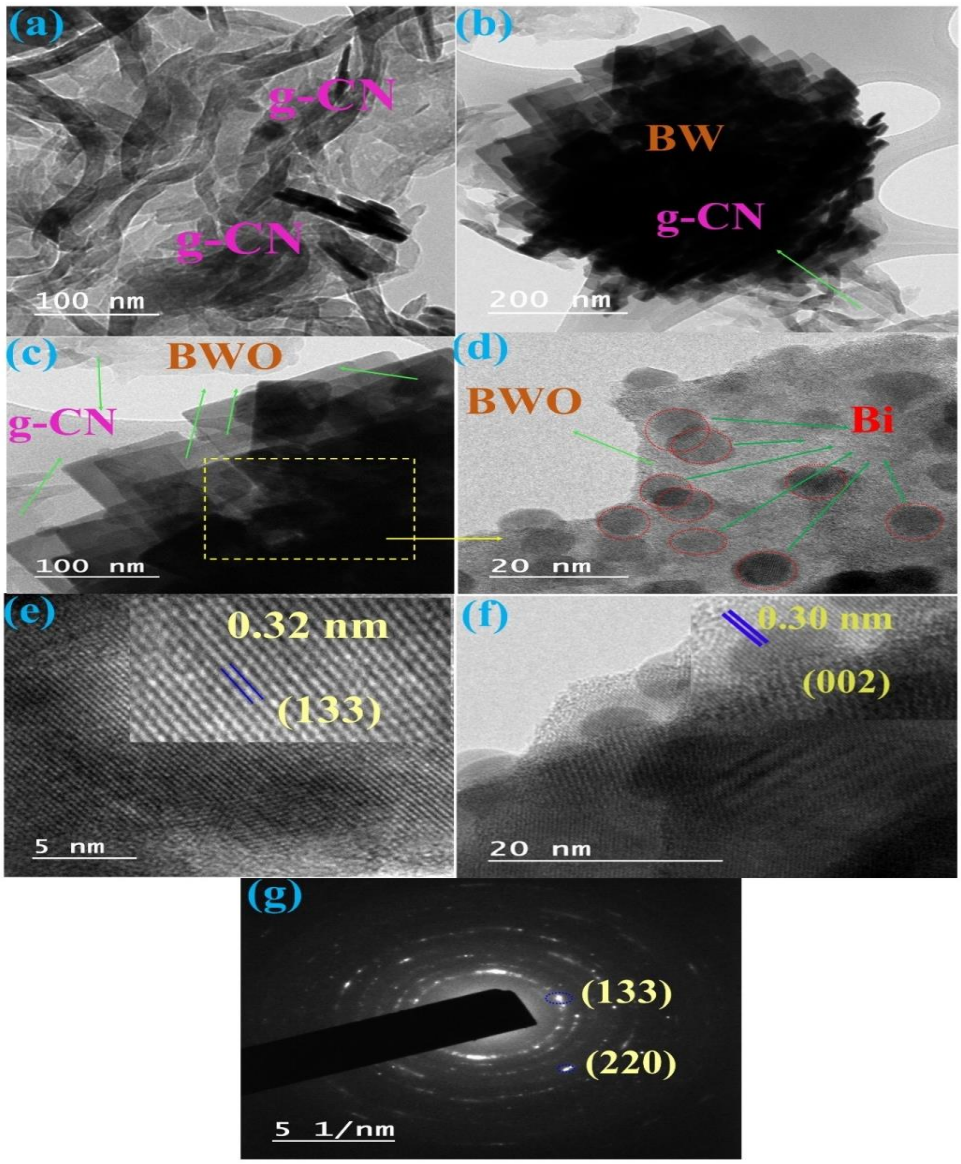

Fig. 3.8: (a) HRTEM image of bare g-CN, (b-d) HRTEM images, (e-f) lattice fringes, and (g) SAED pattern of the 20GBW composite.

To examine the morphology and crystallinity to a greater extent, the HRTEM studies were performed **(Fig. 3.8)**. The HRTEM image of g-CN confirms its sheet-like structure **(Fig. 3.8a)**. The HRTEM micrographs of 20GBW composites confirm the deposition of g-CN on the surface of Bi_2WO_6 (BWO) **[Fig. 3.8 (b-c)]** [36]. The darker square-shaped petal-like floral regions correspond to BWO, whereas the lighter sheet-like portions can be ascribed to g-CN **[Fig. 3.8 (b-c)]**. Furthermore, the deposition of spherical particles of Bi (0) over the BWO surface was also observed **(Fig. 3.8 d)**. Furthermore, the lattice fringes in **Fig. 3.8 (e)**, Additionally the lattice fringes match quite well with the (133) plane of BWO [25] and in **Fig. 3.8 (f)**, lattice fringes of g-CN having (002) plane. The selected area diffraction (SAED) pattern **(Fig. 3.8 g)** of 20GBW heterostructures consists of characteristic spots corresponding

to (133) and (220) crystallographic planes for the orthorhombic phase of BWO [25]. Such observations confirm the formation and crystallinity of the 20GBW ternary nanocomposite.

3.3.7 N_2 sorption analysis

To rationalize the variation of surface characteristics upon g-CN loading, BET sorption isotherms of the pristine BW and g-CN, as well as the 20GBW heterostructure, were recorded **(Fig. 3.9)**. All three samples display type-III sorption isotherm along with H3 hysteresis loop [58]. Such observation signifies the presence of small pores and weak adsorbent-adsorbate interactions. Among these, the g-CN possesses the highest specific surface area of 105 m^2/g due to its unique two-dimensional layer-like structure **(Fig. 3.9)**. Moreover, the 20GBW nanocomposite composite exhibits a significantly larger surface area compared to the bare BW. This is because loading of g-CN in BW surface increases the counts of active sites and, consequently, enhances the surface area. Due to its larger surface area, the ternary nanostructure can thus serve as a more effective photocatalyst [36].

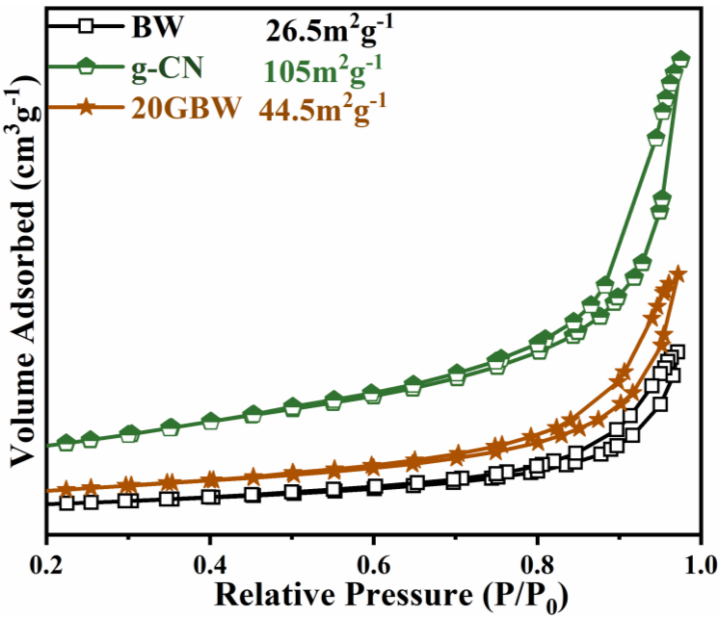

Fig. 3.9: N_2 adsorption-desorption analysis of bare BW, g-CN, and 20GBW composite.

3.3.8 Photocatalytic degradation

The photocatalytic activity of pristine BW, g-CN, and all three ternary composites (5GBW, 10 GBW, and 20 GBW) was scrutinized under visible light **(Fig. 3.10 and 3.11)**. At first, the reaction mixture was stirred for 30 minutes in the dark to ensure the adsorption-desorption equilibrium. The pristine BW shows insignificant photocatalytic degradation efficiency **(Fig. 3.10 a)**, whereas the 5GBW, 10GBW, and 20GBW hybrids are having degradation efficiencies are ~30(3) %, ~58(3) %, and ~89(2) %, respectively, after 300 minutes of reaction time **[Fig. 3.10 (a-b)]** [36].

It was observed that in the case of g-CN, there is a significant amount of removal of the pollutant under the dark only, and it shows nominal changes in the removal efficiency under visible light, suggesting extensive adsorption of the contaminant without any substantial degradation **(Fig. 3.12)**. Such an outcome is due to the excessive adsorption of reactive orange 16 in the g-CN surface, thereby blocking the active sites to reduce the probability of photocatalytic degradation. To validate such observation, the DRS spectra of g-CN and 20 GBW were recorded before and after photocatalytic reactions **[Fig. 3.10 (c-d)]**. It was found that for g-CN, there is a distinct peak analogous to the reactive orange 16 dye **(Fig. 3.10 c)**. At the same time, the DRS patterns of the 20GBW composite remain practically identical after the reaction **(Fig. 3.10 d)**. Such observations confirm that the g-CN acts as an adsorbent only, but the 20GBW composite promotes photocatalytic degradation.

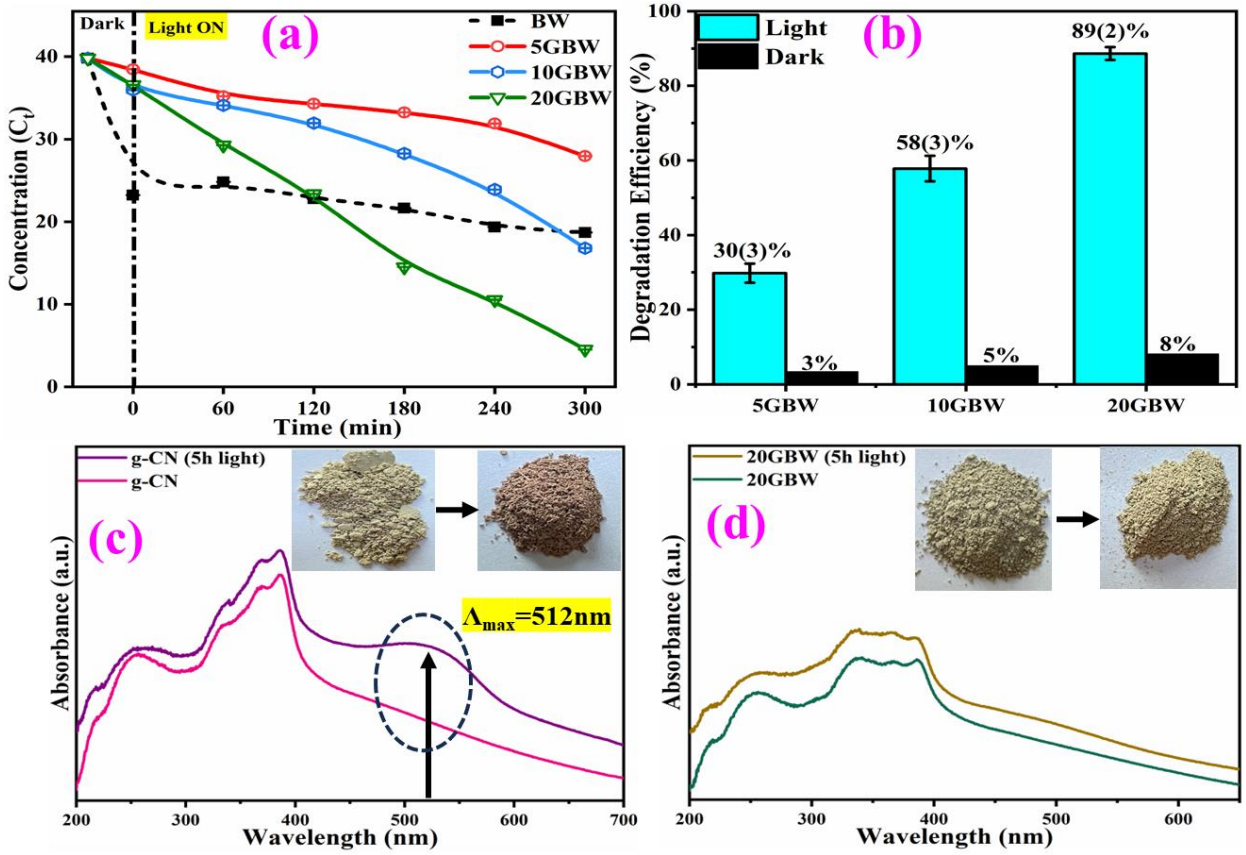

Fig. 3.10: (a) Change in concentration with time for RO-16 in the presence of different photocatalysts, (b) comparison degradation efficiency of 5GBW, 10GBW, and 20GBW towards RO-16 and DRS plots for (c) g-CN and (d) 20GBW before and after photocatalytic reactions.

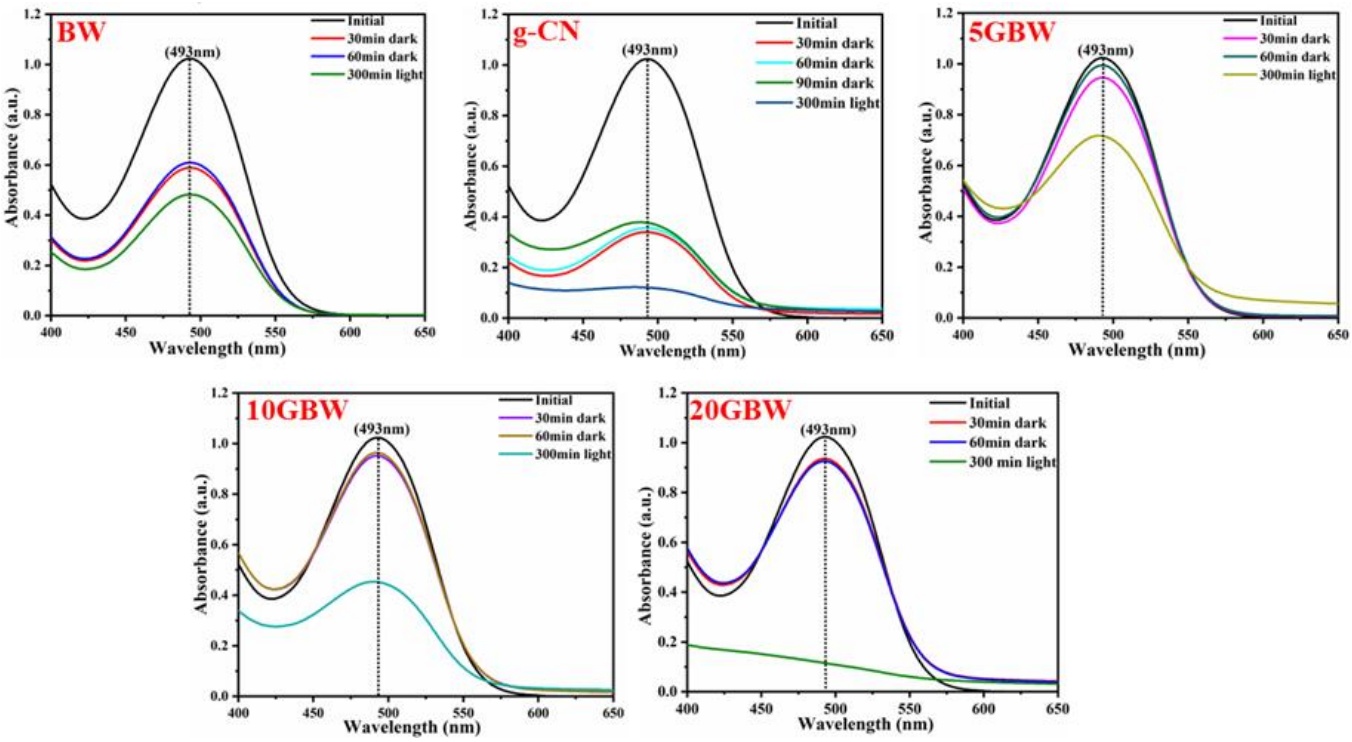

Fig. 3.11: Kinetic study of bare BW, g-CN, and different wt.% loaded composite.

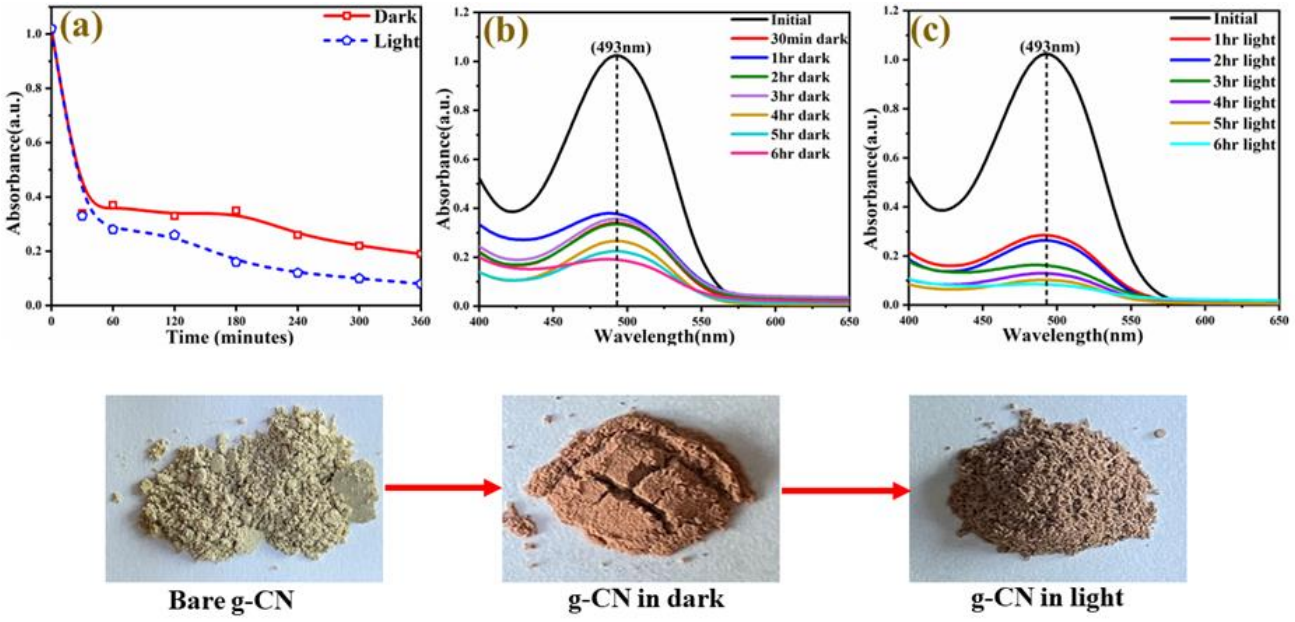

Fig. 3.12: Catalytic activity of g-CN showing majorly working in the dark environment rather than in light irradiation for 360min.

All the photodegradation followed the pseudo-zero-order kinetic reaction shown in Equation 3 **(Fig. 3.13)** [59].

$$C_t = -kt + C_O \qquad (3)$$

Where C_0 and C_t represent the concentration of the pollutant at the start of the reaction and after time 't', whereas k stands for the pseudo-zero-order rate constant. The pseudo-zero-order kinetics was further validated by determining the half-life values **(Fig. 3.14)** in the case of the 20GBW composite. The half-life values are almost linearly proportional to the initial concentration, thereby confirming the pseudo-zero-order kinetic model.

Notably, the reaction rate improves with increasing the g-CN loading, and the 20GBW composite possesses the highest rate constant of 0.107(5) mol L^{-1} min^{-1} **(Fig. 3.13).**

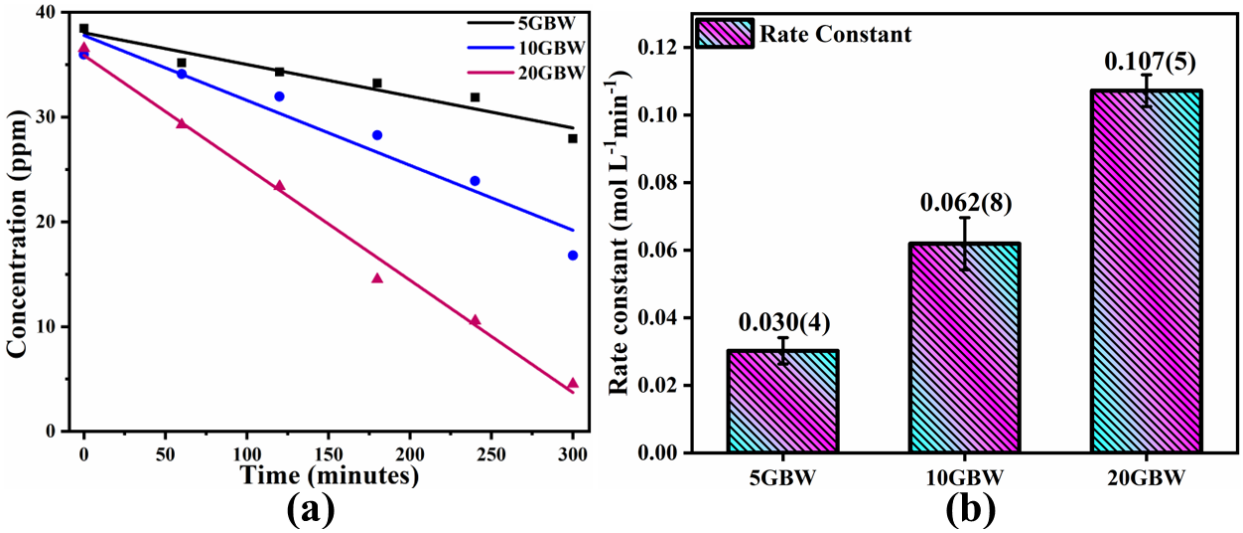

Fig. 3.13: Photocatalytic degradation trends with concentration (ppm) and at different time (min) intervals with as-synthesized catalyst (a) and (b) represents the bar plot of rate constant value of 5GBW, 10GBW, and 20GBW correspondingly.

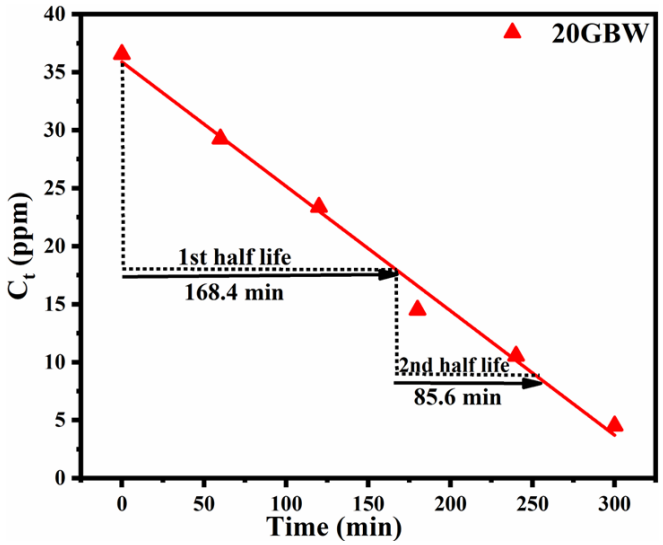

Fig. 3.14: Half-life calculation for zero order kinetic reaction of 20GBW composite.

To ensure the optimal usage of the catalyst, the effect of the catalyst amount was inspected **(Fig. 3.15)**. It has been observed that upon increasing the catalyst dosage from 5 mg to 7.5 mg, the photodegradation efficiency increases from 43% to 89% owing to the accessibility of a larger number of active sites. But upon further enhancement of catalyst amount, there is no change in the degradation efficiency.

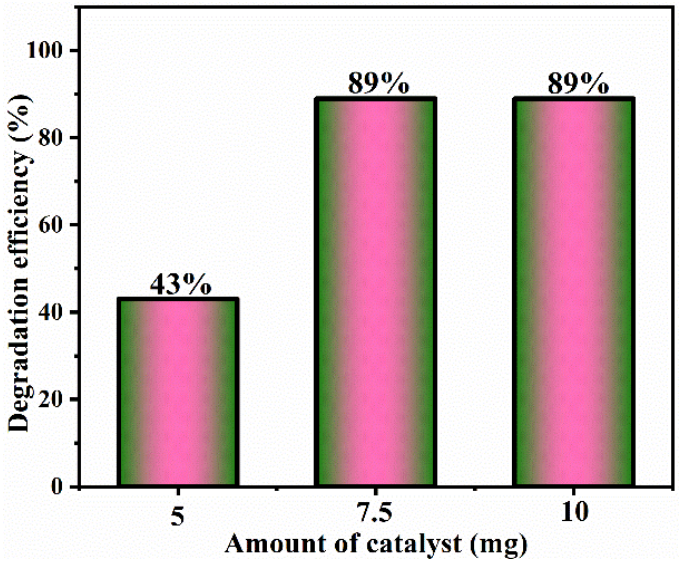

Fig. 3.15: Outcome of catalyst loading on the photocatalytic degradation efficiency of 20GBW composite towards the removal of RO16 dye.

In order to confirm the demineralization of RO-16, the total organic carbon (TOC) before and after the photocatalytic reaction was determined for the 20 GBW photocatalyst. It was observed that the TOC of the reaction mixture decreased from 53 to 16 ppm which of correspond to a demineralization efficiency ~70%. Such observation suggests that a significant portion of the RO-16 has been completely decomposed.

3.3.9 Mechanistic study

3.3.9.1 Proposed Mechanism

To understand the reaction mechanism, XPS valence band spectra determined the band positions BW and g-CN **[Fig. 3.16 (a-b)]**. The valence band (VB) energies of BW and g-CN were found to be +1.44eV and +1.88eV, respectively. Then, the conduction band (CB) positions were calculated by using the band gap values for the respective semiconductors, which are −1.08eV and −0.72eV, respectively. The band positions indicate that the 20GBW composite acts as a type-II heterojunction **(Fig. 3.16 c)** [38], in which excited electrons in the CB of BW migrate to the CB of g-CN, and the holes in VB of g-CN will transfer to the VB of BW, that minimizes the electron-hole pair recombination. As a reduction potential is smaller, compared to the $OH^-/OH^\bullet$ redox couple. So, the

production of hydroxyl radicals is not favourable. Therefore, the holes and superoxide anions can act as reactive species in the photodegradation reactions [36].

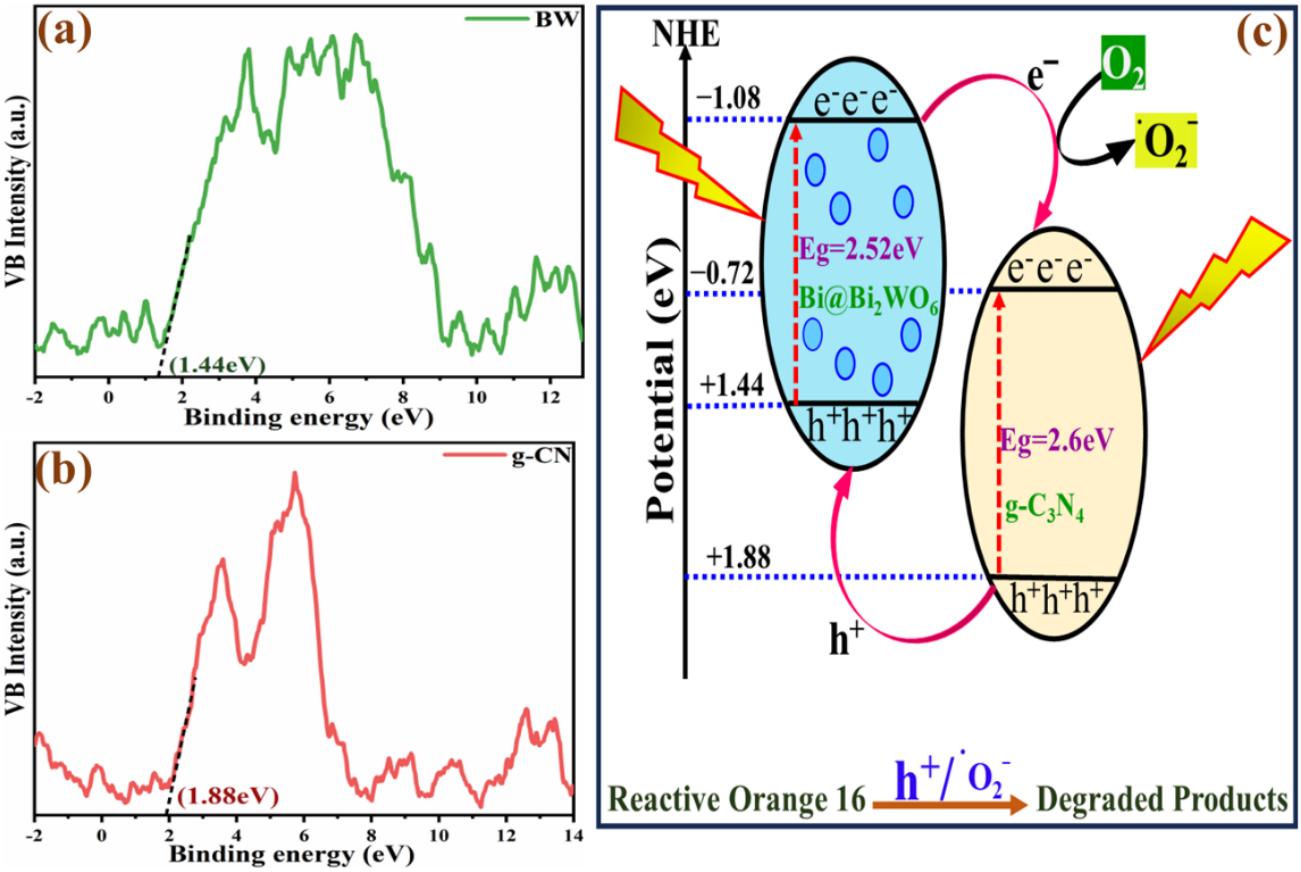

Fig. 3.16: XPS valence band spectra of (a) BW and (b) g-CN and (c) schematic representation for the type-II heterojunction formed in 20GBW composite and its photocatalytic activity towards the removal of reactive orange 16.

3.3.9.2 Scavengers effect

Various control experiments were conducted to confirm the contributions of reactive species **(Fig. 3.17)**. It was found that the addition of NH_4SCN and EDTA to the reaction mixture reduced the degradation efficiency from 89% to 70% and 65%, respectively. Because they act as hole scavengers, consequently inhibiting the oxidation of the pollutant with the hole. Furthermore, after Ar gas purging, the photocatalytic degradation efficiency decreases to 28%. This is because argon purging diminishes the possibility of producing superoxide radicals by removing oxygen from the reaction mixture. All these outcomes confirm that both superoxide anions and holes indeed play crucial roles in photocatalytic oxidation reactions [60,61]. However, the addition of *iso*-propyl alcohol (iPA) to the reaction mixture does not change the degradation efficiency significantly. So, it suggests that hydroxyl radicals are not involved in the degradation process.

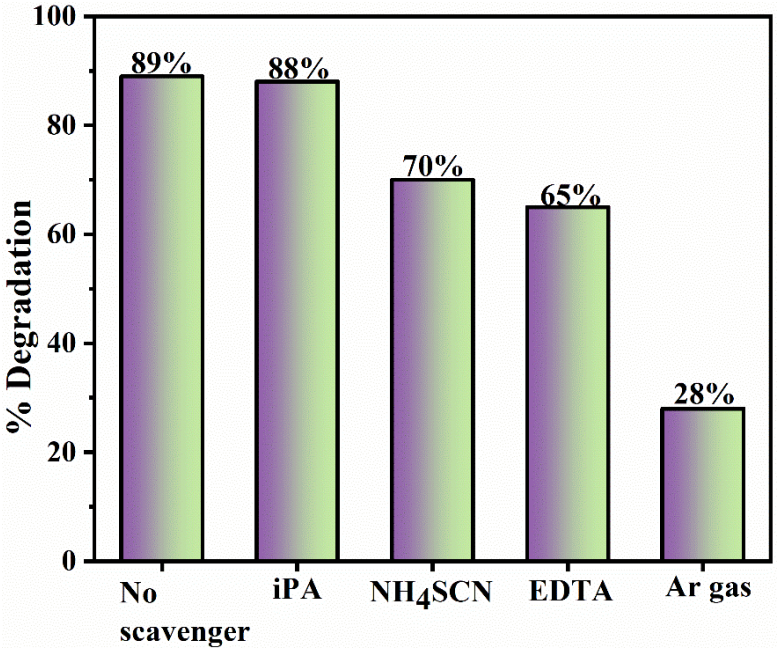

Fig. 3.17: Changes in photocatalytic degradation activity of 20GBW composite after Ar purging and addition of NH_4SCN, EDTA and iPA in the reaction mixture.

3.3.10 HRMS Studies

To gather a broader perspective about the reaction mechanism, high-resolution mass spectrometry (HR-MS) studies were performed **(Scheme 1**, **Fig. 3.18-3.19)**. The peaks as m/z 618 and 574 are characteristic of the original and protonated forms of the RO-16 dye **(Fig. 3.18).** Moreover, the peaks as m/z 437 (I1), 229 (I2), 126 (I3), 202 (I4), 274 (I5) and 163 (I6) signify the formation of different smaller fragments during the photodegradation process. It is fascinating to note that with the progress of the reaction, the peaks corresponding to the unreacted RO-16 dye completely disappear, and the relative intensities of the smaller fragments increase **(Fig. 3.19)** substantially, thus providing the necessary evidence for the photocatalytic degradation process.

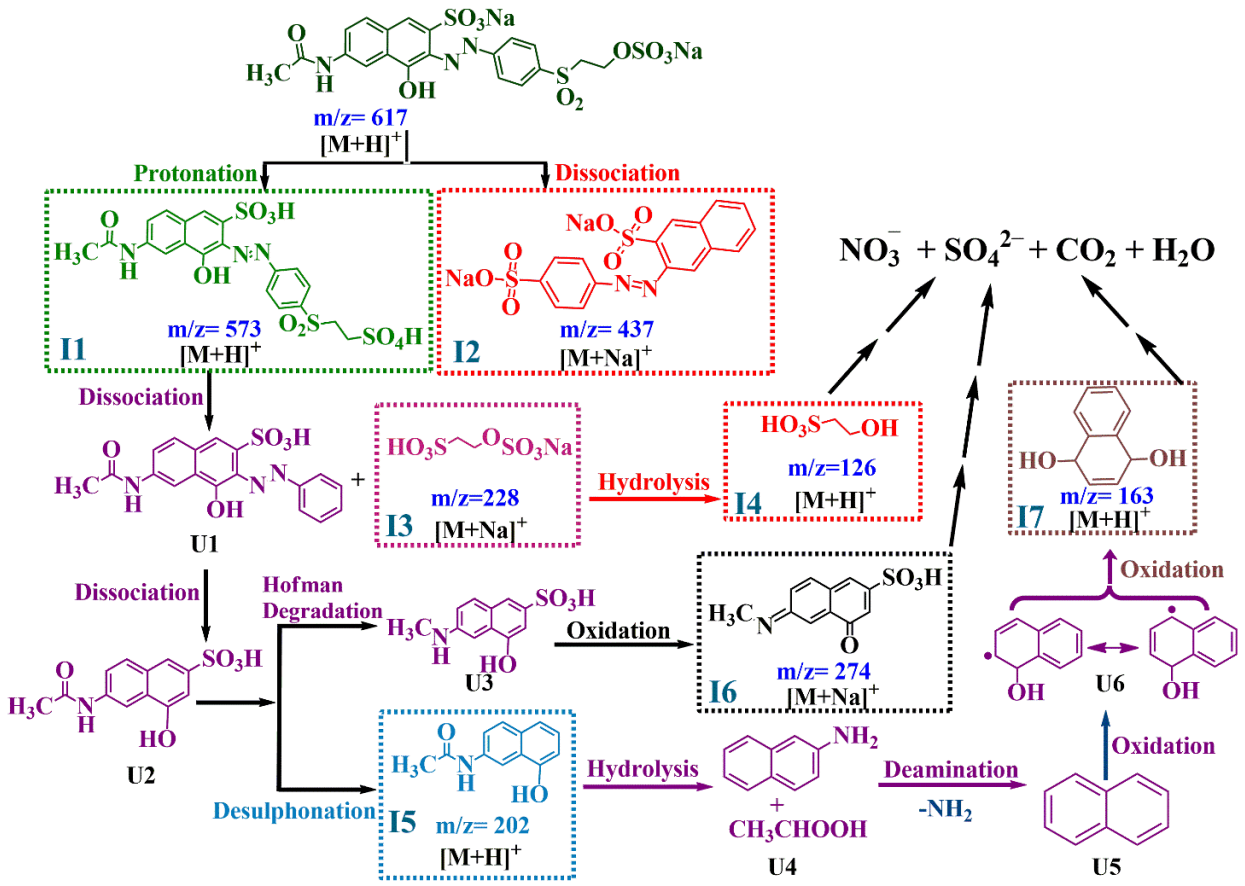

Scheme 1: The probable mechanism for the photodegradation of reactive orange 16 using 20GBW nanocomposite (I1 to I7 stands for identified fragments, and U1 to U6 stands for unidentified fragments).

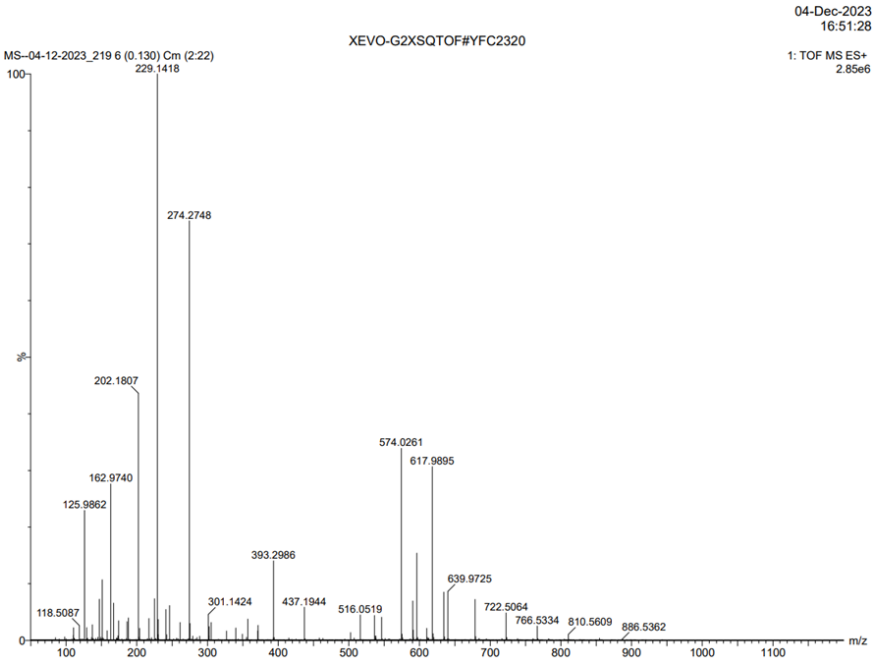

Fig. 3.18: HRMS spectrum of the reaction mixture after 150 minutes of reaction time.

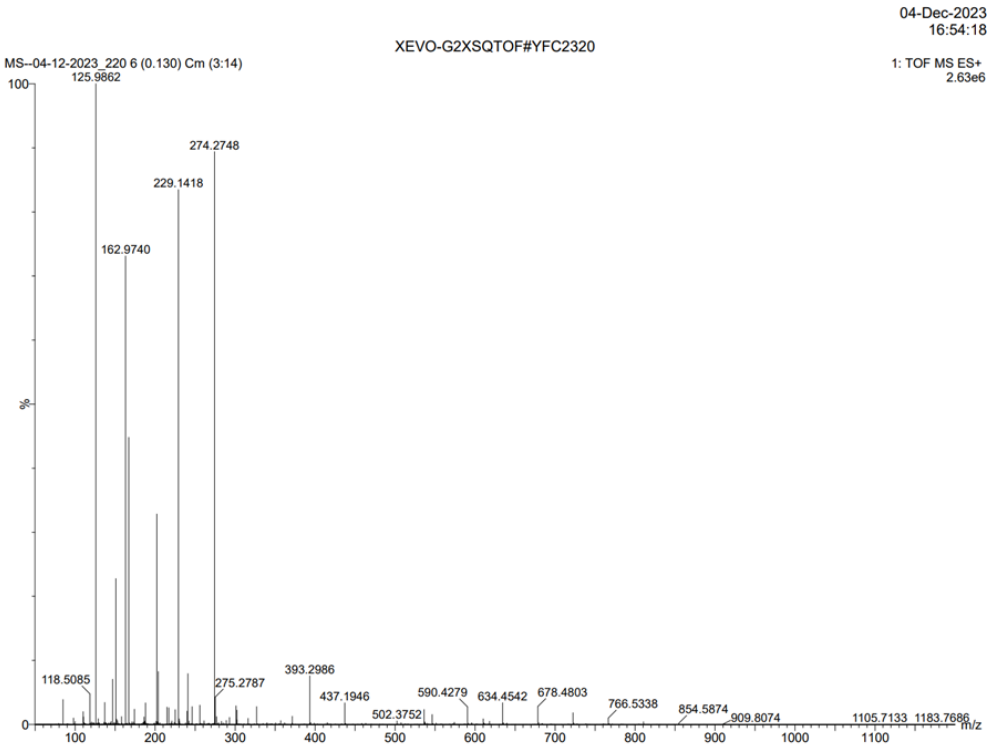

Fig. 3.19: HRMS spectrum of the reaction mixture after 300 minutes of reaction time.

3.3.11 Recyclability and stability of the photocatalyst

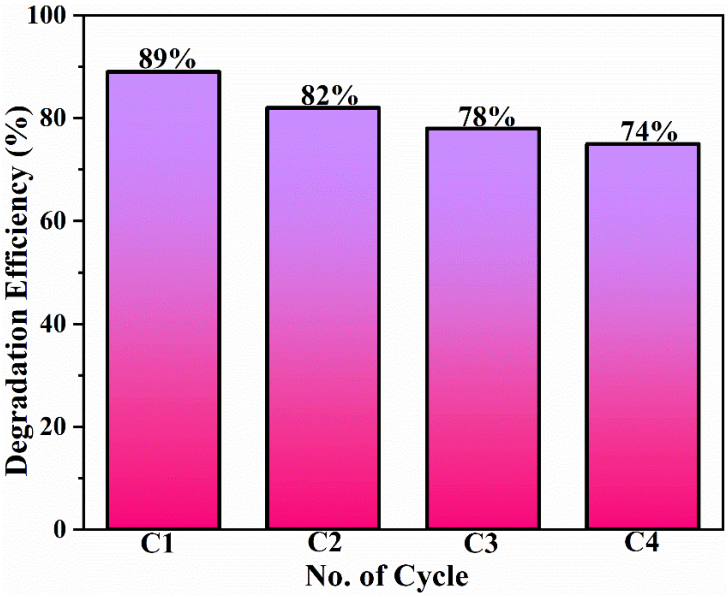

Fig. 3.20: Recyclability of the 20GBW composite for four consecutive cycles of RO-16 degradation with a visible light source.

The recyclability and stability of a catalyst are extremely crucial for its prospective applications. Once the reaction was completed, the catalyst was removed from the reaction mixture and utilized in a subsequent reaction. It has been observed that after the fourth cycle, the photocatalytic activity of the

20GBW composite is reduced by only 15% compared to the first cycle **(Fig. 3.20)**, thereby suggesting excellent reusability of the hybrid composite. The apparent loss of photocatalytic activity can be attributed to the loss of catalyst that occurred during the washing and separation of the photocatalyst.

To assess the stability, furthermore, the XRD, FTIR and FESEM of the 20GBW composite were executed before and after the photocatalytic reaction **(Figs. 3.21).** Remarkably, both the XRD patterns and the FTIR spectra remained almost exactly the same before and after the photocatalytic reactions (Fig. 14). Moreover, FESEM studies reveal that the 20GBW composites possess similar morphology before and after the reactions **(Fig. 3.22).** Therefore, such observations rule out any probability of leaching of the catalyst during catalytic reactions and ascertain the stability of the 20GBW composite.

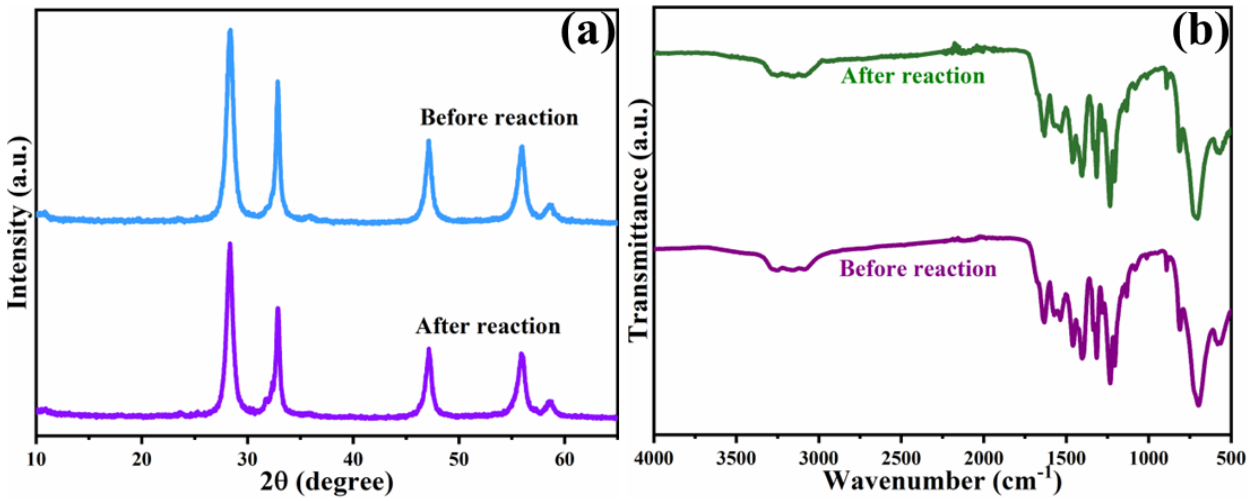

Fig. 3.21: (a) XRD and (b) FTIR plots of 20GBW photocatalyst before and after the photocatalytic reaction.

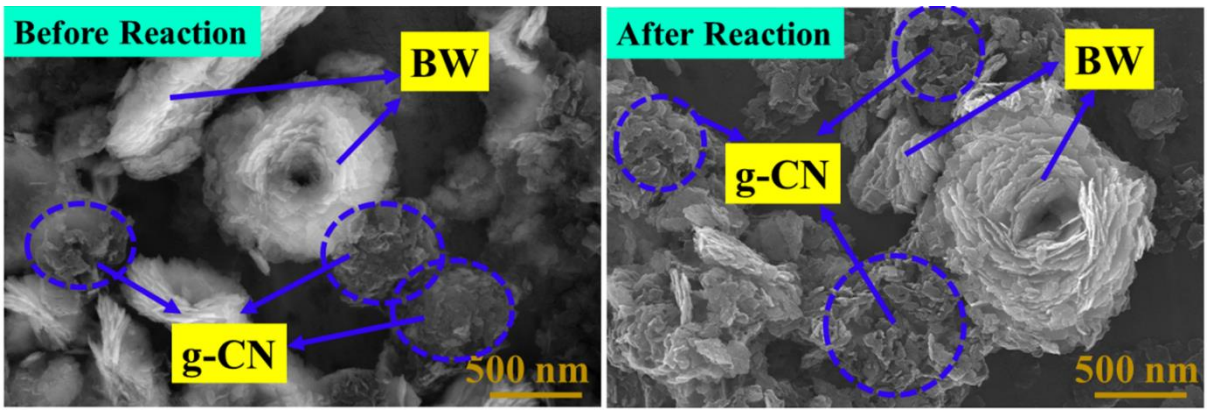

Fig. 3.22: FESEM images of 20GBW photocatalyst before and after the photocatalytic reaction.

3.4 Comparison of degradation efficiency:

Remarkably, the 20GBW composite shows either similar or greater photocatalytic activity towards the degradation of reactive orange 16 compared to the several reported catalysts, as shown in **Table 1.**

Table 1: Comparative photodegradation efficiencies of different catalysts towards reactive orange 16.

S. No.	Catalyst	Degradation efficiency	Nature of irradiation	Conc. of pollutants	Catalyst dose	Reaction time	References
1.	$MgO/g\text{-}C_3N_4$	82%	visible	2 mg/L	0.2 g/500 mL	30 min	[62]
2.	TiO_2/Al_2O_3	85%	UV	20 mg/L	20 g	120 min	[63]
3.	$Bi_5Nb_3O_{15}$/N-rGO	84%	visible	30 ppm	100 mg	180 min	[64]
4.	CeO_2/ZnO	90%	Simulated solar	50 mg/L	100 mg	180 min	[65]
5.	N, S co-doped TiO_2/graphene	96%	visible	3.12×10^{-5} M	50 mg	120 min	[66]
6.	Bi-doped g-C_3N_4/Bi_2WO_6 (20GBW)	89%	visible	40 ppm	7.5 mg/5mL	300 min	This work

3.5 Conclusion:

The report demonstrates the preparation of zerovalent Bi-doped g-C_3N_4/Bi_2WO_6 ternary heterostructures and studies their photodegradation activity towards reactive orange 16 dye. Markedly, the synthetic process does not require the addition of any other reductant. The surfactant CTAB acts as a mild reducing agent to affect the concerted reduction of Bi (III) to zerovalent Bi during Bi_2WO_6 synthesis. Also, due to in-situ reduction, the Bi (0) is dispersed throughout the Bi_2WO_6 matrix. The loading of g-C_3N_4 facilitates the electron transfer process through the formation of type-II heterojunctions, while the zerovalent Bi enhances the visible light response via localized surface plasmon resonance effect. As a result, the nanocomposites have superior photodegradation activity towards reactive orange 16 under visible light. The superoxide ions and hydroxide radicals are the key reactive species, as indicated by controlled studies. The HRMS studies affirm the formation of different intermediates to provide greater insight into the reaction mechanism. Additionally, the photocatalyst possesses excellent stability and reusability, validated by the recyclability analysis. Therefore, the present work can open a new dimension of preparing plasmonic element-doped materials for the removal of toxic contaminants from wastewater.

References:

1 A. Tkaczyk, K. Mitrowska and A. Posyniak, Synthetic organic dyes as contaminants of the aquatic environment and their implications for ecosystems: A review, *Sci. Total Environ*., 2020, **717**, 137222.

2 U. H. Siddiqua, S. Ali, M. Iqbal and T. Hussain, Relationship between structure and dyeing properties of reactive dyes for cotton dyeing, *J. Mol. Liq.*, 2017, **241**, 839.

3 M. Kokturk, F. Altindag, G. Ozhan, M. H. Çalimli and M. S. Nas, Textile dyes Maxilon blue 5G and Reactive blue 203 induce acute toxicity and DNA damage during embryonic development of Danio rerio, *Comp. Biochem. Physiol. Part -C: Toxicol*., 2021, **242**, 108947.

4 H. Kusic, N. Koprivanac and A. L. Bozic, Environmental aspects on the photodegradation of reactive triazine dyes in aqueous media, *J. Photochem. Photobiol. A Chem.*, 2013, **252**, 131.

5 N. H. Malik, H. Zain and N. Ali, Organismic-level acute toxicology profiling of reactive azo dyes, *Environ. Monit. Assess*., 2018, **190**, 612.

6 G. M. L. B. B. L. de B. R. Daniela Morais Leme Gisele Augusto Rodrigues de Oliveira and D. P. de Oliveira, Eco- and Genotoxicological Assessments of Two Reactive Textile Dyes, *J. Toxicol. Environ. Health A.,* 2015, **78**, 287.

7 N. Tara, M. Arslan, Z. Hussain, M. Iqbal, Q. M. Khan and M. Afzal, On-site performance of floating treatment wetland macrocosms augmented with dye-degrading bacteria for the remediation of textile industry wastewater, *J. Clean Prod.*, 2019, **217**, 541.

8 N. Kaur, S. K. Shahi and V. Singh, Anomalous behaviour of visible light active TiO_2 for the photocatalytic degradation of different Reactive dyes, *Photochem. Photobiol. Sci.,* 2015, **14**, 2024.

9 E. Hu, S. Shang and A. K. L. Chiu, Removal of Reactive Dyes in Textile Effluents by Catalytic Ozonation Pursuing on- Site Effluent Recycling, *Molecules*, 2019, **24**, 2755.

10 H. M. Solayman, M. A. Hossen, A. Abd Aziz, N. Y. Yahya, K. H. Leong, L. C. Sim, M. U. Monir and K. D. Zoh, Performance evaluation of dye wastewater treatment technologies: A review, *J. Environ. Chem. Eng.*, 2023, **11**, 109610.

11 S. Bilgi and C. Demir, Identification of photooxidation degradation products of C.I. Reactive Orange 16 dye by gas chromatography–mass spectrometry, *Dyes and Pigments*, 2005, **66**, 69.

12 S. Pu, Q. Zhao, X. Luo, D. Wang, K. Lei, Y. Duan, L. Mao, W. Feng and Y. Sun, In-situ synthesis of $AgCl/WO_3$ loaded with g-C_3N_4 as dual Z-scheme heterojunction for boosting photocatalytic degradation of antibiotics, *Surf. Interfaces*., 2024, **46**, 104016.

13 H. Wu, L. Li, S. Wang, N. Zhu, Z. Li, L. Zhao and Y. Wang, Recent advances of semiconductor photocatalysis for water pollutant treatment: mechanisms, materials and applications, *Phys. Chem. Chem. Phys*., 2023, **25**, 25899.

14 G. Zhang, S. Li, L. Zhang and Y. Tian, Structural tuning of bismuth molybdate composite photocatalyst for pollutants removal, *Surf. and Interfaces.*, 2024, **44**, 103707.

15 J. Xu, J. Shen, H. Jiang, X. Yu, W. Ahmad Qureshi, C. Maouche, J. Gao, J. Yang and Q. Liu, Progress and challenges in full spectrum photocatalysts: Mechanism and photocatalytic applications, *J. Ind. Eng. Chem.,* 2023, **119**, 112.

16 T. Chen, L. Liu, C. Hu and H. Huang, Recent advances on Bi_2WO_6-based photocatalysts for environmental and energy applications, *Chinese J. Catal.*, 2021, **42**, 1413.

17 A. S. Belousov, A. A. Parkhacheva, E. V. Suleimanov and I. Shafiq, Potential of Bi_2WO_6-based heterojunction photocatalysts for environmental remediation, *Mater. Today Chem.*, 2023, **32**, 101633.

18 D. A. Collu, C. Carucci, M. Piludu, D. F. Parsons and A. Salis, Aurivillius Oxides Nanosheets-Based Photocatalysts for Efficient Oxidation of Malachite Green Dye, *Int. J. Mol. Sci.*, 2022, **23**, 5422.

19 S. Yu, Y. Zhang, M. Li, X. Du and H. Huang, Non-noble metal Bi deposition by utilizing Bi_2WO_6 as the self-sacrificing template for enhancing visible light photocatalytic activity, *Appl. Surf. Sci.*, 2017, **391**, 491.

20 N. D. Phu, L. H. Hoang, P. Van Hai, T. Q. Huy, X. B. Chen and W. C. Chou, Photocatalytic activity enhancement of Bi_2WO_6 nanoparticles by Ag doping and Ag nanoparticles modification, *J. Alloys Compd.*, 2020, **824**, 153914.

21 X. Zheng, T. Han and H. Shi, Cu-doped Bi_2WO_6-x photocatalyst with efficient charge separation ability for enhanced peroxymonosulfate activation, *J. Mol. Liq.*, 2023, **391**, 123273.

22 Z. Ni, Y. Shen, L. H. Xu, G. Xiang, M. Chen, N. Shen, K. Li and K. Ni, Facile construction of 3D hierarchical flower-like Ag_2WO_4/Bi_2WO_6 Z-scheme heterojunction photocatalyst with enhanced visible light photocatalytic activity, *Appl. Surf. Sci.*, 2022, **576**, 151868.

23 X. Ren, K. Wu, Z. Qin, X. Zhao and H. Yang, The construction of type II heterojunction of Bi_2WO_6/BiOBr photocatalyst with improved photocatalytic performance, *J. Alloys Compd.*, 2019, **788**, 102.

24 R. Kumar, A. Sudhaik, A. A. P. Khan, P. Raizada, A. M. Asiri, S. Mohapatra, S. Thakur, V. K. Thakur and P. Singh, Current status on designing of dual Z-scheme photocatalysts for energy and environmental applications, *J. Ind. Eng. Chem.,* 2022, **106**, 340.

25 R. Zhang, J. Jiang and K. Zeng, Synthesis of Bi_2WO_6/g-C_3N_4 heterojunction on activated carbon fiber membrane as a thin-film photocatalyst for treating antibiotic wastewater, *Inorg. Chem. Commun.*, 2022, **140**, 109418.

26 X. Lian, W. Xue, S. Dong, E. Liu, H. Li and K. Xu, Construction of S-scheme Bi_2WO_6/g-C_3N_4 heterostructure nanosheets with enhanced visible-light photocatalytic degradation for ammonium dinitramide, *J. Hazard Mater.*, 2021, **412**, 125217.

27 C. Yang, H. Chai, P. Xu, P. Wang, X. Wang, T. Shen, Q. Zheng and G. Zhang, One-step synthesis of a 3D/2D Bi_2WO_6/g-C_3N_4 heterojunction for effective photocatalytic degradation of atrazine: Kinetics, degradation mechanisms and ecotoxicity, *Sep. Purif. Technol.*, 2022, **288**, 120609.

28 L. Mascaretti and A. Naldoni, Hot electron and thermal effects in plasmonic photocatalysis, *J. Appl. Phys.*, 2020, **128**, 041101.

29 N. Wu, Plasmonic metal–semiconductor photocatalysts and photoelectrochemical cells: a review, *Nanoscale*, 2018, **10**, 2679.

30 P. Soni, B. Pal and R. K. Das, Influence of β-CD and Ag deposition over TiO_2 towards photocatalytic oxidation of urea under solar irradiation, *J. Environ. Chem. Eng.*, 2024, **12**, 112150.

31 F. Dong, Q. Li, Y. Sun and W. K. Ho, Noble Metal-Like Behaviour of Plasmonic Bi Particles as a Cocatalyst Deposited on $(BiO)_2CO_3$ Microspheres for Efficient Visible Light Photocatalysis, *ACS Catal.*, 2014, **4**, 4341.

32 Z. Zhao, W. Zhang, Y. Sun, J. Yu, Y. Zhang, H. Wang, F. Dong and Z. Wu, Bi Cocatalyst/Bi_2MoO_6 Microspheres Nanohybrid with SPR-Promoted Visible-Light Photocatalysis, *J. Phys. Chem. C.,* 2016, **120**, 11889.

33 R. Li, X. Wang and M. Chen, Non-Noble Metal and Nonmetallic Plasmonic Nanomaterials with Located Surface Plasmon Resonance Effects: Photocatalytic Performance and Applications, *Catal.*, 2023, **13**, 940.

34 C. Yue, L. Zhu, Y. Qiu, Z. Du, J. Qiu, F. Liu and F. Wang, Recent advances of plasmonic elemental Bi based photocatalysts in environmental remediation and energy conversion, *J. Clean Prod.*, 2023, **392**, 136017.

35 J. Tang, J. Huang and S. Q. Man, Preparation of gold nanoparticles by surfactant-promoted reductive reaction without extra reducing agent, *Spectrochim. Acta. A. Mol. Biomol. Spectrosc.*, 2013, **103**, 349.

36 P. Rohilla, B. Pal and R. K. Das, Improved photocatalytic degradation of rhodamine B by g-C_3N_4 loaded $BiVO_4$ nanocomposites, *Heliyon*, 2023, **9**, e21900.

37 W. Guo, K. Fan, J. Zhang and C. Xu, 2D/2D Z-scheme Bi_2WO_6/Porous-g-C_3N_4 with synergy of adsorption and visible-light-driven photodegradation, *Appl. Surf. Sci.*, 2018, **447**, 125.

38 F. Chen, D. Li, B. Luo, M. Chen and W. Shi, Two-dimensional heterojunction photocatalysts constructed by graphite-like C_3N_4 and Bi_2WO_6 nanosheets: Enhanced photocatalytic activities for water purification, *J. Alloys Compd.*, 2017, **694**, 193.

39 D. Monga, D. Ilager, N. P. Shetti, S. Basu and T. M. Aminabhavi, 2D/2d heterojunction of MoS_2/g-C_3N_4 nanoflowers for enhanced visible-light-driven photocatalytic and electrochemical degradation of organic pollutants, *J. Environ. Manage.*, 2020, **274**, 111208.

40 D. Y. Liu, J. H. Dong, F. M. Liu, X. F. Gao, Y. Yu, S. B. Zhang, L. M. Dong and Y. K. Guo, Synthesis and photocatalytic performance of g-C_3N_4 composites, 2019, **15**, 239.

41 J. Wang, L. Tang, G. Zeng, Y. Liu, Y. Zhou, Y. Deng, J. Wang and B. Peng, Plasmonic Bi Metal Deposition and g-C_3N_4 Coating on Bi_2WO_6 Microspheres for Efficient Visible-Light Photocatalysis, *ACS Sustain. Chem. Eng.*, 2017, **5**, 1062.

42 J. Tang, J. Huang and S. Q. Man, Preparation of gold nanoparticles by surfactant-promoted reductive reaction without extra reducing agent, *Spectrochim. Acta. A. Mol. Biomol. Spectrosc.*, 2013, **103**, 349.

43 Y. Zhou, S. Ren, Q. Dong, Y. Li and H. Ding, One-pot preparation of Bi/Bi_2WO_6/reduced graphene oxide as a plasmonic photocatalyst with improved activity under visible ligh, *RSC Adv.*, 2016, **6**, 102875.

44 Z. Wang, L. Zhang, X. Zhang, C. Hu, L. Wang, B. Shi and X. Cao, Enhanced photocatalytic destruction of pollutants by surface W vacancies in VW-Bi_2WO_6 under visible light, *J. Colloid Interface Sci.*, 2020, **576**, 385.

45 P. Jiménez-Calvo, C. Marchal, T. Cottineau, V. Caps and V. Keller, Influence of the gas atmosphere during the synthesis of g-C_3N_4 for enhanced photocatalytic H_2 production from water on Au/g-C_3N_4 composites, *J. Mater. Chem. A. Mater.*, 2019, **7**, 14849.

46 S. Liu, J. Chen, D. Xu, X. Zhang and M. Shen, Enhanced photocatalytic activity of direct Z-scheme Bi_2O_3/g-C_3N_4 composites via facile one-step fabrication, *J. Mater. Res.*, 2018, **33**, 1391.

47 K. Manoharan and N. R. Krishna Chandar, Hydrothermal Synthesis and Characterization of Sulfur-doped g-C_3N_4/VS_4 nanocomposite for efficient photocatalytic applications, *Inorg. Chem. Commun.*, 2023, **155**, 111047.

48 H. Luo, T. Shan, J. Zhou, L. Huang, L. Chen, R. Sa, Y. Yamauchi, J. You, Y. Asakura, Z. Yuan and H. Xiao, Controlled synthesis of hollow carbon ring incorporated g-C_3N_4 tubes for boosting photocatalytic H_2O_2 production, *Appl. Catal. B.*,122933.

49 B. Zhu, P. Xia, W. Ho and J. Yu, Isoelectric point and adsorption activity of porous g-C_3N_4, *Appl. Surf. Sci.*, 2015, **344**, 188.

50 Q. Xu, B. Cheng, J. Yu and G. Liu, Making co-condensed amorphous carbon/g-C_3N_4 composites with improved visible-light photocatalytic H_2-production performance using Pt as cocatalyst, *Carbon*, 2017, **118**, 241.

51 M. Sierra, E. Borges, P. Esparza, J. Méndez-Ramos, J. Martín-Gil and P. Martín-Ramos, Photocatalytic activities of coke carbon/g-C_3N_4 and Bi metal/Bi mixed oxides/g-C_3N_4 nanohybrids for the degradation of pollutants in wastewater, *Sci. Technol. Adv. Mater.*, 2016, **17**, 659.

52 J. Liu, Y. Li, Z. Li, J. Ke, H. Xiao and Y. Hou, In situ growing of $Bi/Bi_2O_2CO_3$ on Bi_2WO_6 nanosheets for improved photocatalytic performance, *Catal. Today.*, 2018, **314**, 2.

53 S. H. Liu and W. T. Tang, Photodecomposition of ibuprofen over g-C_3N_4/Bi_2WO_6/rGO heterostructured composites under visible/solar light, *Sci. Total Environ.,* 2020, **731**, 139172.

54 Y. Wang, W. Jiang, W. Luo, X. Chen and Y. Zhu, Ultrathin nanosheets g-C_3N_4@Bi_2WO_6 core-shell structure via low temperature reassembled strategy to promote photocatalytic activity, *Appl. Catal. B.*, 2018, **237**, 633.

55 W. Xue, D. Huang, J. Li, G. Zeng, R. Deng, Y. Yang, S. Chen, Z. Li, X. Gong and B. Li, Assembly of AgI nanoparticles and ultrathin g-C_3N_4 nanosheets co decorated Bi_2WO_6 direct dual Z-scheme photocatalyst: An efficient, sustainable and heterogeneous catalyst with enhanced photocatalytic performance, Chem. Eng. J., 2019, **373**, 1144.

56 T. Wang, Y. Bai, W. Si, W. Mao, Y. Gao and S. Liu, Heterogeneous photo-Fenton system of novel ternary $Bi_2WO_6/BiFeO_3/g\text{-}C_3N_4$ heterojunctions for highly efficient degrading persistent organic pollutants in wastewater, *J. Photochem. Photobiol. A Chem.,*2021, **404**, 112856.

57 Y. Su, G. Tan, T. Liu, L. Lv, Y. Wang, X. Zhang, Z. Yue, H. Ren and A. Xia, Photocatalytic properties of $Bi_2WO_6/BiPO_4$ Z-scheme photocatalysts induced by double internal electric fields, *Appl. Surf. Sci.*, 2018, **457**, 104.

58 A. Kundu, S. Sharma and S. Basu, Modulated BiOCl nanoplates with porous $g\text{-}C_3N_4$ nanosheets for photocatalytic degradation of color/ colorless pollutants in natural sunlight*, J. Phys. Chem. Solids.,* 2021, **154**, 110064.

59 M. A. Barakat, R. Kumar and J. O. Eniola, Adsorption and photocatalytic scavenging of 2-chlorophenol using carbon nitride-titania nanotubes-based nanocomposite: Experimental data, kinetics and mechanism, *Data Brief*, 2021, **34**, 106664,

60 M. Chahkandi and M. Zargazi, New water based EPD thin $BiVO_4$ film: Effective photocatalytic degradation of Amoxicillin antibiotic, *J. Hazard Mater.*, 2020, **389**, 121850.

61 B. R. Shah and U. D. Patel, Mechanistic aspects of photocatalytic degradation of Lindane by TiO_2 in the presence of Oxalic acid and EDTA as hole-scavengers, *J. Environ. Chem. Eng.*, 2021, **9**, 105458.

62 E. Fathi, F. Derakhshanfard, P. Gharbani and Z. Ghazi Tabatabaei, Facile Synthesis of MgO/C_3N_4 Nanocomposite for Removal of Reactive Orange 16 Under Visible Light, *J. Inorg. Organomet. Polym. Mater.*, 2020, **30**, 2234.

63 T. Yildiz, H. C. Yatmaz and K. Öztürk, Anatase TiO_2 powder immobilized on reticulated Al_2O_3 ceramics as a photocatalyst for degradation of RO16 azo dye, *Ceram. Int.*, 2020, **46**, 8651.

64 B. Appavu, S. Thiripuranthagan and T. Sureshkumar, Novel band gap engineered $Bi_5Nb_3O_{15}$/N-rGO composite catalyst for photo degradation of reactive dyes, *Mater. Sci. Eng. B.,* 2020, **225**, 114472.

65 B. Simovic, Z. Radovanovic, G. Brankovic and A. Dapcevic, Hydrothermally synthesized CeO_2/ZnO nanocomposite photocatalysts for the enhanced degradation of Reactive Orange 16 dye, *Mater. Sci. Semicond. Process.*, 2023, **162**, 107542.

66 A. Brindha and T. Sivakumar, Visible active N, S co-doped TiO_2/graphene photocatalysts for the degradation of hazardous dyes, *J. Photochem. Photobiol. A. Chem.*, 2017, **340**, 146.

CHAPTER-4

CHAPTER-4

Bi-doped g-C_3N_4/Bi_2MoO_6 ternary nanocomposite for the effective photodegradation of Ofloxacin under visible light irradiation.

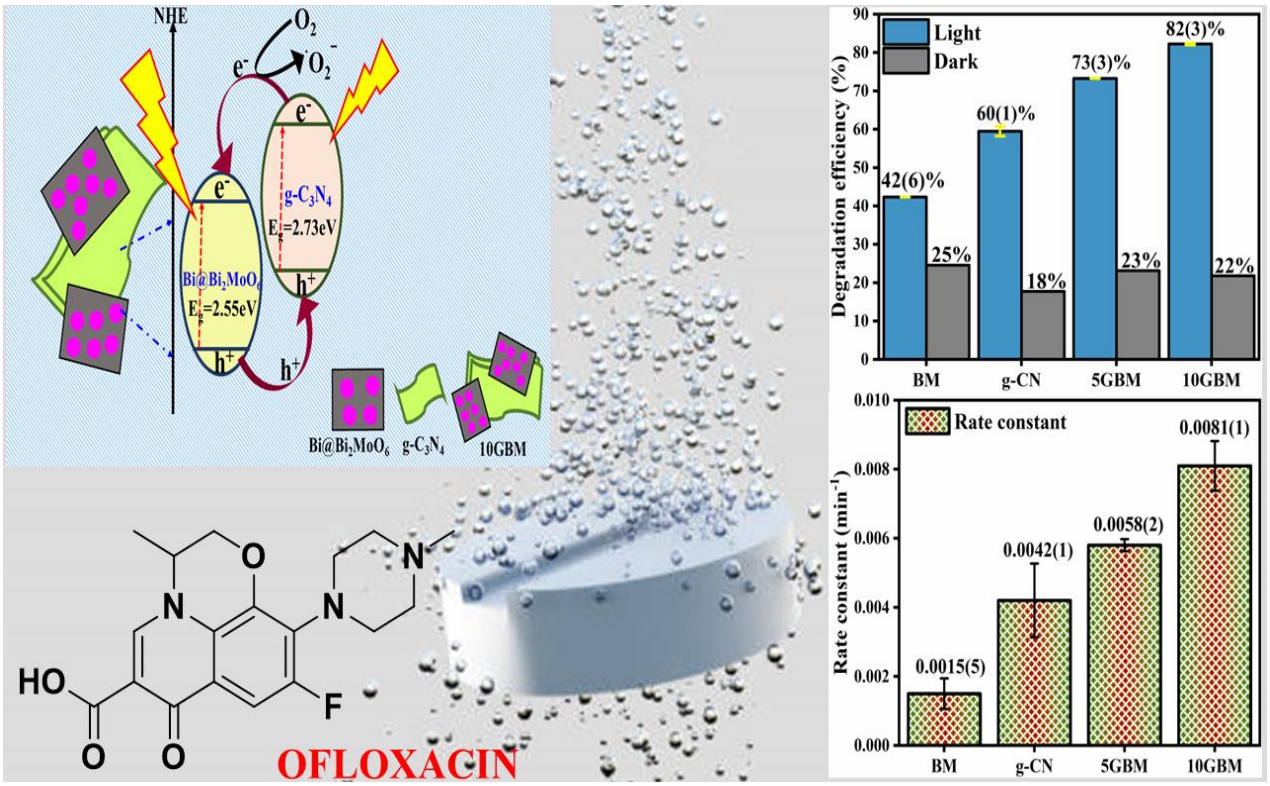

Schematic outline:

Bi (0)-doped g-C_3N_4/Bi_2MoO_6 [g-C_3N_4/Bi@Bi_2MoO_6] ternary nanocomposite was prepared using the wet impregnation method. Surprisingly, the zerovalent Bi is generated simultaneously during the hydrothermal synthesis of Bi_2MoO_6 without using any additional reducing agent. The photocatalyst is highly stable and having suitable band gap of 2.40 eV lying in visible region. The presence of Bi is confirmed by XPS, HRTEM and DRS. HRMS was used to identify various fragments which support the proposed mechanism. Due to the stability, easy preparation method and recyclability the photocatalyst worked superior for the degradation of pollutants.

4.1 Introduction:

The discharge of effluent containing organic pollutants and toxins into the environment has significant risks to the biosphere and serious health threats to humans[1]. Among these pollutants, antibiotics-commonly used to treat bacterial infections[2].

Among the antibiotics, Ofloxacin is a frequently used fluoroquinolone-based drug found in surface water at up to 31.7 µg/L concentrations. Even at very low concentrations, ofloxacin might have a detrimental effect on ecological systems by preventing the growth of microorganisms and producing other ecotoxicological effects[3–7]. Hence, it is crucial to remove these pollutants from wastewater[8,9]. Many methods have been developed so far, including nano-filtration, coagulation, ion exchange, photocatalysis, adsorption, etc. One of the most appealing methods for treating wastewater is photocatalysis as it causes the contaminants to entirely break down rather than merely shifting from one medium to another[10]. In recent years, semiconductor catalysed photocatalytic degradation of organic contaminants has grown significantly by consuming solar light energy due to increasing environmental concerns[11–14].

Bi_2MoO_6, an Aurivillius oxide, exhibits interesting physicochemical properties, such as a band gap of nearly 2.7 eV. This unique semiconductor reveals excellent performance under visible light irradiation. Its structure includes $[MoO_4]^{-2}$ alternate sheets with $[Bi_2O_2]^{+2}$ layers, distinguishing it from other bismuth-based materials[15]. However, because of the low separation efficiency of the photoexcited charge carriers, Bi_2MoO_6 is insufficiently efficient to meet the requirements of the application [16]. This drawback can be fixed by using various approaches like porosity engineering, elemental doping, semiconductor modification by creating heterojunction structures, etc [17]. Because of its high stability and low cost, g-C_3N_4 is a promising material for making semiconductor heterojunctions. Other aids include strong physicochemical stability, a 2.7 eV band gap, non-toxicity, and a large surface area[10].

Furthermore, photocatalytic activity is increased by loading various plasmonic metals due to their localised surface plasmon resonance (LSPR) properties, which help to separate charge carriers and excite electron-hole pairs[18]. Bismuth (Bi), a non-noble metal, exhibits a significant LSPR effect along with plasmonic metals (Cu, Ag, Au). One benefit of bismuth over noble metals is its affordable price. This study includes the fabrication of a Bi-doped g-C_3N_4/Bi_2MoO_6 ternary composite and examines its photoactivity for the degradation of Ofloxacin. To fabricate Bi-doped Bi_2MoO_6, a hydrothermal method was adopted in which methanol was used as a solvent. Remarkably, Bi (+3) does not need any extra step for the reduction process as methanol itself works as a reducing agent here, reducing Bi (+3) in situ during hydrothermal reaction. The wet impregnation method was used for the successful loading of g-C_3N_4. The presence of Bi (0) and g-C_3N_4 can increase the light sensitivity and decrease the charge

carriers (e^- and h^+) recombination. Such characteristics can be beneficial to enhance the photocatalytic activity.

4.2 Experimental:

4.2.1 Chemicals

Chemical reagents: [Bi $(NO_3)_3$.$5H_2O$] 98 %, Sodium molybdate dihydrate 99 % [Na_2MoO_4 .$2H_2O$], Urea extra pure 99 %, Methanol 99.5 % extra pure and N-methyl-2-pyrrolidone (NMP) were obtained from Loba Chemie, India. Changshu Hongsheng Fine Chemicals Co. Ltd. has provided the absolute 99.9% ethanol. Antibiotic Ofloxacin (200 mg) was purchased from Cipla Pharmaceutical, and DI (distilled water) was produced using the Milli-Q Millipore system. The fluorinated tin oxide (FTO) coated glasses were bought from Vritra Technologies (resistance < 10 Ω). Carbon black powder (CB) and polyvinylidene fluoride (PVDF) were purchased from Nanoshell and Sigma Aldrich, respectively.

4.2.2 Preparation of Bi@Bi_2MoO_6

Solvothermal method was used to synthesis Bi@Bi_2MoO_6, 0.25 M of $Na_2MoO_4 \cdot 2H_2O$ and bismuth nitrate pentahydrate (0.5 M) were mixed in 35 mL of distilled water and 35 mL of methanol respectively and stirred for 2 h. The above mixture was kept in an autoclave of 100 mL at 180 ℃ for 24 h[19] , then centrifuged and dried at 70 ℃ and will be denoted as **BM** in this manuscript.

4.2.3 Synthesis of g-C_3N_4

To synthesis g-C_3N_4 sheets using urea as a raw material was prepared by pyrolysis followed by the ultrasonication method. 30 g urea in a crucible was heated at 5 ℃/min at 500 ℃ for 2 h then again to 550 ℃ at 10 ℃/min for another 2 h. After cooling down naturally, the pale yellow-coloured powder was ground into bulk g-C_3N_4. The obtained product was dispersed in ethanol for 1 h using ultrasonication to attain g-C_3N_4 sheets, then the solution was filtered and dried at 50 ℃. It will be abbreviated as g-CN in the entire manuscript[20].

4.2.4 Synthesis of g-CN loaded BM nanocomposite

The g-C_3N_4/Bi@Bi_2MoO_6 composite was prepared via the wet impregnation method 21. For the preparation, 100 mg of Bi_2MoO_6 was mixed with the desired quantity of g-C_3N_4 in 1:1 (ethanol and DI water). The solution was kept at stirring for 24 h. Then the product was centrifugated and dehydrated at 50 ℃[20]. Throughout the manuscript, the 5 and 10 wt.% g-C_3N_4 loaded Bi@Bi_2MoO_6 composite will be represented as 5GBM and 10GBM respectively.

4.2.5 Preparation of thin films

The drop-casting method was used to prepare the working electrode for EIS measurement (Nyquist plot). 1 mg PVDF and 50 µL NMP were ground together to form a homogenous paste. Then 1-2 mg carbon black (CB) was added and mixed for an extra 15 min. After that, active material (8 mg) was added to attain a slurry, then it was drop-casted and spread onto the FTO-layered glass and dehydrated for 12 h at 60 ℃.

4.2.6 Photocatalytic activity evaluation

The photocatalytic activity of the synthesised BM and its composite 5GBM and 10GBM were examined using the hazardous pollutant Ofloxacin. In a model experiment, an optimized amount (5 mg) of the as-prepared composite was added to a test tube containing 5 mL of Ofloxacin solution at a concentration of 20 ppm. To acquire the adsorption-desorption equilibrium, the mixture was stirred for half an hour in the absence of light. Then, for predefined periods, the reaction mixture was exposed to visible light (Wipro Garnet B22-50 W LED having a wavelength of more than 360 nm and light intensity of 5000 lumens). By centrifugation, the catalyst was extracted, and then the concentration of the pollutant was scrutinized using a UV-Vis spectrophotometer. The percentage degradation efficiency was evaluated using the Eq. no. (1):

$$\text{Degradation efficiency (\%)} = \frac{C_0 - C_t}{C_0} \times 100\% \qquad (1)$$

Where C_0 is the initial concentration and C_t is the concentration at time "t".

4.2.7 Characterization technique

To record the crystallographic properties, X-ray diffraction (XRD) was examined by employing a diffractometer of Xpert pro-Cu-Kα (1.54 Å) at 45 kV having a diffraction angle (2θ, 10°-75°). The structural morphology was studied using high-resolution transmission electron microscopy (HRTEM) (JEOL JEM 2100 plus) and field-emission scanning electron microscopy (FESEM) (500 FEG-SEM, Carl-Zeiss Sigma). The energy dispersive spectroscopy (EDS) was examined using BRUKER. JASCO V-750 Spectrophotometer was used to measure the DRS (diffused reflectance spectroscopic) of the synthesized samples. The oxidation state was determined using (XPS, Omicron ESCA, Oxford Instrument Germany). The Microtrac Belsorp Mini-II (Bel, Japan, Inc.) was utilized to govern the surface area. The FTIR Spectra were obtained by IR Tracer-100 (Shimadzu). The fragments were studied by High-resolution mass spectrometry (HRMS) using a Waters mass spectrometer (QTOF) with UPLC (XEVO G2 XS) and Ion source Combined APCI and both positive and negative ESI mode

to identify the fragments. EIS tests were conducted in the dark using a Biologic (potentiostat, VSP300 at 10 mV, with a 0.1 Hz–1 MHz frequency range). The three-electrode system comprised a Pt counter electrode, a BM/10GBM-loaded FTO working electrode, and a standard Ag/AgCl reference electrode in 0.5 M Na_2SO_4 solution. Chemical oxygen demand was measured using Hach COD digestor DRB200, open reflux method followed by APHA 4200 (21edition).

4.3 Results and discussion:

4.3.1 XRD studies

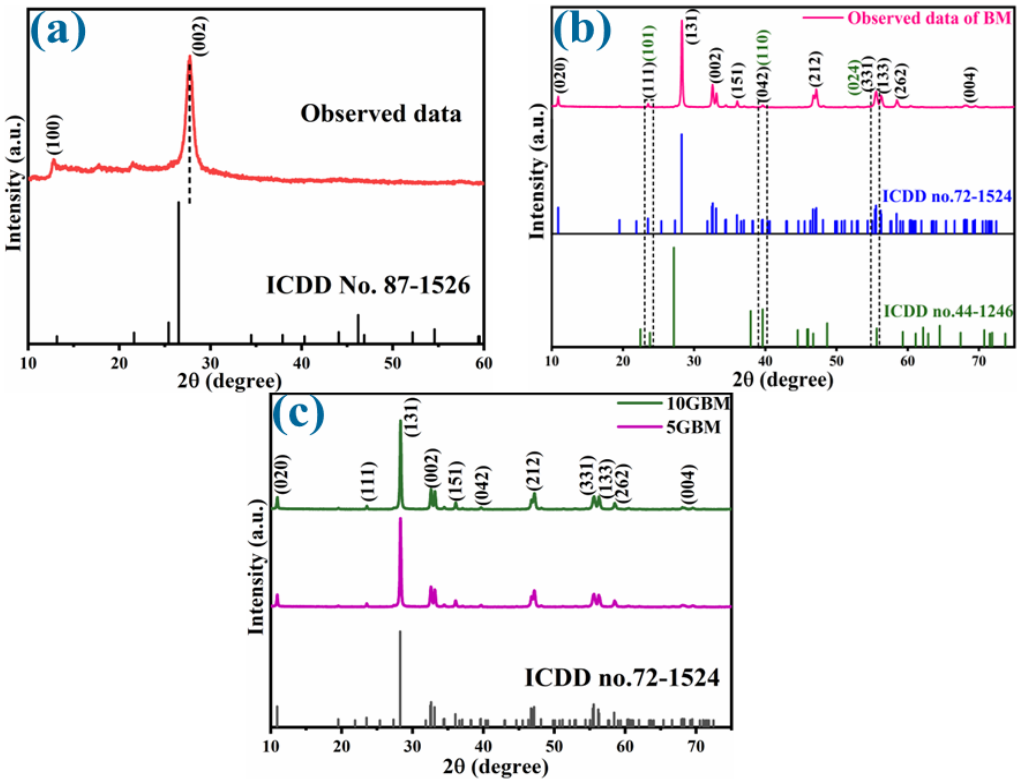

Fig. 4.1: Diffraction pattern for (a) g-CN (b) pure BM, and (c) as synthesised composites 5GBM and 10GBM.

The diffraction studies were recorded to analyse the crystallinity and phase purity of the material **(Fig. 4.1)**. The pattern of g-CN closely matches with the ICDD NO. 87-1526 **(Fig. 4.1a)**[10]. A strong peak at 27.5° corresponds to (002) and another peak at 12.7° (100). The minor peak shift of (002) corresponds to the change in interplanar distance between the graphitic nitride sheets [22]. Moreover, two extra peaks between the range 15° and 25° are due to the layered structure of g-CN. The peaks at 10.8°, 23.4°, 28.2°, 32.5°, 36.0°, 39.5°, 47.1°, 55.4°, 56.3°, 58.4° and 68.2° associated with (020), (111), (131), (002), (151), (042), (212), (331), (133), (262) and (004) planes respectively, which justified with the ICDD NO. 72-1524 **(Fig. 4.1b)** of the orthorhombic crystal phase of Bi_2MoO_6 [19]. Additionally, peaks with respect to (101), (110), and (024) planes are observed at 23.4°, 39.5°, and 55.4°, respectively,

corresponding to the structure of Bi_2MoO_6 indicating the presence of Bi metal at Bi_2MoO_6, confirmed with the ICDD No. 44-1246 [16]. Moreover, the XRD of synthesized composites 5GBM and 10GBM **(Fig. 4.1c)** is almost similar to the bare BM, implying that by introducing g-CN, the structural integrity of the BM is not disrupted. Because of the small amount of loading and lower X-ray scattering coefficient of g-CN than pristine BM, there is no g-CN peaks in the composite [10,21].

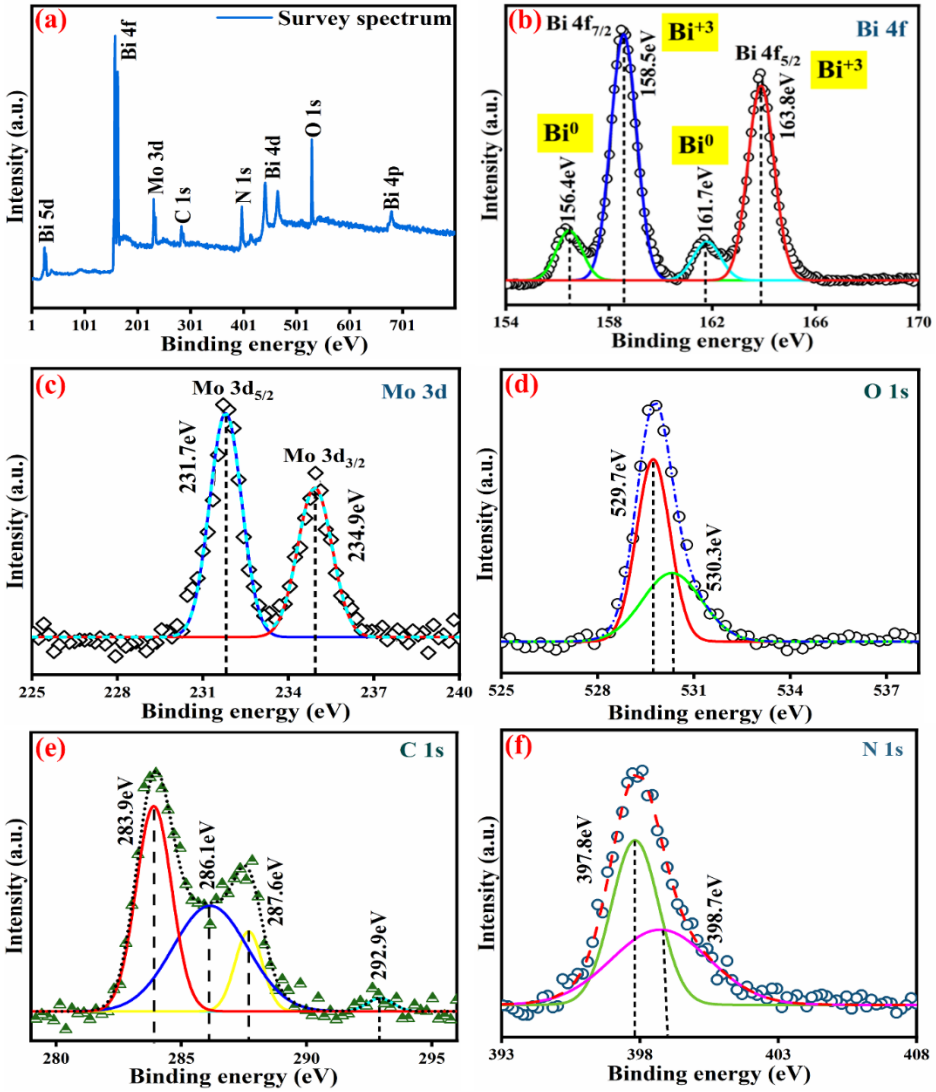

Fig. 4.2: XPS graphs representing (a) survey diagram (b) Bi [4f] (c) Mo [3d] (d) O [1s] (e) C [1s] and (f) N [1s] of the 10GBM nanocomposite.

4.3.2 XPS studies

The chemical composition of the 10GBM composite has been determined using XPS analysis as shown in **Fig. 4.2**. The 4f signals of Bi in Bi_2MoO_6 **(Fig. 4.2b)** at 158.5 eV (Bi $4f_{7/2}$) and 163.8 eV (Bi $4f_{5/2}$) is attributed to trivalent bismuth [Bi (III)]. Additionally, two other peaks at 156.4 eV and 161.7 eV are referred to as zerovalent Bi which validates that methanol reduces Bi (+3) to zerovalent Bi [10]. Mo (+5)

3d (**Fig. 2c**) deconvolutes into two peaks, at 231.7 eV and 234.9 eV relative to Mo $3d_{5/2}$ and Mo $3d_{3/2}$, respectively [23,24]. Typically for O 1s **(Fig. 4.2d)**, lattice oxygen in the crystal structure is assigned to 529.7 eV and 530.3 eV attributed to oxygen vacancies [25]. The XPS spectra of C1s showed four peaks that corresponded to binding energies of 283.9 eV, 286.1 eV, 287.6 eV, and 292.9 eV **(Fig. 4.2e)** due to extraneous carbon in the surface, N−C=N bonds, sp^2 hybridised carbon of $(N)_2$−C=N heterocyclic ring and C−NH_2 respectively [10,26,27]. The signals observed at 397.8 eV and 398.7 eV attributed to sp^2 nitrogen of triazine rings corresponding to C−N=C and bridged nitrogen atom N−$(C)_3$ respectively **(Fig. 4.2f)** [28].

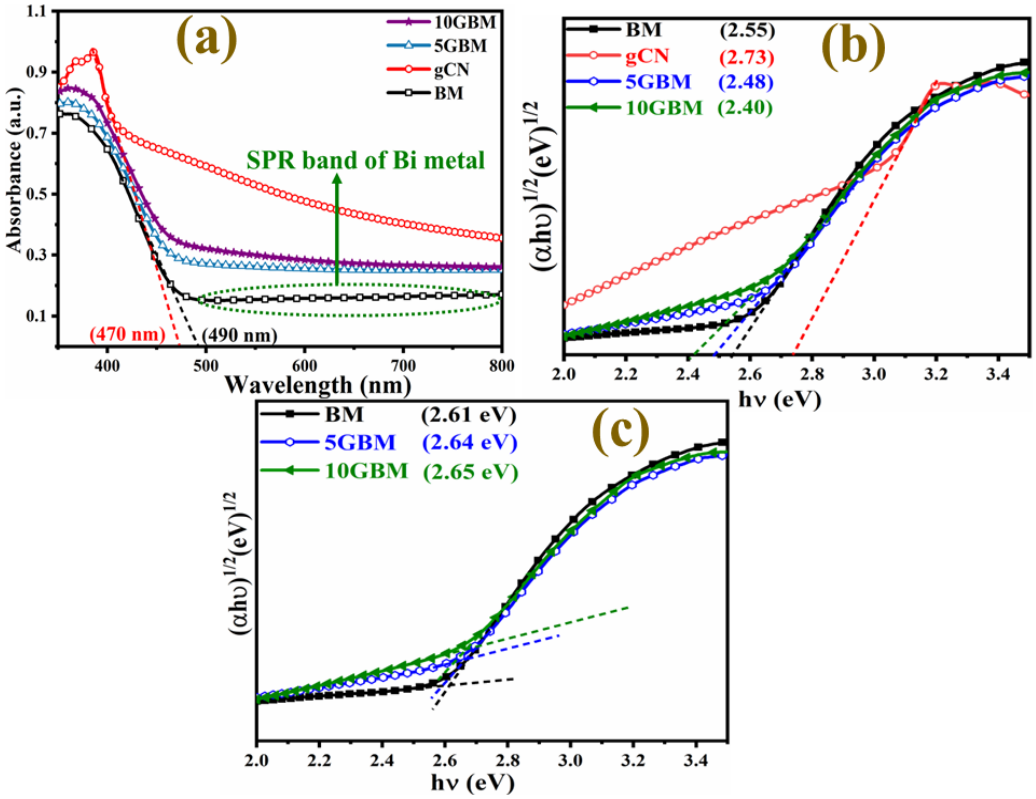

Fig. 4.3: (a) DRS of BM, g-CN, and all synthesised nanocomposites (b) Band gap values and (c) Band gap values at absorption edge using Tauc's plot.

4.3.3 Optical studies

Optical studies were examined to determine the bandgap of BM and the synthesised nanocomposites. The Bi_2MoO_6 and g-CN have an absorption edge value **(Fig. 4.3a)** of 490 nm and 470 nm respectively [29,30]. A broad absorption band at 500–800 nm in the UV-Vis DRS spectra of BM is referred to as the LSPR effect shown by Bi (0)[31]. Tauc's plot **(Fig. 4.3b-c)** indicates that the band gap of BM is 2.55 eV, significantly less than the reported value[19]. This is probably because plasmonic Bi is present in the Bi_2MoO_6 lattice. As g-CN loading increases, the composites' bandgap reduces to 2.40 eV from 2.55 eV, revealing improved absorption of visible light. In contrast, the band gap values at the absorption edge remain practically similar for BM, 5GBM, and 10GBM as shown in **Fig. 4.3c**. Such observation

is quite similar to the result reported previously[12] and reveals that the loading of g-CN over BM enhances the light sensitivity of the prepared composites.

The PL (photoluminescence) experiments' results are indeterminate because the bare BM showed non-fluorescent behaviour.

4.3.4 FTIR analysis

The synthesised materials were further verified by FTIR analysis. All the nanocomposites 5GBM and 10GBM show peaks of both the bare BM and g-CN **(Fig. 4.4).** Several peaks in the region 1100- 1700 cm^{-1} are attributed to the C−N heterocycle. The broad band between 3000-3400 cm^{-1} is due to the N−H and O−H groups of g-CN. At 810 cm^{-1}, the out-of-plane bending mode of the heptazine unit was detected.

The bands between 400-900 cm^{-1} are because of the stretching mode of Bi−O, Mo−O, and the bridging mode of Mo−O−Mo. At 790 cm^{-1}, MoO_6 octahedron asymmetric mode was observed[32].

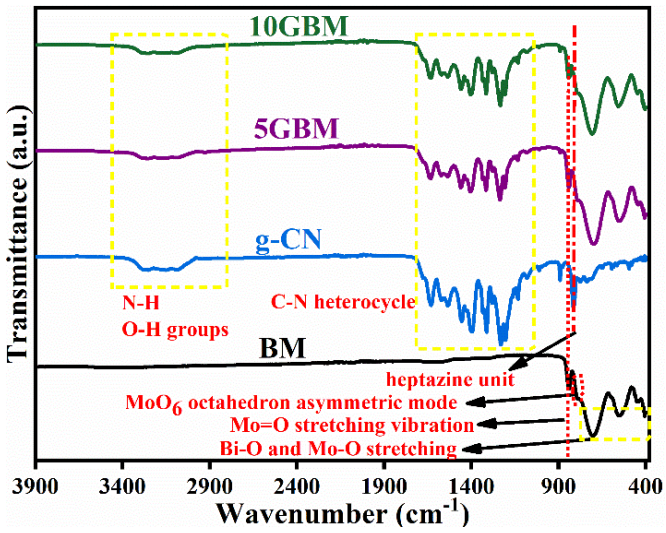

Fig. 4.4: The FTIR spectra of pristine BM, g-CN and all composites.

4.3.5 EIS analysis

The EIS analysis was carried out to understand the transfer efficiency of photogenerated charge carriers[33]. The experiment was conducted in the dark for g-CN as well as bare BM and 10GBM composite **(Fig. 4.5)**. The g-CN has an extremely small charge transfer resistance due to its high conductivity. As a result, the charge transfer resistance[34] of 10GBM composites becomes smaller compared to bare BM as the composite possesses smaller radii in the Nyquist plot compared to its pristine analog, as represented in **Fig. 4.5(b)**[35]. This indicates that incorporating g-CN helps the

electron migration from BM to the g-CN surface. Hence, the composites can serve as more proficient photocatalysts than pristine BM.

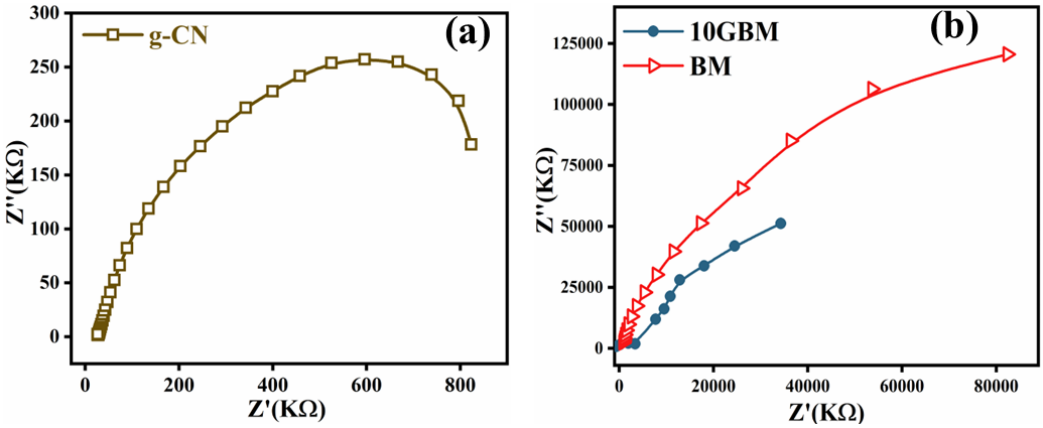

Fig. 4.5: Nyquist plots of (a) g-CN and (b) bare BM and 10GBM composite.

4.3.6 Morphology and Multielemental analysis

The morphology of bare BM and its 10GBM ternary composite were studied using FESEM shown in **Fig. 4.6**. Remarkably, the pristine Bi_2MoO_6 depicts an irregular crystals-like structure **(Fig. 4.6a-b)** [36]. The presence of both the CN layers and Bi_2MoO_6 irregular crystals is shown in **Fig. 4.6c-d** confirming the development of 10GBM nanocomposite. The elemental mapping (EDS) of the bare BM and nanocomposite 10GBM exhibits every component (Mo, O, Bi, C, and N) elements were uniformly dispersed across the entire surface **(Fig. 4.7 and 4.8).**

HRTEM analysis **(Fig. 4.9)** was conducted to further examine morphology and crystallinity. The heterostructure consists of g-CN, a sheet-like structure of g-CN, and irregular, disorganized particles of Bi_2MoO_6 **(Fig. 4.9a)**[37]. In **Fig. 4.9b**, the loading of g-CN over Bi_2MoO_6 is confirmed. The lighter sheet-like structure corresponds to g-CN while the darker square shape is of BM. Moreover, spherical Bi (0) particle deposition on the BMO surface was also detected in **Fig. 4.9c-d**. Additionally, the fringes of BMO and Bi-metal (**Fig. 9e-f**) were also represented which are well matched with the (151) and (101) planes, respectively. The selected area diffraction pattern in **Fig. 4.9g** exhibits the spots that are respective to (002), (131) and (202), (024) planes of BMO and Bi-metal, respectively. The observations validate the crystallinity and formation of 10GBM ternary composite.

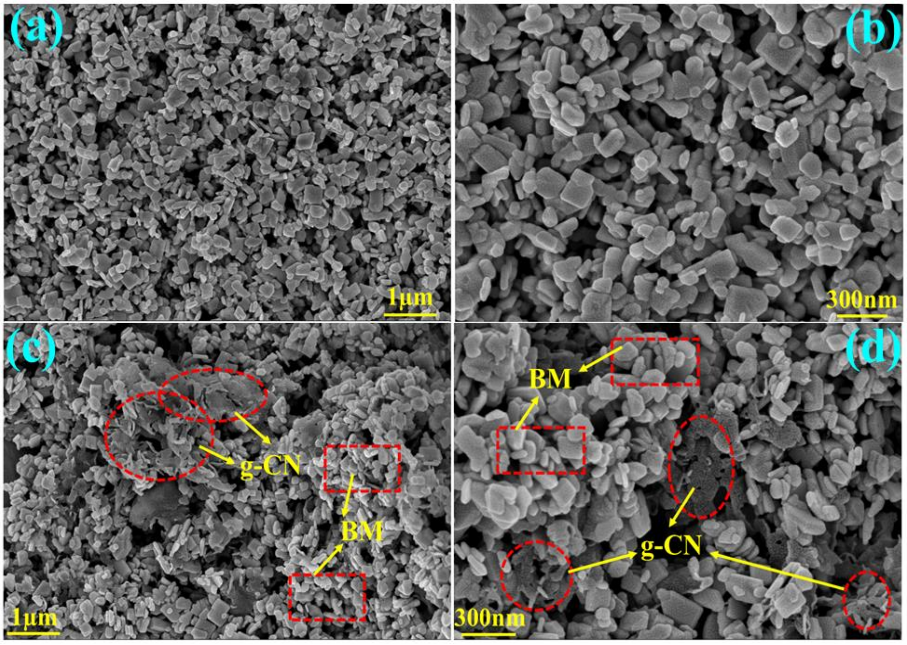

Fig. 4.6: FESEM images of pristine BM (a, b) and 10GBM nanocomposite (c, d).

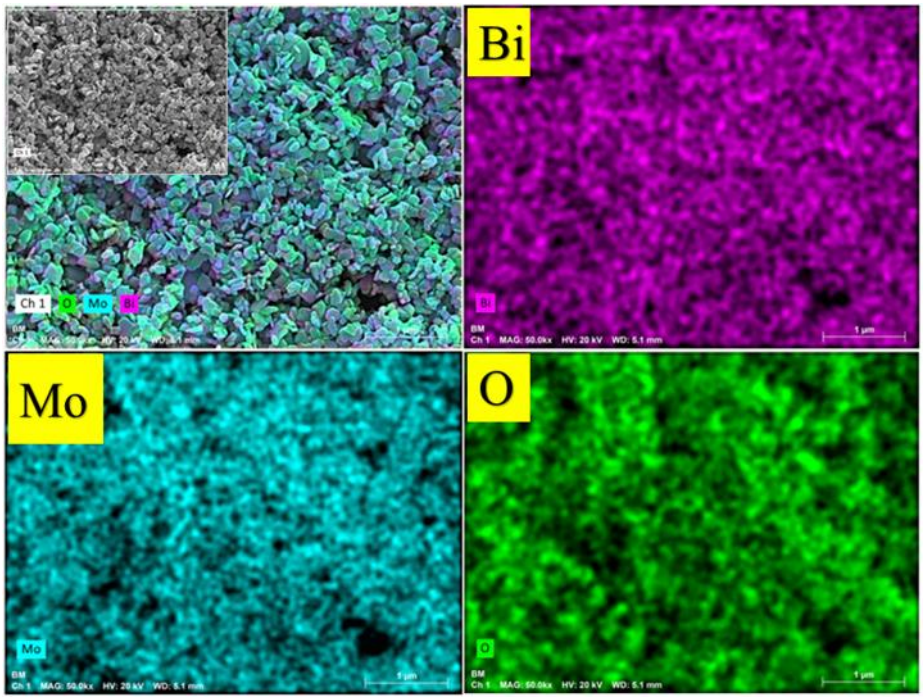

. **Fig. 4.7: EDS mapping of pristine BM containing elements Bi, Mo and O.**

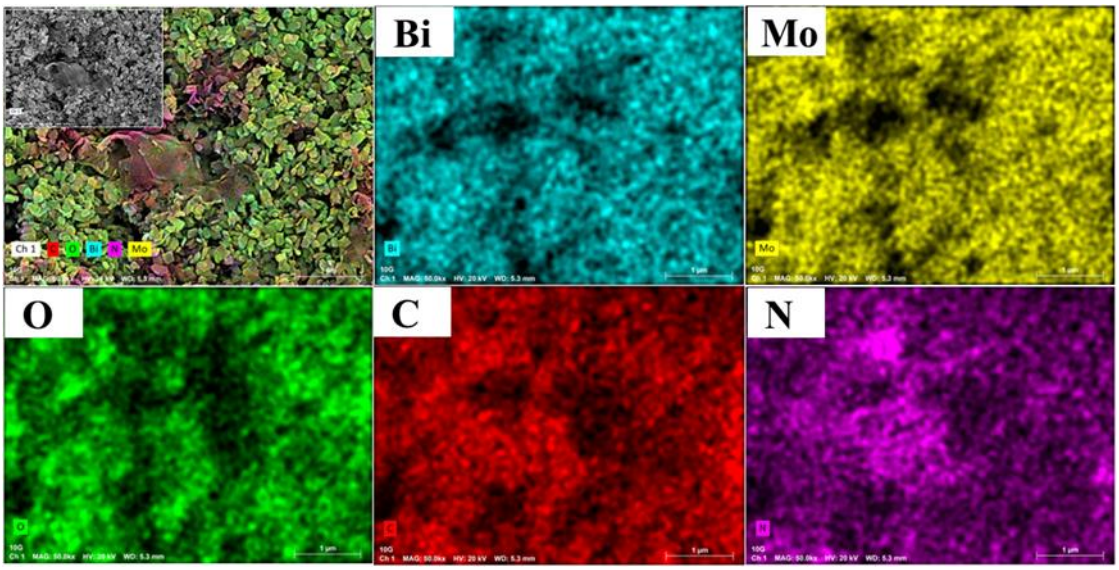

Fig. 4.8: EDS mapping of ternary nanocomposite 10GBM having all the elements Bi, Mo, O, C and N.

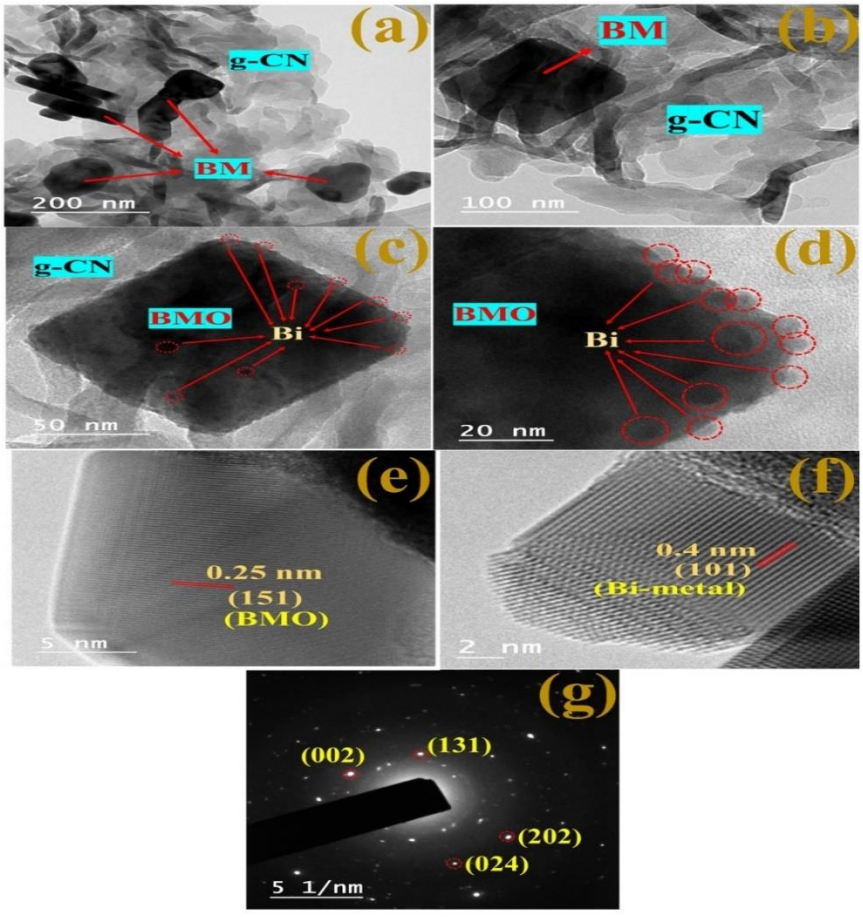

Fig. 4.9: (a, b) HRTEM micrograph of g-CN and BM, (c and d) showing Bi-metal over BMO and (e, f) lattice fringes (g) Selected area diffraction pattern of the synthesised 10GBM ternary nanocomposite.

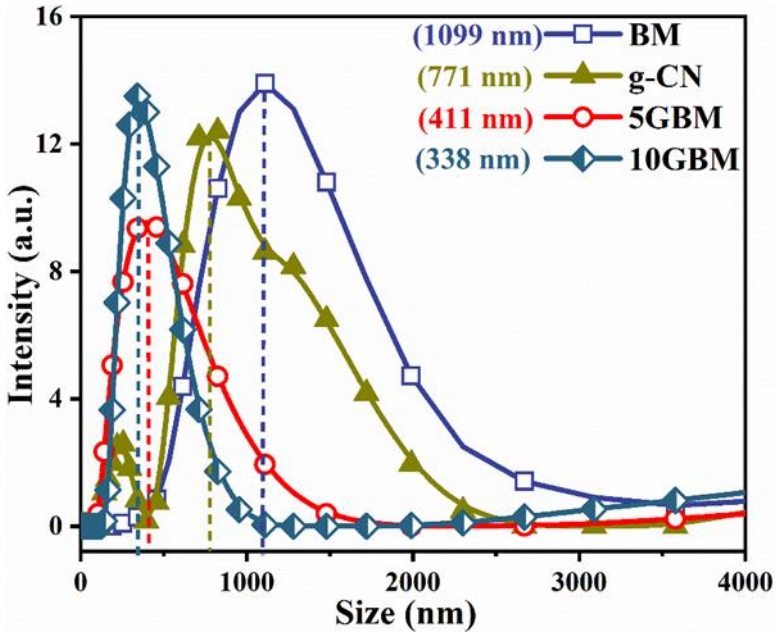

Fig. 4.10: The hydrodynamic size of photocatalyst and their composites.

The hydrodynamic particle size of the synthesised catalyst is measured using the DLS technique. The particle size of bare BM and g-CN was observed to be 1099 and 771 nm respectively. As the loading of g-CN increases, the size decreases to 411 nm and 338 nm for 5GBM and 10GBM respectively **(Fig. 4.10)** which is due to more hydrophobicity around the catalyst which reduces the hydrodynamic particle size

4.3.7 N_2 sorption analysis

BET sorption isotherms in **Fig. 4.11** were determined for pristine BM and the 10GBM heterostructure to explain the difference in surface properties after g-CN loading. The prepared samples exhibit an H3 hysteresis loop and type-III sorption isotherm[38]. This indicates the weak adsorbate-adsorbent interaction and implies the occurrence of small pores. Among the two, the 10GBM composite possesses almost double the surface area compared to bare BM due to the incorporation of g-CN which augments the total active sites and resultantly increases the surface area. The total pore volume of bare BM and 10GBM is 1.67×10^{-2} cm^3/g and 3.44×10^{-2} cm^3/g whereas the pore diameter is 10.07 nm and 10GBM is 11.33 nm, respectively. Such observation suggests that the 10GBM heterostructure is also having higher porosity compared to BM. As a result, 10GBM can act as a superior photocatalyst.

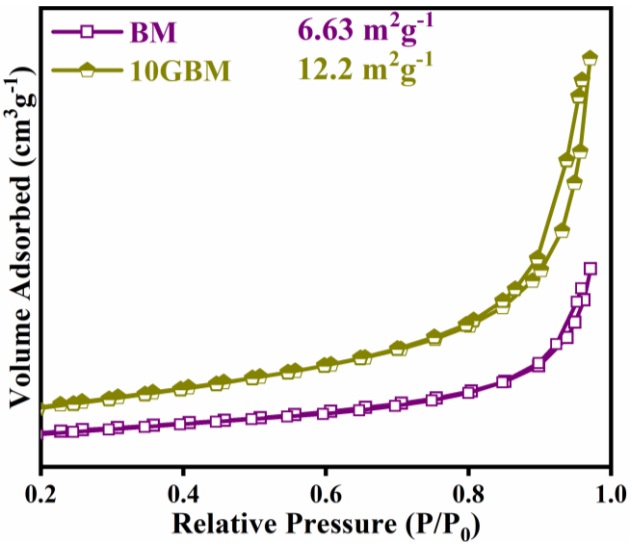

Fig. 4.11: BET analysis of pristine BM and 10GBM ternary composite.

4.3.8 Photocatalytic activity

The photocatalytic performance of bare BM, g-C_3N_4, and synthesised composites (5GBM and 10GBM) were examined using visible light **(Fig. 4.12** and **4.13).** Before irradiating the visible light, the reaction mixture was vigorously stirred in the dark for half an hour to attain the adsorption-desorption equilibrium. The bare BM and g-CN exhibit lower photocatalytic degradation activity in **Fig. 4.12a-b** while in the case of ternary nanocomposite (5GBM and 10GBM), upon loading of g-CN on BM photocatalytic activity gradually increases as ~72(3) % and ~82(3) % respectively after 3 h **(Fig. 4.12 a, b, and d).** The photodegradation process followed the pseudo-first-order kinetics as depicted in the following Eq. (2)[21]

$$ln\frac{C}{C_0} = -kt \qquad (2)$$

where C_0 = initial concentration, C = concentration at the time 't' and 'k' = rate constant for pseudo-first-order kinetics.

Substantially, a reaction rate enhances on loading of g-CN and the hybrid nanocomposite 10GBM has the maximum rate constant value 0.0081(1) min^{-1} (**Fig. 4.12c**).

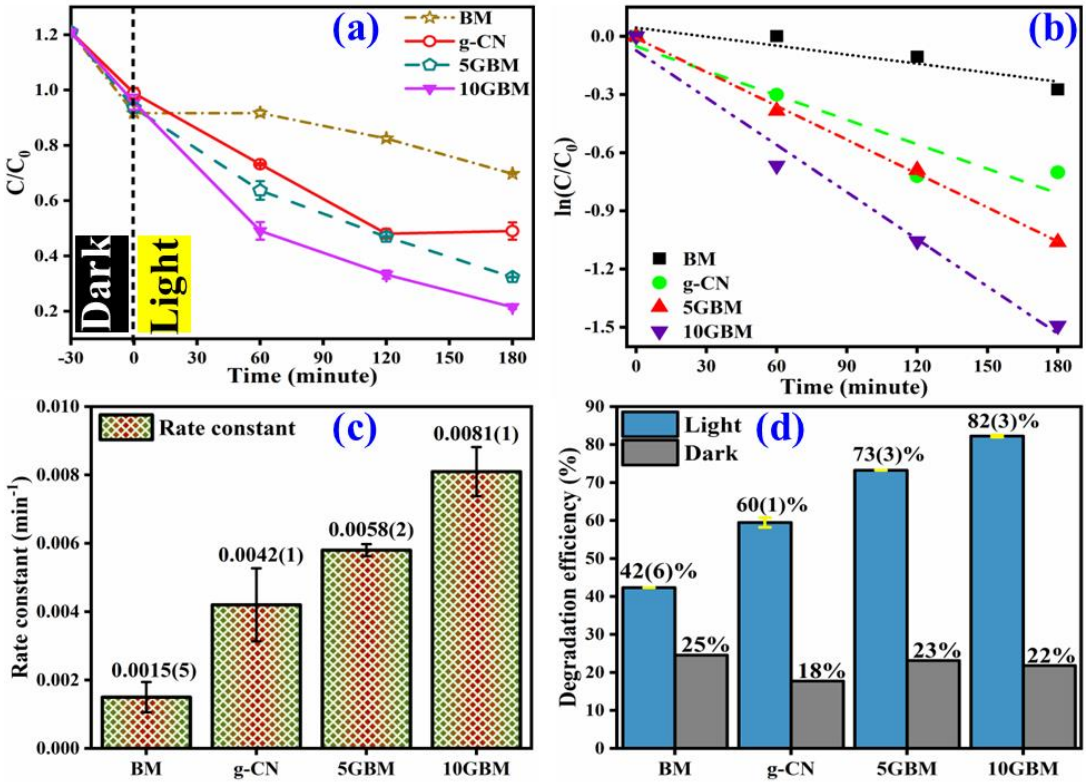

Fig. 4.12: Photocatalytic deterioration of Ofloxacin with time 't' (a), displaying pattern with ln C/C_0 at different time period of pristine BM, g-CN and hybrid composites 5GBM and 10GBM (b), rate constant values (c) and bar plot of degradation efficiency in a dark and light environment of all the samples (d)

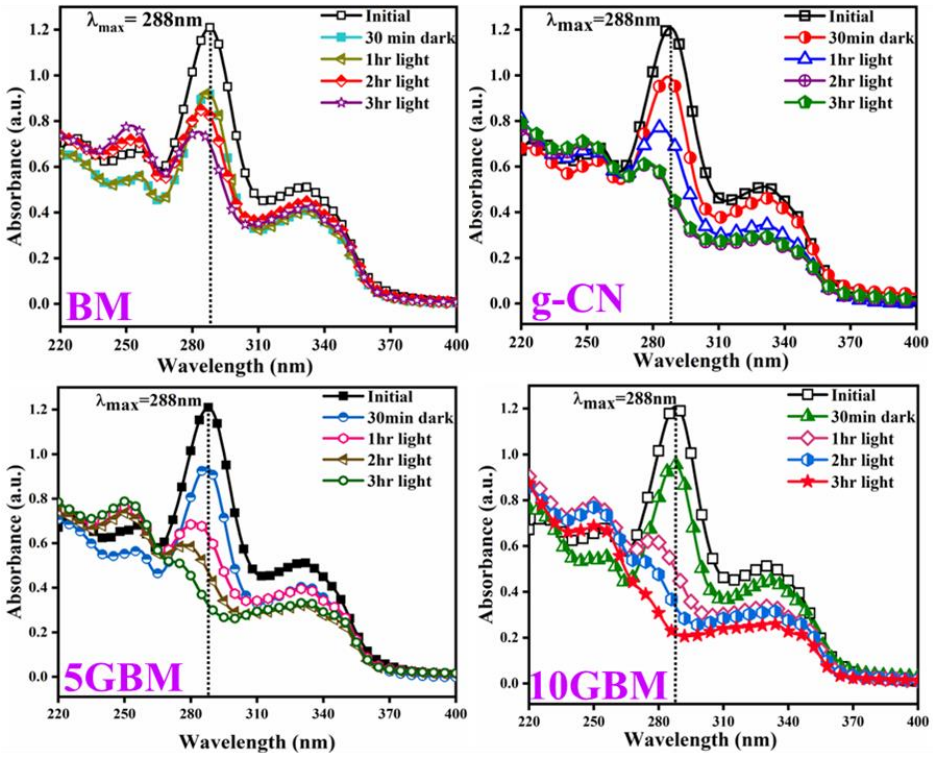

Fig. 4.13: UV-Vis spectra at different time of pristine BM, g-CN and different wt.% loaded composites.

To achieve the optimized condition, the effect of reaction time, catalyst amount, and different wt.% loading of g-CN was scrutinized **(Fig. 4.14).** It was observed in **Fig. 4.14a** that on increasing reaction time, the degradation efficiency enhances considerably till 3 h, but after that, no such improvement in the efficiency was observed. It has also been noted **(Fig. 4.14b)** that when the catalyst amount increases from 2.5 mg to 5 mg, the degradation efficiency significantly enhances from 47% to 82% due to the greater counts of active sites but with a further increase in the amount, the degradation efficiency remains practically same. Further, evaluated the different wt.% loading of g-CN over BM, and it was found that the maximum degradation efficiency was achieved through 10GBM **(Fig. 4.14c),** increasing the loading of g-CN above the optimal condition would result in no substantial improvement.

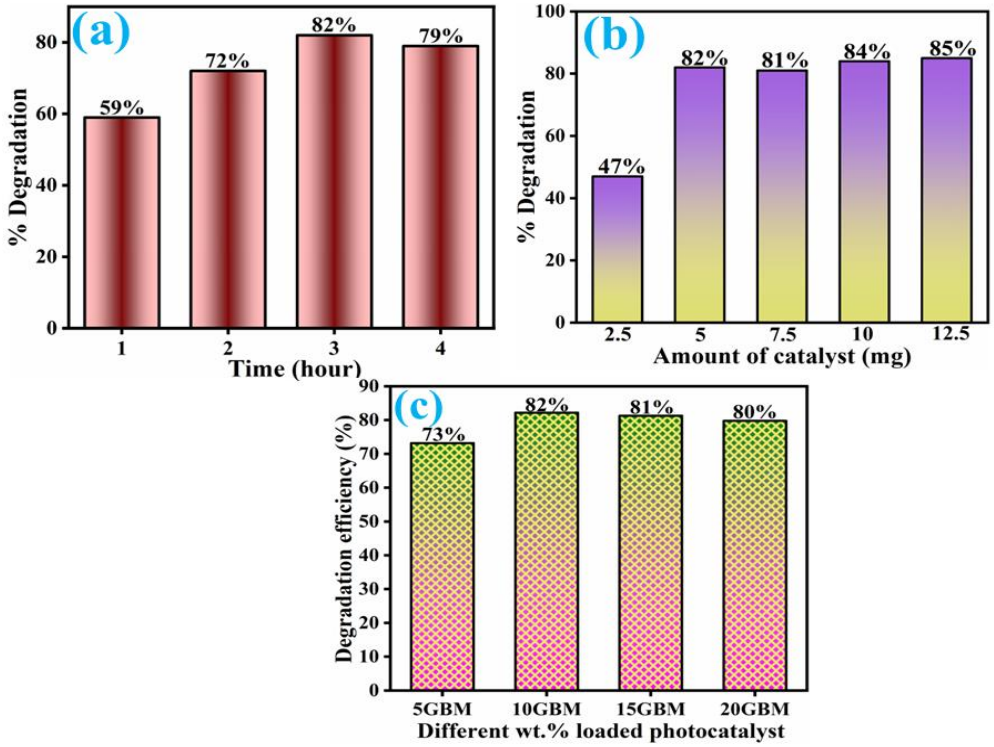

Fig. 4.14: Optimization of reaction time (a), catalyst dosage (b) and loading of g-CN over BM (c) towards the degradation of ofloxacin.

The degree of mineralization was also evaluated along with the degradation studies. Therefore, COD measurements were carried out to study the demineralization of the organic matter [39] using the 10GBM composite. The demineralisation efficiency (DE) was evaluated from the following Eq. 3

$$DE = \frac{COD_i - COD_f}{COD_i} \times 100 \qquad (3)$$

The COD of the reaction mixture was decreased from 164 mg/L to 35.4 mg/L, which is attributed to ~78.4 % demineralization efficiency, which is very close to degradation efficiency, suggesting almost complete degradation of a pollutant without the presence of any residual intermediate.

4.3.9 Mechanistic study

4.3.9.1 Proposed mechanism

A heterojunction structure of type II **(Fig. 4.15)**[21,40,41] was constructed on the formation of electron-hole pairs produced by excitation via a band gap to study the proposed reaction mechanism. The following equation calculates the band energy values of BM and g-CN to validate the mechanism [42]

$E_{CB} = E_{VB} - E_g$,

$E_{VB} = X\text{-}E_e + 0.5E_g$

E_{VB} = Energy of the valence band

E_{CB} = Energy of the conduction band

X= Electronegativity of free electron

E_e = Energy of free electron

E_g = Band gap energy

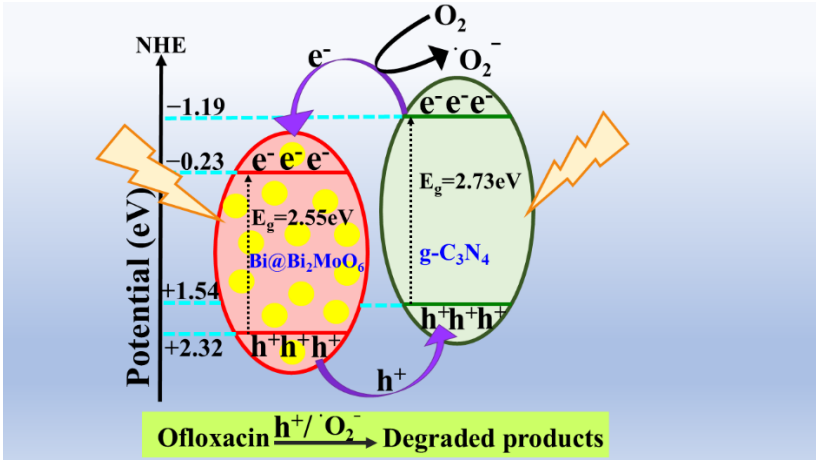

Fig. 4.15: Representation of the proposed mechanism of type-II heterojunction structure formed by 10GBM photocatalyst.

The values of CB and VB of BM and g-CN are -0.23 eV and +2.32 eV [43] and -1.19 eV and +1.54 eV [44] respectively. Now, in the 10GBM, the primary reaction occurs in the presence of light irradiation when it falls on the semiconductor. Then the charge carriers (e^- and h^+) will generate, and electrons (e^-) will excite to the CB from the VB and concurrently leave behind the holes (h^+) in the VB. Therefore, for the photocatalytic reaction to occur lower redox potential is required so according to the respective (type-II) mechanism, the electrons that are excited to the conduction band of g-CN migrating to the conduction of BM and holes that correspond to the valence band of BM will transfer to the valence band of g-CN, which reduces the recombination of the photogenerated charge carriers

(electron-hole pair). Hydroxyl radical production is unfavourable here as the reduction potential is lower than the ¯OH/ ˙OH redox couple [10].

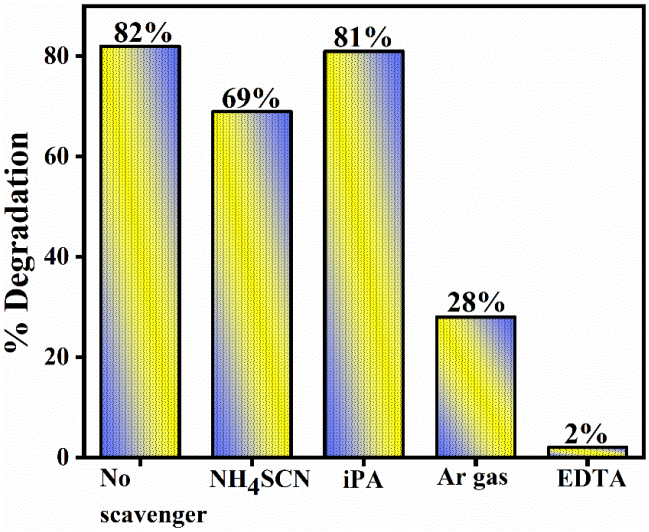

Fig. 4.16: Effect of Ar purging and NH_4SCN, EDTA, and iPA addition on the photocatalytic activity of the 10GBM catalyst.

4.3.9.2 Scavenger studies

Several control studies were investigated to verify the role of reactive entities **(Fig. 4.16)**. It was observed that upon the addition of NH_4SCN, the degradation efficiency decreased from 82% to 69% and by that of EDTA, it was reduced to 2%, as they function like a hole scavenger so accordingly suppress the oxidation of the pollutant (ofloxacin) with the hole. Additionally, the degradation efficiency was reduced to 28% after Ar gas purging resulting in a lowering of the $\cdot O_2^-$ production by eliminating O_2 from a reaction solution. All the conclusions support that the holes (h^+) and superoxide radicals ($\cdot O_2^-$) act as reactive species in the degradation mechanism[45,46]. However, the degradation efficiency does not alter significantly with the presence of isopropyl alcohol (iPA) which shows that hydroxyl radicals (·OH) are not participating in the degradation process.

4.3.10 HRMS studies

HRMS analyses were studied to obtain a detailed understanding of the reaction mechanism in **Scheme 1** and **Figs. 4.17**. The peak at m/z 362 is the corresponding peak of the protonated form of Ofloxacin. Furthermore, the signals at m/z 363 (**I1**), 158 (**I2**), 142 (**I3**), 125 (**I4**) and 123 (**I5**) indicate the intermediates formed during the degradation process (marked as I, stands for Identified fragments) and m/z 379 (**U1**), 365 (**U2**), 364 (**U3**) are the Unidentified fragments. It is worth noticeable that with increasing reaction time, the pollutant is degraded a little more into smaller products after half time as showed by the Identified fragments.

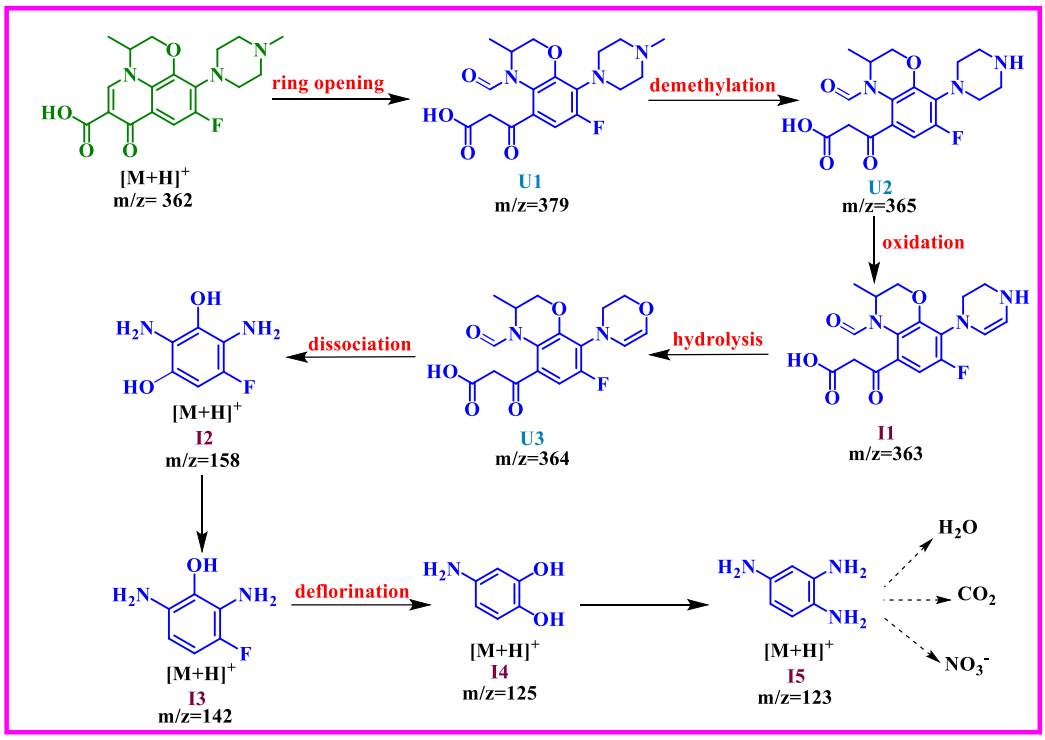

Scheme 1. A plausible mechanism for the degradation of Ofloxacin pollutant by 10GBM photocatalyst.

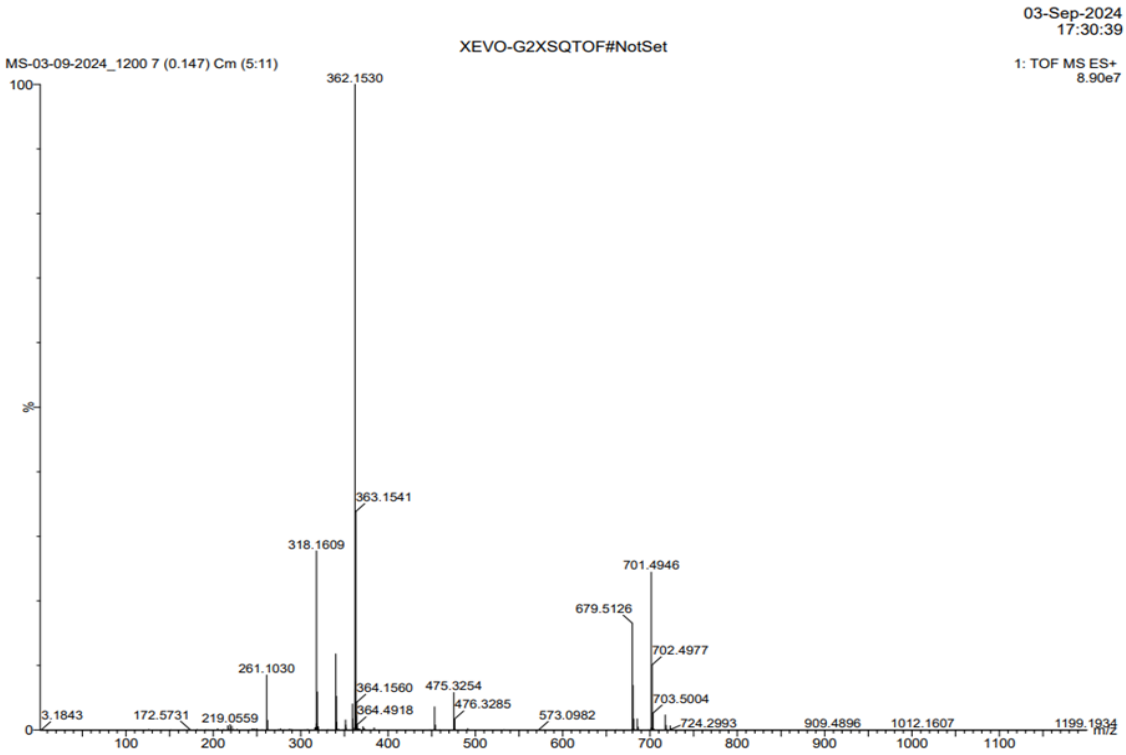

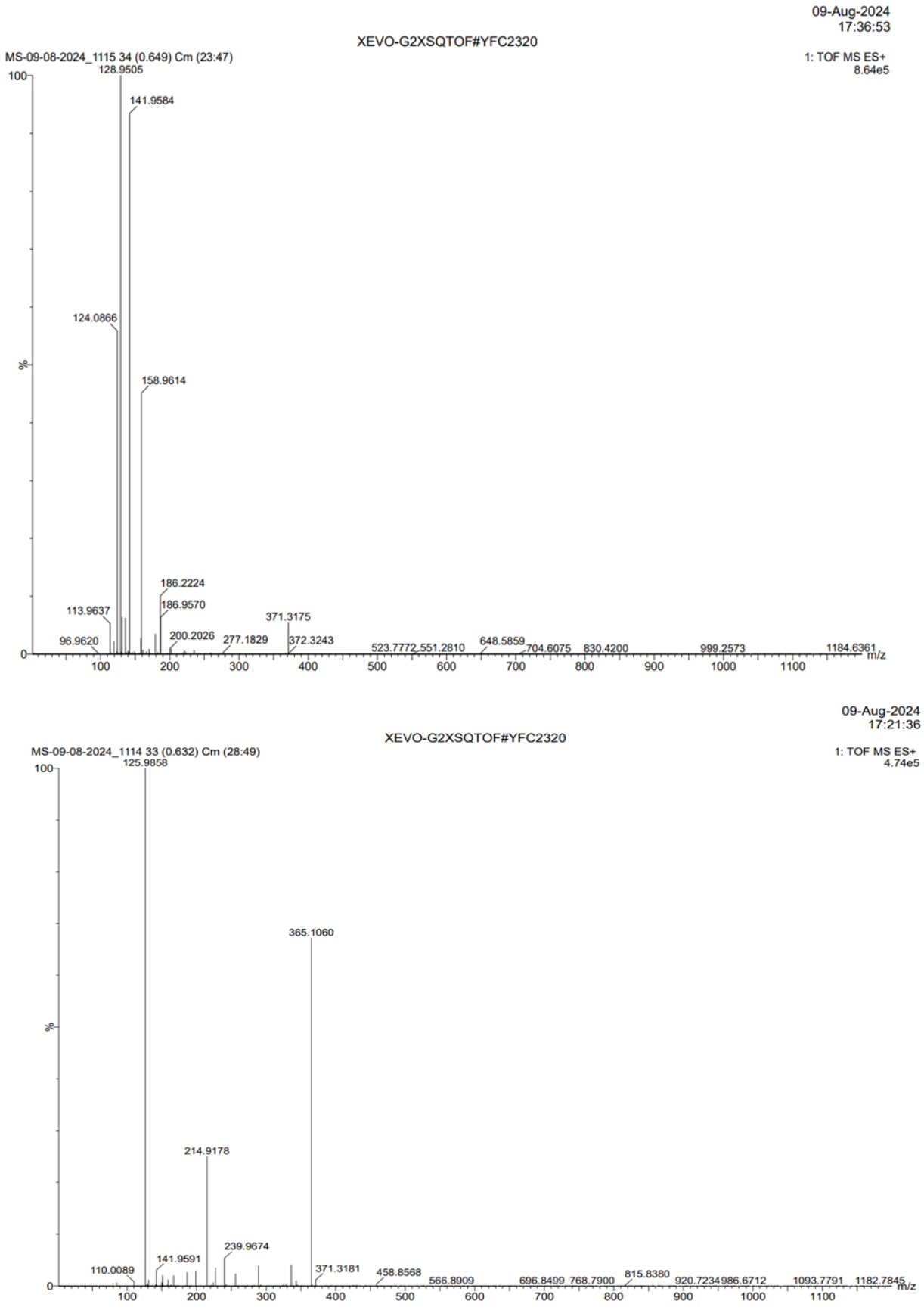

Fig. 4.17: The different fragments of ofloxacin using 10GBM photocatalyst

4.3.11 Recyclability and stability

For the application of the photocatalysts, their recyclability and stability are essential. The catalyst was extracted from the reaction mixture once it was completed and used in a successive reaction. The degradation efficiency using 10GBM photocatalyst has been found to decrease by just 10% following the fourth cycle when compared to the first **(Fig. 18)**, hence revealing that the composite has great reusability.

The apparent reduction in the photocatalytic activity can be due to the catalyst loss during washing and separation.

Moreover, the stability of the composite in **Fig. 19** was evaluated using FESEM, FTIR, and XRD after and before the photocatalytic reaction. Notably, before-after spectra of FTIR and XRD are nearly identical **(Fig. 19)**. Additionally, the morphology of the catalyst before and after the reaction remains similar as depicted by FESEM analysis. These outcomes confirm the excellent stability of the 10GBM composite.

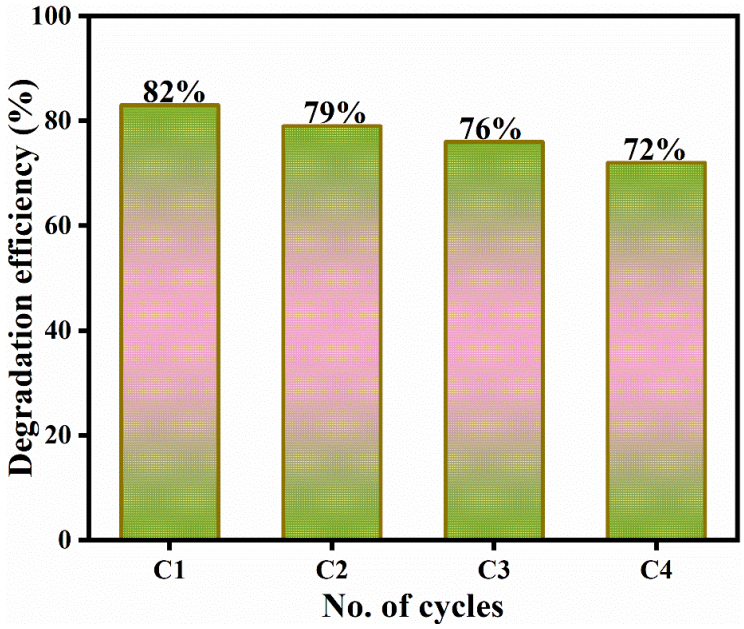

Fig. 18: Reusability using 10GBM composite up to four consecutive cycles of Ofloxacin degradation.

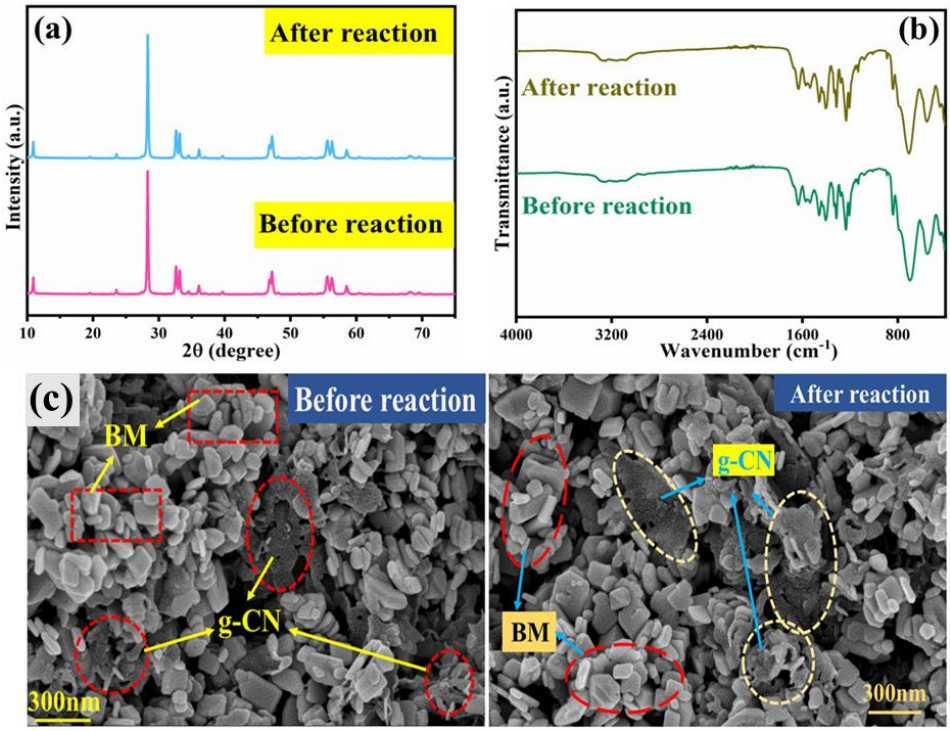

Fig. 19: Before and after reaction XRD and FTIR respectively (a, b) and FESEM (c) of 10GBM photocatalyst.

4.4 Comparison of degradation efficiency:

Notably, the 10GBM hybrid catalyst displays either superior or similar photocatalytic performance in the degradation of ofloxacin compared to many reported catalysts as shown in **Table 1**.

Table 1.

Comparative study of degradation efficiency using different catalysts for Ofloxacin.

S. No.	Catalyst	Degradation efficiency	Light source	Conc. of pollutants	Catalyst dose	Reaction time	References
1.	$AgBr/WO_3$	82.5%	Solar	10 mg/L (200 mL)	50 mg	180 min	[47]
2.	$BiOCl/TiO_2$	70%	Solar	100 mL of 0.2 g/L	0.15 g	10 min	[48]
3.	ZnO/CdS	73%	visible	10 mg/L	50 mg	120 min	[49]
4.	CdS	79%	visible	10 mg/L	0.25 g/L	80 min	[50]
5.	CdS/TiO_2	86%	visible	10 mg/L	0.45 g	180 min	[51]
6.	Bi-doped g-C_3N_4/Bi_2MoO_6	**82%**	visible	20 ppm	5 mg in 5 mL	180 min	**This work**

4.5. Conclusion:

To conclude, this report validates the fabrication of ternary Bi (0)-doped g-C_3N_4/Bi_2MoO_6 nanocomposite and evaluates their photodegradation process using the pharmaceutical drug Ofloxacin as a pollutant. Substantially, no additional reducing agent is needed to facilitate the formation of photocatalyst as the methanol which serves as a solvent here also plays the role of reducing agent and reduces Bi (III) to zerovalent Bi during the synthesis of Bi_2MoO_6. Bi (0) is dispersed throughout the Bi_2MoO_6 structure because of an in-situ hydrothermal reaction. The g-C_3N_4 loading simplifies the process of electron transfer in type-II heterojunction structure. In contrast, the metallic Bi increases the visible light response through the LSPR effect, resulting in better photocatalytic activity in degrading Ofloxacin under visible light. The reactive species are holes and superoxide radicals as demonstrated by the controlled experiments. The formation of various intermediates was examined by HRMS, which further provided more clarification to the reaction mechanism. Moreover, the recyclability studies confirmed the catalyst has outstanding stability and reusability. As a result, the current work may pave the way for developing plasmonic element-doped materials intended to remove harmful pollutants from wastewater.

References:

1 S. H. Ammar, F. D. Ali, H. J. Hadi and Z. H. Jabbar, Visible-light-induced photodegradation of ofloxacin antibiotic by facile assembled $BiFeO_3$/Bi-modified g-C_3N_4 heterojunctions, *Mater. Sci. Semicond. Process*, 2023, **171**,108026.

2 S. Adhikari and D. H. Kim, Synthesis of Bi_2S_3/Bi_2WO_6 hierarchical microstructures for enhanced visible light driven photocatalytic degradation and photoelectrochemical sensing of ofloxacin, *Chem. Eng. J.*, 2018, **354**, 692–705.

3 T. Chankhanittha and S. Nanan, Visible-light-driven photocatalytic degradation of ofloxacin (OFL) antibiotic and Rhodamine B (RhB) dye by solvothermally grown ZnO/Bi_2MoO_6 heterojunction, *J. Colloid Interface Sci.*, 2021, **582**, 412–427.

4 P. Chen, L. Blaney, G. Cagnetta, J. Huang, B. Wang, Y. Wang, S. Deng and G. Yu, Degradation of Ofloxacin by Perylene Diimide Supramolecular Nanofiber Sunlight-Driven Photocatalysis, *Environ. Sci. Technol.*, 2019, **53**, 1564–1575.

5 Q. Shang, X. Liu, M. Zhang, P. Zhang, Y. Ling, G. Cui, W. Liu, X. Shi, J. Yue and B. Tang, Photocatalytic degradation of ofloxacin antibiotic wastewater using TS-1/C_3N_4 composite photocatalyst: Reaction performance optimisation and estimation of wastewater component

synergistic effect by artificial neural network and genetic algorithm, *Chem. Eng. J.*, 2022, **443**, 136354

6 Q. Su, J. Li, H. Yuan, B. Wang, Y. Wang, Y. Li and Y. Xing, Visible-light-driven photocatalytic degradation of ofloxacin by g-C_3N_4/NH_2 -MIL-88B(Fe) heterostructure: Mechanisms, DFT calculation, degradation pathway and toxicity evolution, *Chem. Eng. J.*, 2022, **427**, 131594

7 W. Chen, Z. Xing, N. Zhang, T. Cheng, B. Ren, X. Liu, Z. Wang, Z. Li and W. Zhou, Hierarchical $Bi_2Fe_4O_9$/BiOI S-scheme heterojunctions with exceptional hydraulic shear induced photo-piezoelectric catalytic activity, npj *Clean Water.*, 2024, **7**, 86.

8 H. Li, W. Zhang and Y. Liu, HZSM-5 zeolite supported boron-doped TiO_2 for photocatalytic degradation of ofloxacin*, J. Mater. Res. Technol.*, 2020, **9**, 2557–2567.

9 K. Rabé, L. Liu, N. A. Nahyoon, Y. Zhang, A. M. Idris, J. Sun and L. Yuan, Fabrication of high efficiency visible light Z-scheme heterostructure photocatalyst g-C_3N_4/Fe0(1%)/TiO_2 and degradation of rhodamine B and antibiotics, *J. Taiwan Inst. Chem. Eng.*, 2019, **96**, 463–472.

10 P. Rohilla, B. Pal and R. K. Das, Bi-doped g-C_3N_4/Bi_2WO_6 ternary composites for superior photocatalytic degradation of reactive orange 16 under visible light irradiation, *J. Ind. Eng. Chem.,* 2025, **141**, 456-467.

11 J. Wang, L. Tang, G. Zeng, Y. Liu, Y. Zhou, Y. Deng, J. Wang and B. Peng, Plasmonic Bi metal deposition and g-C_3N_4 coating on Bi_2WO_6 Microspheres for Efficient visible light Photocatalysis, *ACS Sustain Chem. Eng.*, 2017, **5**, 1062–1072.

12 H. Huang, J. Zhao, H. Guo, B. Weng, H. Zhang, R. A. Saha, M. Zhang, F. Lai, Y. Zhou, R. Z. Juan, P. C. Chen, S. Wang, J. A. Steele, F. Zhong, T. Liu, J. Hofkens, Y. M. Zheng, J. Long and M. B. J. Roeffaers, Noble-Metal-Free High-Entropy Alloy Nanoparticles for Efficient Solar-Driven Photocatalytic CO_2 Reduction, *Adv. Mater.*, 2024, **36**, 2313209.

13 W. Cheng, L. Wang, H. Lao, Y. Wei, J. Xu and B. Weng, Unraveling the Plasmonic Effect of Au in Promoting Photocatalytic H_2 Generation and Organic Synthesis, *ACS Sustain. Chem. Eng.*, 2024, **12**, 17026–17034.

14 H. Zhang, Y. Gao, S. Meng, Z. Wang, P. Wang, Z. Wang, C. Qiu, S. Chen, B. Weng and Y. M. Zheng, Metal Sulfide S-Scheme Homojunction for Photocatalytic Selective Phenylcarbinol Oxidation, *Adv. Sci.*, 2024, **11**, 2400099.

15 Q. Liang, M. Zhang, C. Yao, C. Liu, S. Xu and Z. Li, High performance visible-light driven photocatalysts of Bi_2MoO_6-g-C_3N_4 with controllable solvothermal fabrication, *J. Photochem. Photobiol. A Chem.*, 2017, **332**, 357–363.

16 Z. Zhao, W. Zhang, Y. Sun, J. Yu, Y. Zhang, H. Wang, F. Dong and Z. Wu, Bi Cocatalyst/Bi_2MoO_6 Microspheres Nanohybrid with SPR-Promoted Visible-Light Photocatalysis, *J. Phys. Chem. C*, 2016, **120**, 11889–11898.

17 W. Guo, K. Fan, J. Zhang and C. Xu, 2D/2D Z-scheme Bi_2WO_6/Porous-g-C_3N_4 with synergy of adsorption and visible-light-driven photodegradation, *Appl. Surf. Sci.*, 2018, **447**, 125–134.

18 Y. Huang, S. Kang, Y. Yang, H. Qin, Z. Ni, S. Yang and X. Li, Facile synthesis of Bi/Bi_2WO_6 nanocomposite with enhanced photocatalytic activity under visible light, *Appl. Catal. B*, 2016, **196**, 89–99.

19 B. J. Rani, R. Yuvakkumar, G. Ravi, M. Pannipara, A. G. Al-Sehemi and D. Velauthapillai, Bi_2MoO_6 hierarchical microflowers for electrochemical oxygen evolution reaction, *Int. J. Hydrogen Energy*, 2021, **46**, 18719–18728.

20 V. D. Dang, J. Adorna, T. Annadurai, T. A. N. Bui, H. L. Tran, L. Y. Lin and R. A. Doong, Indirect Z-scheme nitrogen-doped carbon dot decorated Bi_2MoO_6/g-C_3N_4 photocatalyst for enhanced visible-light-driven degradation of ciprofloxacin, *Chem. Eng. J.*, 2021, **422**, 130103.

21 P. Rohilla, B. Pal and R. K. Das, Improved photocatalytic degradation of rhodamine B by g-C_3N_4 loaded $BiVO_4$ nanocomposites, *Heliyon*, 2023, **9**, e21900.

22 D. Y. Liu, J. H. Dong, F. M. Liu, X. F. Gao, Y. Yu, S. B. Zhang, L. M. Dong and Y. K. Guo, Synthesis and photocatalytic performance of g-C_3N_4 composites, *J. Ovonic Res.*, 2019, **15**, 239 – 246.

23 L. Wang, Z. Liu, D. Wang, S. Ni, D. Han, W. Wang and L. Niu, Tailoring hetero structured Bi_2MoO_6/Bi_2S_3 nanobelts for highly selective photoelectrochemical analysis of gallic acid at drug level, *Biosens. Bioelectron.*, 2017, **94**, 107–114.

24 F. Xu, J. Wang, N. Zhang, H. Liang and H. Sun, Simultaneously generating Bi quantum dot and oxygen vacancy on Bi_2MoO_6 nanosheets for boosting photocatalytic selective alcohol oxidation, *Appl. Surf. Sci.*, 2022, **575**,151738.

25 J. Bai, X. Li, Z. Hao and L. Liu, Enhancement of 3D Bi_2MoO_6 mesoporous spheres photocatalytic performance by vacancy engineering, *J. Colloid Interface Sci.*, 2020, **560**, 510–518.

26 D. S. Vavilapalli, R. G. Peri, R. K. Sharma, U. K. Goutam, B. Muthuraaman, M. S. Ramachandra Rao and S. Singh, g-C_3N_4/$Ca_2Fe_2O_5$ heterostructures for enhanced photocatalytic degradation of organic effluents under sunlight, *Sci. Rep.*, 2021, **11**, 19639.

27 Z. Mao, J. Chen, Y. Yang, L. Bie, B. D. Fahlman and D. Wang, Modification of surface properties and enhancement of photocatalytic performance for g-C_3N_4 via plasma treatment, *Carbon*, 2017, **123**, 651–659.

28 Y. Wang, S. Zhao, Y. Zhang, J. Fang, Y. Zhou, S. Yuan, C. Zhang and W. Chen, One-pot synthesis of K-doped g-C_3N_4 nanosheets with enhanced photocatalytic hydrogen production under visible-light irradiation, *Appl. Surf. Sci.*, 2018, **440**, 258–265.

29 M. Zhu, S. Kim, L. Mao, M. Fujitsuka, J. Zhang, X. Wang and T. Majima, Metal-Free Photocatalyst for H_2 Evolution in Visible to Near-Infrared Region: Black Phosphorus/Graphitic Carbon Nitride, *J. Am. Chem. Soc.*, 2017, **139**, 13234–13242.

30 N. Li, L. Zhu, W. De Zhang, Y. X. Yu, W. H. Zhang and M. F. Hou, Modification of TiO2 nanorods by Bi_2MoO_6 nanoparticles for high performance visible-light photocatalysis, *J. Alloys Compd*, 2011, **509**, 9770–9775.

31 M. Sierra, E. Borges, P. Esparza, J. Méndez-Ramos, J. Martín-Gil and P. Martín-Ramos, Photocatalytic activities of coke carbon/g-C_3N_4 and Bi metal/Bi mixed oxides/g-C_3N_4 nanohybrids for the degradation of pollutants in wastewater, *Sci. Technol. Adv. Mater.*, 2016, **17**, 659–668.

32 E. Vesali-Kermani, A. Habibi-Yangjeh, H. Diarmand-Khalilabad and S. Ghosh, Nitrogen photo fixation ability of g-C_3N_4 nanosheets/Bi_2MoO_6 heterojunction photocatalyst under visible-light illumination, *J. Colloid Interface Sci.*, 2020, **563**, 81–91.

33 W. Xue, D. Huang, J. Li, G. Zeng, R. Deng, Y. Yang, S. Chen, Z. Li, X. Gong and B. Li, Assembly of AgI nanoparticles and ultrathin g-C_3N_4 nanosheets codecorated Bi_2WO_6 direct dual Z-scheme photocatalyst: An efficient, sustainable and heterogeneous catalyst with enhanced photocatalytic performance, *Chem. Eng. J.*, 2019, **373**, 1144–1157.

34 T. Wang, Y. Bai, W. Si, W. Mao, Y. Gao and S. Liu, Heterogeneous photo-Fenton system of novel ternary Bi2WO6/BiFeO3/g-C3N4 heterojunctions for highly efficient degrading persistent organic pollutants in wastewater, *J. Photochem. Photobiol. A Chem.*, 2021, **404**,112856.

35 Y. Su, G. Tan, T. Liu, L. Lv, Y. Wang, X. Zhang, Z. Yue, H. Ren and A. Xia, Photocatalytic properties of Bi_2WO_6/$BiPO_4$ Z-scheme photocatalysts induced by double internal electric fields, *Appl. Surf. Sci.*, 2018, **457**, 104–114.

36 D. Chen, Q. Hao, Z. Wang, H. Ding and Y. Zhu, Influence of phase structure and morphology on the photocatalytic activity of bismuth molybdates, *Cryst. Eng. Comm.*, 2016, **18**, 1976–1986.

37 G. Yang, Y. A. Zhu, Y. Liang, J. Yang, K. Wang, Z. Zeng, R. Xu and X. Xie, Crystal defect-mediated {0 1 0} facets of Bi_2MoO_6 nanosheets for removal of TC: Enhanced mechanism and degradation pathway, *Appl. Surf. Sci.*, 2021, **539**,148038.

38 A. Kundu, S. Sharma and S. Basu, Modulated BiOCl nanoplates with porous g-C_3N_4 nanosheets for photocatalytic degradation of color/colorless pollutants in natural sunlight, *J. Phys. Chem. Sol.*, 2021, **154**, 110064.

39 S. Singla, P. Devi and S. Basu, Revolutionizing the Role of Solar Light Responsive $BiVO_4$/BiOBr Heterojunction Photocatalyst for the Photocatalytic Deterioration of Tetracycline and Photo electro catalytic Water Splitting, *Mater.*, 2023, **16**, 5661.

40 C. Murugan, M. Karnan, M. Sathish and A. Pandi kumar, Construction of heterostructure based on hierarchical Bi_2MoO_6 and g-C_3N_4 with ease for impressive performance in photoelectrocatalytic water splitting and supercapacitor, *Catal. Sci. Technol.*, 2020, **10**, 2427–2442.

41 K. Wu, X. Qiu, Y. Luo and C. Zhang, Oxygen Vacancy Mediated-Bismuth Molybdate/Graphitic Carbon Nitride Type II Heterojunction Chemiresistor for Efficient NH_3 Detection at Room Temperature, *ACS Sens.*, 2024, **9,** 6698–6708.

42 N. Tian, H. Huang, Y. He, Y. Guo, T. Zhang and Y. Zhang, Mediator-free direct Z-scheme photocatalytic system: $BiVO_4$/g-C_3N_4 organic–inorganic hybrid photocatalyst with highly efficient visible-light-induced photocatalytic activity, *Dalton Trans.*, 2015, **44**, 4297–4307.

43 T. Han, Y. Chen and H. Shi, Construction of a Bi_2MoO_6/CoOx/Au system with a dual-channel charge transfer path for enhanced tetracycline degradation, *Catal. Sci. Technol.*, 2022, **12**, 5565–5574.

44 W. Hu, J. Yu, X. Jiang, X. Liu, R. Jin, Y. Lu, L. Zhao, Y. Wu and Y. He, Enhanced photocatalytic activity of g-C_3N_4 via modification of $NiMoO_4$ nanorods, *Colloids Surf. A: Physicochem. Eng. Asp.*, 2017, **514**, 98–106.

45 B. R. Shah and U. D. Patel, Mechanistic aspects of photocatalytic degradation of Lindane by TiO_2 in the presence of Oxalic acid and EDTA as hole-scavengers, *J. Environ. Chem. Eng.*, 2021, **9**, 105458.

46 M. Chahkandi and M. Zargazi, New water based EPD thin $BiVO_4$ film: Effective photocatalytic degradation of Amoxicillin antibiotic, *J. Hazard Mater.*, 2020, **389**, 121850.

47 J. Piriyanon, P. Takhai, S. Patta, T. Chankhanittha, T. Senasu, S. Nijpanich, S. Juabrum, N. Chanlek and S. Nanan, Performance of sunlight responsive WO_3/AgBr heterojunction photocatalyst toward degradation of Rhodamine B dye and ofloxacin antibiotic, *Opt. Mater.*, 2021, **121**, 111573.

48 Q. Wang, P. Li, Z. Zhang, C. Jiang, K. Zuojiao, J. Liu and Y. Wang, Kinetics and mechanism insights into the photodegradation of tetracycline hydrochloride and ofloxacin mixed antibiotics with the flower-like BiOCl/TiO_2 heterojunction, *J. Photochem. Photobiol. A Chem.*, 2019, **378**, 114–124.

49 T. Senasu, T. Chankhanittha, K. Hemavibool and S. Nanan, Visible-light-responsive photocatalyst based on ZnO/CdS nanocomposite for photodegradation of reactive red azo dye and ofloxacin antibiotic, *Mater. Sci. Semicond. Process*, 2021, **123**, 105558.

50 M. Kaur, S. K. Mehta and S. K. Kansal, Visible light driven photocatalytic degradation of ofloxacin and malachite green dye using cadmium sulphide nanoparticles, *J. Environ. Chem. Eng.*, 2018, **6**, 3631–3639.

51 A. Kaur, A. Umar, W. A. Anderson and S. K. Kansal, Facile synthesis of CdS/TiO_2 nanocomposite and their catalytic activity for ofloxacin degradation under visible illumination, *J. Photochem. Photobiol. A Chem.*, 2018, **360**, 34–43.

Summary and Future outlook

This study reported the feasible synthesis of bimetallic bismuth-based oxide compounds like $BiVO_4$, Bi_2WO_6, and Bi_2MoO_6, which contain different elements in the structure along with bismuth like V, W, and Mo, etc. They are synthesized using various preparation methods and then characterized. Additionally, g-C_3N_4 is a highly stable carbon-containing material that is non-toxic in nature, easily synthesized, low-cost or economical, and efficient material in the field of adsorption and photocatalysis. According to the research study that was carried out, it was observed that by loading of g-C_3N_4 (g-CN) over bimetallic bismuth oxide (BBO) compounds, adsorption and photocatalytic degradation activity can be boosted. It was noted that coupling g-CN with BBO augmented the adsorption of different pollutants over the nanocomposites by increasing the surface-active sites, lowering the charge transfer resistance, and broadening the light absorption potential. The three different heterojunction structure are showing different surface area such as in case of g-C_3N_4@$BiVO_4$, the surface area increased from 6.7 m^2/g to 13.4 m^2/g, similarly in case of g-C_3N_4@Bi/Bi_2WO_6, it was increased from 26.5 m^2/g to 44.5 m^2/g. In last case that is g-C_3N_4@Bi/Bi_2MoO_6, it increased from 6.63 m^2/g to 12.2 m^2/g. Moreover, the charge transfer property also increased on loading of g-C_3N_4 in all the three-heterojunction system. In addition, the photocatalytic degradation efficiency was also enhanced upon loading of g-C_3N_4. In case of g-C_3N_4@$BiVO_4$, bare $BiVO_4$ has efficiency of ~19% and its composite with g-CN has 86%. Similarly, pure Bi/Bi_2WO_6 has shown insignificant degradation efficiency but its nanocomposite depicted 89% removal of the pollutant. In case of last material, g-C_3N_4@Bi/Bi_2MoO_6 pristine Bi/Bi_2MoO_6 has 42% while its composite upon loading with g-CN increased the degradation rate up to 82%.

The synthesized nanocomposites are highly proficient in the degradation of toxic pollutants using economical LED light sources. The HRMS studies and mineralization techniques (TOC and COD) provided more clarity about the dissociation of pollutants into smaller fragments. Moreover, the loading of non-noble plasmonic metal Bi has been successfully achieved via in situ reduction without adding any extra reducing agent. Herein, the metallic bismuth is deposited uniformly throughout the Bi_2WO_6 and Bi_2MoO_6 lattice, whereas the traditional photoreduction method leads to loading of plasmonic metals predominantly on the surface only. Furthermore, due to the non-fluorescent behaviour of bimetallic bismuth oxide compounds, the changes in electron-hole pair recombination rate cannot be monitored, but instead, the improved photocatalytic activity was found to be due to improved optical absorption and lowering of charge transfer resistance.

Such observations will open a new direction for the researchers to prepare non-noble plasmonic metal-loaded hybrid materials using the in-situ reduction method and explore the photocatalytic activities of the non-fluorescent material-based hybrid nanocomposites in the future.

List of Publications

1. **Priti Rohilla**, Bonamali Pal, Raj Kumar Das **(2023)**, "Improved photocatalytic degradation of Rhodamine B by g-C_3N_4 loaded $BiVO_4$ nanocomposites", **Heliyon**, 9, e21900 **(I.F.= 3.4)**. *https://doi.org/10.1016/j.heliyon.2023.e21900*
2. **Priti Rohilla**, Bonamali Pal, Raj Kumar Das **(2025)**, "Bi-doped g-C_3N_4/Bi_2WO_6 ternary composites for superior photocatalytic degradation of reactive orange 16 under visible light irradiation", **Journal of Industrial and Engineering Chemistry**, 141, 456-467 **(I.F.= 5.9)**. *https://doi.org/10.1016/j.jiec.2024.07.007*
3. **Priti Rohilla**, Bonamali Pal, Raj Kumar Das **(2025)**, "Construction of Bi-doped g-C_3N_4/Bi_2MoO_6 ternary nanocomposite for the effective photodegradation of Ofloxacin under visible light irradiation", **RSC Advances,** 15, 2347-2360 **(I.F.= 3.9).** *https://doi.org/10.1039/D4RA08493D*
4. **Priti Rohilla,** Raj Kumar Das, "A Review on bismuth vanadate ($BiVO_4$) photocatalyst: Different synthesis, morphology and photocatalytic degradation of toxic pollutants" **(Manuscript under preparation)**

Other Publications

1. **Priti Rohilla**, Ishita Dhiman, Kamya Jasuja, Raj Kumar Das, "Photocatalytic degradation of Ofloxacin using bare $BiVO_4$ under visible light irradiation" **(Manuscript under preparation)**
2. Kamya Jasuja, Tania, **Priti Rohilla**, Raj Kumar Das, "Improved adsorptive removal of reactive dye with Co-Al layered double hydroxide" **Journal of the Indian Chemical Society**, **(I.F.=3.2) (Communicated)**
3. **Priti Rohilla,** Shikha Rani, Bonamali Pal, "Photocatalytic H_2O Splitting and methanol dehydrogenation using Core-shell bismuth vanadate @Ag/TiO_2 under solar irradiation" **(writeup in progress)**

Conferences and Workshops

1. **Volunteered** in **SCI-FEST 2022**, held at Thapar Institute of Engineering and Technology, Patiala, on 7th June, 2022.

2. **Attended** "International conference on emerging trends in science and technology" **(ICETST-2022),** organized by the Department of Applied Sciences, Punjab Engineering College, Chandigarh, 10th -11th June, 2022.

3. **Poster presentation on the topic,** "g-C_3N_4 loaded Bimetallic bismuth oxide nanocomposite for photocatalytic degradation of toxic pollutants" International conference on Sustainable development in Chemical and Environmental Engineering, **(SDCEE-2024),** held at Thapar University, Patiala 147004 (Punjab), 22nd-24th February, 2024.

4. **Poster presentation on the topic,** "Fabrication of g-C_3N_4 loaded bimetallic bismuth oxide-based nanocomposites to remove toxic pollutants by photocatalysis" International conference on Role of Chemical Engineering towards Sustainable Development and Atmanirbhar Bharat, **(IIChE-ChemCon 2024),** held at NIT Jalandhar (Punjab), 27th-30th December, 2024.

priti thesis plagiarism check

ORIGINALITY REPORT

14%	10%	10%	2%
SIMILARITY INDEX	INTERNET SOURCES	PUBLICATIONS	STUDENT PAPERS

PRIMARY SOURCES

1	pubs.rsc.org Internet Source	1%
2	doaj.org Internet Source	1%
3	Wee-Jun Ong, Lling-Lling Tan, Yun Hau Ng, Siek-Ting Yong, Siang-Piao Chai. " Graphitic Carbon Nitride (g-C N)-Based Photocatalysts for Artificial Photosynthesis and Environmental Remediation: Are We a Step Closer To Achieving Sustainability? ", Chemical Reviews, 2016 Publication	1%
4	www.mdpi.com Internet Source	1%
5	Harpreet Kaur, Satnam Singh, Bonamali Pal. "Effect of plasmonic metal (Cu, Ag, and Au) loading over the physicochemical and photocatalytic properties of Mg-Al LDH towards degradation of tetracycline under LED light", Applied Surface Science, 2022 Publication	1%
6	c.coek.info Internet Source	1%
7	Mehak Bansal, Bonamali Pal. "Synergy of adsorption and visible light-induced photocatalytic degradation of doxycycline by cellulose modified Cu Al layered double	<1%

Raj Kumar Das

Heliyon 9 (2023) e21900

Contents lists available at ScienceDirect

Heliyon

journal homepage: www.cell.com/heliyon

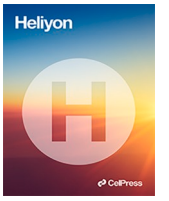

Improved photocatalytic degradation of rhodamine B by g-C_3N_4 loaded $BiVO_4$ nanocomposites

Priti Rohilla [a], Bonamali Pal [a,b], Raj Kumar Das [a,b,*]

[a] School of Chemistry and Biochemistry, Thapar Institute of Engineering & Technology, Patiala, 147004, Punjab, India
[b] TIET-Virginia Tech Center of Excellence in Emerging Materials, Thapar Institute of Engineering and Technology, Patiala, 147004, India

ARTICLE INFO

Keywords:
$BiVO_4$
Binary composite
Photocatalysis
Wastewater treatment
Emerging contaminants

ABSTRACT

Photocatalytic degradation has emerged as one of the most efficient methods to eliminate toxic dyes from wastewater. In this context, graphitic nitride (g-C_3N_4) loaded $BiVO_4$ nanocomposites (5 wt% g-CN@$BiVO_4$ and 10 wt% g-CN@$BiVO_4$) have been fabricated by the wet impregnation method, and their efficiency towards photocatalytic removal of rhodamine B have been investigated under visible light irradiation. These hybrid composites have been characterized by XRD, FESEM, HRTEM, EDS-mapping, UV-Vis DRS, DLS, XPS and BET, etc. The HRTEM images revealed that $BiVO_4$ has a decagonal shape covered by a layered nanosheet-like structure of g-C_3N_4. BET measurements suggest increasing the proportion of g-C_3N_4 results enhancement of the specific surface area. Among different photocatalysts, the 10 wt% g-C_3N_4@$BiVO_4$ hybrid possesses the best catalytic activity with 86% degradation efficiency after 60 min of reaction time. The LC-MS studies suggest that the degradation reactions follow the de-ethylation pathway. Even after five cycles, the heterostructure shows only a 14% decrease in photocatalytic activity, confirming its stability. As a result, the binary composite can be regarded as a promising catalyst for the degradation of pollutants due to its ease of preparation, high stability and superior catalytic activity.

1. Introduction

Water contamination has played a significant role in the recent increase in worldwide environmental pollution, which is primarily due to the textile industry. According to studies, between 10 and 12% of the dyes are classified as hazardous waste, with Rhodamine B being one of the contaminants [1,2]. Rhodamine B, a member of the xanthene family, is frequently employed in the textile industry due to its stability, solubility in water, and brightness [3]. Even at smaller concentrations (1 ppm), the dye has a detrimental impact on the aquatic environment [4]. The dye has a dangerous and mutagenic effect in that it harms people by affecting their brain, central nervous system, liver, and kidneys [5]. As a result, many techniques for their removal have been developed [6].

The reliable method for removing toxins from water is thought to be semiconductor-based photocatalysts. $BiVO_4$ has emerged as an excellent photocatalyst due to its narrow band gap (2.4eV), low toxicity, corrosion resistance, chemical stability, etc [7,8]. The photoactivity of bare $BiVO_4$ is not very significant due to the rapid electron-hole pair recombination rate and smaller specific surface area [9]. Therefore, combining it with other materials, such as metals and non-metals, to create composites with heterojunction structures has now emerged as a great option [10]. Such methodologies result in an improvement of the sensitivity towards visible light

* Corresponding author. School of Chemistry and Biochemistry, Thapar Institute of Engineering & Technology, Patiala, 147004, Punjab, India.
E-mail address: rkdas@thapar.edu (R.K. Das).

https://doi.org/10.1016/j.heliyon.2023.e21900
Received 26 August 2023; Received in revised form 10 October 2023; Accepted 31 October 2023
Available online 5 November 2023

Journal of Industrial and Engineering Chemistry xxx (xxxx) xxx

Contents lists available at ScienceDirect

Journal of Industrial and Engineering Chemistry

journal homepage: www.elsevier.com/locate/jiec

Full Length Article

Bi-doped g-C_3N_4/Bi_2WO_6 ternary composites for superior photocatalytic degradation of reactive orange 16 under visible light irradiation

Priti Rohilla [a], Bonamali Pal [a,b,*], Raj Kumar Das [a,b,*]

[a] Department of Chemistry and Biochemistry, Thapar Institute of Engineering & Technology, Patiala 147004, Punjab, India
[b] TIET-Virginia Tech Center of Excellence in Emerging Materials, Thapar Institute of Engineering and Technology, Patiala 147004, India

ARTICLE INFO

Keywords:
Bi_2WO_6
Hybrid composites
Photocatalytic degradation
Wastewater treatment
Reactive dyes
Emerging contaminants

ABSTRACT

Because of unrestricted disposal, the concentration of reactive dyes in wastewater is gradually increasing. Owing to their eco-toxicity their removal becomes so crucial. In this regard, Bi(0)-doped g-C_3N_4/Bi_2WO_6 (g-C_3N_4/Bi@Bi_2WO_6) nanocomposites were prepared by wet impregnation followed by calcination. Remarkably, the Bi(0) doping occurs concertedly during the preparation of Bi_2WO_6 without the addition of any extra reducing agent. The efficacy of the photocatalyst for eliminating reactive orange 16 was evaluated under visible light irradiation. XRD, FESEM, HRTEM, DRS, XPS, BET, etc., were employed to characterize these hybrids. The presence of Bi(0) was confirmed by HRTEM and XPS. Increasing the g-C_3N_4 content enhances the specific surface and reduces the charge transfer resistance. Among the various photocatalysts, the 20 wt% g-C_3N_4/Bi@Bi_2WO_6 hybrid owned the highest degradation efficiency of 89 % after 300 min of reaction time. The controlled experiments confirm the participation of holes and superoxide anions during the reactions. The various reaction intermediates were detected by HRMS providing the necessary evidence about the mechanism. The heterostructure possesses excellent reusability and stability. Due to enhanced catalytic activity, high stability, and ease of synthesis, the reported composite can be considered as a promising catalyst for the degradation of pollutants.

Introduction

In recent years, excessive use of organic dyes by the textile industries has emerged as one of the most important threats to the ecosystem [1]. Reactive dyes are one of the foremost widely used colorants in the textile industry. These dyes react with cotton fabric to form covalent bonds, thereby resulting in quite a strong affinity towards the fabric. As a result, they possess exceptionally high wet fastness [2]. Unfortunately, textile effluents contain a significant concentration of unfixed dyes that are disposed of directly into the environment. These dyes have a harsh impact on the environment as they are carcinogenic, mutagenic, and highly toxic [3–6]. Moreover, they also significantly affect the aquatic ecosystem, human beings, and crop productivity [7–9]. The elimination of these dye effluents is tricky due to their structural complexity, high stability, and poor biodegradability. Consequently, their efficient elimination from wastewater becomes extremely important. To date, several techniques, such as ion exchange, coagulation, nano-filtration, adsorption, photocatalysis, etc., have been developed [10] one of the most promising methodologies in wastewater treatment as it results in the total decomposition of the pollutants instead of transmitting them from one medium to another [11,12].

Nowadays, semiconductor-based photocatalysts have attracted a significant amount of interest in the area of wastewater treatment [13–15]. Bi_2WO_6 is a member of the Aurivillius class of perovskite oxide. Its structure consists of alternate layers of anionic $(WO_4)_2^-$ and cationic $(Bi_2O_2)^{2+}$ sheets. It has drawn much attention because of its exceptional electronic properties, stability, reactivity, low toxicity, etc [16–18]. However, the principal drawback of pure Bi_2WO_6 is interrelated with its low absorbance in the visible region, high charge transfer resistance, fast electron-hole pair recombination, photo-corrosion, low surface area, etc. These shortcomings can be resolved using a variety of strategies. Common techniques for modifying this semiconductor photocatalyst's band structure include element doping [19–21] and heterojunction construction [22–24]. One of the most capable materials for producing a semiconductor heterojunction is g-C_3N_4 because of its low cost and high stability. In addition, g-C_3N_4 has additional benefits like a unique energy

Abbreviations: BW, Bi@Bi_2WO_6; g-CN, g-C_3N_4; 5GBW, 5 wt% g-C_3N_4/Bi@Bi_2WO_6; 10GBW, 10 wt% g-C_3N_4/Bi@Bi_2WO_6; 20GBW, 20 wt% g-C_3N_4/Bi@Bi_2WO_6; RO-16, Reactive Orange 16; VB, Valence Band; CB, Conduction Band; PVDF, Polyvinylidene fluoride; CB, Carbon black; NMP, N-Methyl-2-pyrrolidone.

* Corresponding authors at: Department of Chemistry and Biochemistry, Thapar Institute of Engineering & Technology, Patiala 147004, Punjab, India.
E-mail addresses: bpal@thapar.edu (B. Pal), rkdas@thapar.edu (R.K. Das).

https://doi.org/10.1016/j.jiec.2024.07.007
Received 4 April 2024; Received in revised form 21 June 2024; Accepted 5 July 2024
Available online 9 July 2024

Please cite this article as: Priti Rohilla et al., *Journal of Industrial and Engineering Chemistry*, https://doi.org/10.1016/j.jiec.2024.07.007

RSC Advances

PAPER

View Article Online
View Journal | View Issue

Cite this: *RSC Adv.*, 2025, **15**, 2347

Construction of a Bi-doped g-C_3N_4/Bi_2MoO_6 ternary nanocomposite for the effective photodegradation of ofloxacin under visible light irradiation†

Priti Rohilla,[a] Bonamali Pal*[ab] and Raj Kumar Das *[ab]

Water contamination is a result of the excessive use of antibiotics nowadays. Owing to this environmental toxicity, photocatalytic degradation is the primary approach to non-biological degradation for their removal. In this context, zerovalent Bi-doped g-C_3N_4/Bi_2MoO_6 [g-C_3N_4/Bi@Bi_2MoO_6] ternary nanocomposite was prepared using the wet impregnation method. Surprisingly, zerovalent Bi is generated simultaneously during the hydrothermal synthesis of Bi_2MoO_6 without using any additional reducing agent. The performance of the synthesized catalyst for the removal of ofloxacin is measured using visible light radiation. Various techniques like XRD, XPS, DRS, HRTEM, FESEM, *etc.*, were used to characterize the nanocomposites. Additionally, XPS, DRS, and HRTEM confirm the presence of zerovalent Bi. The degradation efficiency was recorded as 82% after 3 h for the optimized catalyst. The control experiments confirm that the superoxide radicals and holes function as reactive entities in the degradation process. HRMS was used to identify the intermediates and various fragments, which support the suggested mechanism. The photocatalyst exhibits outstanding stability and reusability. Due to its stability, easy synthesis, excellent catalytic activity, and reusability, the reported photocatalyst can be considered to be an excellent candidate for photocatalytic pollutant degradation.

Received 2nd December 2024
Accepted 17th January 2025

DOI: 10.1039/d4ra08493d

rsc.li/rsc-advances

1. Introduction

The discharge of effluent containing organic pollutants and toxins into the environment has significant risks for the biosphere and is a serious health threat to humans.[1] Among these pollutants are antibiotics, commonly used to treat bacterial infections.[2]

Among the antibiotics, ofloxacin is a frequently used fluoroquinolone-based drug found in surface water at up to 31.7 μg L^{-1} concentrations. Even at very low concentrations, ofloxacin can have a detrimental effect on ecological systems by preventing the growth of microorganisms and producing other ecotoxicological effects.[3–7] Hence, it is crucial to remove these pollutants from wastewater.[8,9] Many methods have been developed so far, including nano-filtration, coagulation, ion exchange, photocatalysis, adsorption, *etc.* One of the most appealing methods for treating wastewater is photocatalysis as it causes the contaminants to entirely break down rather than merely shifting from one medium to another.[10] In recent years, semiconductor catalysed photocatalytic degradation of organic contaminants has grown significantly by consuming solar light energy due to increasing environmental concerns.[11–14]

Bi_2MoO_6, an Aurivillius oxide, exhibits interesting physicochemical properties, such as a band gap of nearly 2.7 eV. This unique semiconductor reveals excellent performance under visible light irradiation. Its structure includes $[MoO_4]^{-2}$ alternate sheets with $[Bi_2O_2]^{+2}$ layers, distinguishing it from other bismuth-based materials.[15] However, because of the low separation efficiency of the photoexcited charge carriers, Bi_2MoO_6 is insufficiently efficient to meet the requirements of the application.[16] This drawback can be avoided by using various approaches like porosity engineering, elemental doping, semiconductor modification by creating heterojunction structures, *etc.*[17] Because of its high stability and low cost, g-C_3N_4 is a promising material for making semiconductor heterojunctions. Other advantages include strong physicochemical stability, a 2.7 eV band gap, non-toxicity, and a large surface area.[10]

Furthermore, photocatalytic activity is increased by loading various plasmonic metals due to their localised surface plasmon resonance (LSPR) properties, which help to separate charge carriers and excite electron–hole pairs.[18] Bismuth (Bi), a non-noble metal, exhibits a significant LSPR effect along with

[a]*Department of Chemistry and Biochemistry, Thapar Institute of Engineering & Technology, Patiala 147004, Punjab, India. E-mail: bpal@thapar.edu; rkdas@thapar.edu*

[b]*TIET-Virginia Tech Center of Excellence in Emerging Materials, Thapar Institute of Engineering & Technology, Patiala 147004, Punjab, India*

† Electronic supplementary information (ESI) available. See DOI: https://doi.org/10.1039/d4ra08493d